EXPERIMENTAL AND NUMERICAL INVESTIGATION OF THE THERMAL PERFORMANCE OF GAS-COOLED DIVERTOR MODULES

A Thesis
Presented to
The Academic Faculty

by

Lorenzo Crosatti

In Partial Fulfillment
of the Requirements for the Degree
Doctor of Philosophy in the
School of Mechanical Engineering

Georgia Institute of Technology
August 2008

EXPERIMENTAL AND NUMERICAL INVESTIGATION OF THE THERMAL PERFORMANCE OF GAS-COOLED DIVERTOR MODULES

Approved by:

Dr. Said I. Abdel-Khalik, Co-Advisor
School of Mechanical Engineering
Georgia Institute of Technology

Dr. Minami Yoda, Co-Advisor
School of Mechanical Engineering
Georgia Institute of Technology

Dr. Yogendra Joshi
School of Mechanical Engineering
Georgia Institute of Technology

Dr. S. Mostafa Ghiaasiaan
School of Mechanical Engineering
Georgia Institute of Technology

Dr. Narayanan M. Komerath
School of Aerospace Engineering
Georgia Institute of Technology

Dr. Donald R. Webster
School of Civil Engineering
Georgia Institute of Technology

Date Approved: June 12, 2008

To my beloved Julia.

To my parents Annalisa and Giovanni

and my brother Gianluca:

so far away, but always so close to my heart.

ACKNOWLEDGEMENTS

The successful completion of this thesis would not have been possible without the support and the guidance of many individuals. Foremost, I would like to thank my co-advisors, Dr. Minami Yoda and Dr. Said I. Abdel-Khalik. Their invaluable, continuous and inexhaustible advice and support throughout these past three years were greatly appreciated. I would also like to thank the additional members of my thesis committee, Dr. Yogendra Joshi, Dr. S. Mostafa Ghiaasiaan, Dr. Narayanan M. Komerath, and Dr. Donald R. Webster for their suggestions and prompt support.

I wish to particularly thank Mr. Dennis L. Sadowski for his important collaboration in this project and his enthusiasm in the labs. Many thanks go to my friends and laboratory colleagues for their moral and practical support: Martin Kistenmacher, J. B. Weathers, Tim Koehler, Elizabeth Gayton (Libby), Celine Lascar, Joseph Hu (C.C.), Bo Lu, Haifeng Li, Charlotte Kotas, Myeongsub Kim, Keith Suda-Cederquist, Domenico Lippolis and Dr. Vladimir Novak.

I also wish to thank the ME Office of Student Services staff, in particular Glenda Johnson. My time at Georgia Tech wouldn't have been as enjoyable without the Mechanical Engineering Graduate Students Association (*MEGA*), and my friends Brent Nelson, Gregory Ostrowicki (Greg), Logan McLoed, David Damm and many others.

The individual whom I need to thank the most is my fiancée Julia Chivington-Buck. It is only with her love, support, patience and comprehension that I could achieve this important goal in my life.

TABLE OF CONTENTS

LIST OF TABLES

LIST OF FIGURES

NOMENCLATURE

Variables and Constants

A_{cooled}	Area of the cooled surface	[m^2], [mm^2]
A_h	Total area of the holes — T-Tube	[m^2], [mm^2]
A_{jets}	Total area of the jets — HEMJ	[m^2], [mm^2]
A_{neck}	Concentrator "neck" area	[m^2]
A_{slot}	Area of the slot — T-tube	[m^2], [mm^2]
B	Slot width	[mm]
c	Specific heat (solids)	[J/(kg·K)]
c_h	Specific heat at constant temperature	[J/(kg·K)]
c_p	Specific heat at constant pressure	[J/(kg·K)]
D	Holes diameter	[m], [mm]
D_{jet}	Center jet diameter — HEMJ	[m], [mm]
D_h	Hydraulic diameter of the slot	[m], [mm]
H	Jet-to-wall spacing	[mm]
h	Local surface heat transfer coefficient	[W/(m^2·K)]
h_{amb}	Heat transfer coefficient between test module and ambient	[W/(m^2·K)]
h_{exp}	Experimental local surface heat transfer coefficient	[W/(m^2·K)]
h_{max}	Maximum surface heat transfer coefficient	[W/(m^2·K)]

k	Thermal conductivity	[W/(m·K)]
L	Slot length	[m], [mm]
l	Characteristic length	[m], [mm]
$\dot{m}$	Mass flow rate	[kg/s], [g/s]
$\dot{m}_\ell$	Mass flow rate per unit slit length	[g/(s·m)]
M	Mach number	[-]
Nu	Nusselt number	[-]
P_{in}	Coolant inlet pressure	[Pa]
P_{oper}	Ambient or operating pressure	[Pa]
P_{out}	Coolant exit pressure (gauge)	[Pa]
Pr	Prandtl number	[-]
$\dot{Q}$	Total power input	[W]
$\dot{Q}_v'''$	Uniform heat generation rate per unit volume	[W/m^3]
$\dot{q}''_{avg}$	Average heat flux	[W/m^2]
$\dot{q}''_{CFD}$	Numerically predicted local heat flux	[W/m^2]
$\dot{q}''_{net}$	Measured incident heat flux	[W/m^2]
$\dot{q}''_{nom}$	Nominal incident heat flux	[W/m^2]
Re	Reynolds number	[-]
T_{in}	Coolant inlet temperature	[°C]
T_{out}	Coolant outlet temperature	[°C]

T_{top}	Temperature of the copper free surface at the top of the test module — HEMJ	[°C]

Abbreviations and Acronyms

BCs	Boundary Conditions
CAD	Computer Aided Design
CFD	Computational Fluid Dynamics
He	Helium
HTC	Heat Transfer Coefficient
MFE	Magnetic Fusion Energy
PFC(s)	Plasma Facing Component(s)
TC(s)	Thermocouple(s)

Greek Letters

μ	Dynamic viscosity	[kg/m·s]
ν	Kinematic viscosity	[m^2/s]
ρ	Density	[kg/m^3]
θ	Angular position	[°]

Subscripts

amb	Property value in ambient conditions
avg	Average value
cond	Conduction

emb	Embedded
exp	Experimental value
CFD	*FLUENT*® prediction value
in	Property value at inlet
ℓ	Quantity per unit slit length
net	Measured (experimental) value
nom	Calculated value
oper	Operating
out	Property value at outlet
$surf$	Surface
v	Quantity per unit volume

SUMMARY

In a fusion reactor, burning plasma[1] has to be sustained for a long period of time. In-vessel components which are directly facing the plasma are called *plasma facing components (PFCs)*. These elements receive the thermal power of the plasma either through radiation (*first containment wall, blanket*) or by heat transport via particles from the center of the plasma towards "specialized" components around the plasma (*divertor*).

During the operation of a fusion reactor, fusion reaction ash (α-particles) and eroded particles from the reactor become present in the plasma. These contaminants reduce the purity of the plasma and hinder further fusion reactions. In magnetic confinement reactors, *divertors are used to remove these unwanted products from the plasma*. Since the divertor is placed across the magnetic field line used to confine the plasma, not only its solid surface (*target plate*) is directly exposed to the plasma, but it is also subject to a flux of highly energetic particles from the plasma. The incident surface heat load distribution on the divertor depends on its surface topology, location, reactor type, and plasma conditions; peak surface heat fluxes on the order of 10 MW/m^2 are anticipated (based on the current plasma physics calculations) with surface temperatures in the region of 1,200 °C to 1,500 °C. The role of the divertor is not only to remove impurities but also to remove heat load from the plasma. *A significant fraction* (~ 15 %) *of the total fusion thermal power is removed by the*

[1] A plasma, the fourth state of matter, is typically a high temperature and high density ionized gas. The free electrons in the plasma make it electrically conductive and hence a plasma can be confined and compressed by an electromagnetic field.

divertor coolant and therefore it cannot be wasted. In addition to its desirably high thermal conductivity, helium is proposed as the leading coolant because of its high temperature power conversion (*Brayton*) cycle and material compatibility.

Several He-cooled divertor designs have been considered, including a modular T-tube design (Ihli et al., 2005), a large tungsten plate design (Hermsmeyer and Malang, 2002) and a modular "finger" configuration with jet impingement cooling from perforated end caps which requires a very large number of modules (Ihli et al., 2006; Norajitra et al., 2003a). Analyses have been performed to characterize the T-tube divertor geometry, location, and heat load distribution (Mau et al., 2006). Detailed analyses have been performed using the *FLUENT*® CFD software package to evaluate the thermal performance at the nominal design and operating conditions. Extremely high heat transfer coefficients (~50,000 W/(m^2·K)) have been predicted (Shin et al., 2005). Since these values of heat transfer coefficient are considered to be "outside of the experience base" for gas-cooled systems, an experimental investigation has been undertaken to validate the results of the numerical simulations. This thesis focuses on the thermal performance of the T-tube and the "finger" divertor designs. Numerical and experimental investigations have been performed to support both divertor geometries. Emphasis will be placed on the experimental work performed to validate the results of the numerical analyses.

This research work will contribute to the understanding and prediction of the performance of the leading proposed helium-cooled divertor designs for near- and long-term MFE reactor designs. The results will provide confidence in the ability of state-of-the-art CFD codes to model high heat flux plasma-facing components (PFCs) including divertors.

CHAPTER I

INTRODUCTION

The first part of this chapter is intended to provide a basic background on Magnetic Fusion Energy (MFE); related material and additional information can be found in Stacey (1984); Key (2001) and online (ITER, 2008; ThinkQuest, 2008; Wikipedia, 2008). The motivation and objective of this doctoral thesis will follow.

1.1 Fusion Power

Fusion is the energy source of the Sun and the stars (Figure 1.1). Fusion power refers to power generated by nuclear fusion reactions. In this kind of reaction, two light atomic nuclei fuse together to form a heavier nucleus and in doing so, release energy (Section 1.1.2). Here on Earth, future fusion plants will imitate the Sun, fusing *hydrogen isotopes* (*deuterium* (^2H) and *tritium* (^3H)) at temperatures over 10^8 K, releasing energy for a variety of uses, including electricity.

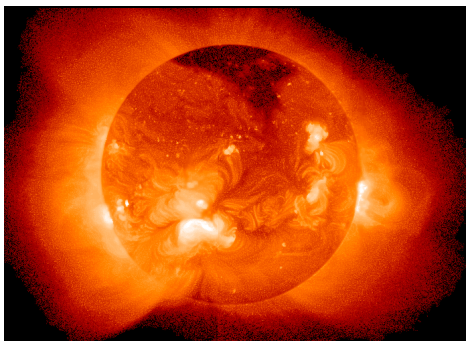

Figure 1.1: The Sun is a natural fusion reactor.

The atoms to be fused must be in the form of a *plasma*. The fourth state of matter is obtained by heating a gas, increasing the kinetic energy of the atoms. At a high enough temperature, the electrons separate from the nuclei, creating a cloud

of charged particles (ions). This cloud consists of an equal amount of positively charged nuclei and negatively charged electrons and is called plasma. The Sun, stars, lightning, and the gas in neon signs are all plasmas. Even higher temperatures are needed to cause the nuclei to collide and fuse (ThinkQuest, 2008).

Fusion requires precisely controlled conditions of *temperature*, *pressure* and *magnetic field parameters* (for MFE) in order to generate net energy, with several technological challenges impeding its practical implementation:

Temperature. At higher temperatures, the nuclei will have a higher kinetic energy. The nuclei need enough energy to overcome their electromagnetic repulsion and fuse. At higher plasma temperatures, more fusion occurs.

Pressure. Higher pressures (i.e., denser plasma) imply higher probability of collision among the nuclei. The pressure, however, will be limited to avoid plasma instabilities.

Containment. The plasma must be confined long enough in order for fusion to occur. The Sun uses its huge gravitational force to contain and compress the particles together (continuous inertial confinement). However, here on Earth, the gravitational field is not strong enough. Instead, the confinement process is achieved through one of two methods: magnetic confinement (Section 1.1.3) or inertial confinement.

This thesis will focus on one of the plasma-facing components (PFCs), the divertor (Section 1.1.5). The understanding and prediction of the performance of the leading proposed helium-cooled divertor designs will contribute to the solution of plasma containment related issues for the robust design of near- and long-term MFE reactors.

1.1.1 Why Fusion?

The world's energy demand (especially electricity) is increasing because of its growing population and the amount of energy use per capita. Nowadays, the energy production is heavily based on fossil fuels, which supply 80 % of the world's energy. The rising of well known problems related to our present energy system (such as ecological issues and limitation of fossil fuels supply) could be addressed by a sustainable energy mix (ITER, 2008). Fusion energy could provide the energy to meet these requirements, having potential benefits including (ITER, 2008):

- First of all, fusion is an *almost limitless fuel supply*. The basic fuels are distributed widely around the globe. Deuterium is abundant because it can be extracted from sea water. Lithium, from which tritium can be produced, is an available light metal in the Earth's crust.

- Fusion produces *no greenhouse gas emissions*. Fusion power plants will not generate gases such as carbon dioxide that cause global warming and climate change, nor other gases that have damaging effects on the environment.

- Fusion is suitable for the *large-scale electricity production* required for the increasing energy needs. A single fusion power station could generate electricity for two million households.

- The fusion reaction is *inherently safe*. Only about two grams of fuel is present in the plasma vessel, enough for a few seconds of "burn". As fusion is not a chain reaction, the reaction can never run out of control.

1.1.2 Fuel Cycle

In any fusion reaction, two or more atoms are "pushed" very close together, so that the their nuclei will pull together into one larger atom. When two light nuclei fuse, they will generally form a single nucleus with a slightly smaller mass than the sum

of their original masses. The difference in mass is released as energy according to Einstein's mass-energy equivalence formula $E = mc^2$ (Stacey, 1984).

The net positive charge of the nuclei acts against the fusion between the atoms. It is necessary to provide an external source of energy in order to overcome this electrostatic force, or "Coulomb barrier". The simplest way to achieve this is to heat the atoms, causing the electrons to be stripped from the atoms which are left as bare nuclei. In most experiments the nuclei and electrons are coexisting in a plasma. Since the temperatures required to provide the nuclei with enough energy to overcome their repulsion is a function of the total charge, hydrogen reacts at the lowest temperature because it has the smallest nuclear charge. Helium has an extremely low mass per nucleus and therefore is energetically favored as a fusion product. As a consequence, most fusion reactions combine isotopes of hydrogen ("protium", deuterium, or tritium) to form isotopes of helium (^{3}He or ^{4}He) (Stacey, 1984).

The easiest (according to the Lawson criterion[1]) and most immediately promising nuclear reaction to be used for fusion power is: $D + T \rightarrow {}^4He + n$ (Figure 1.2).

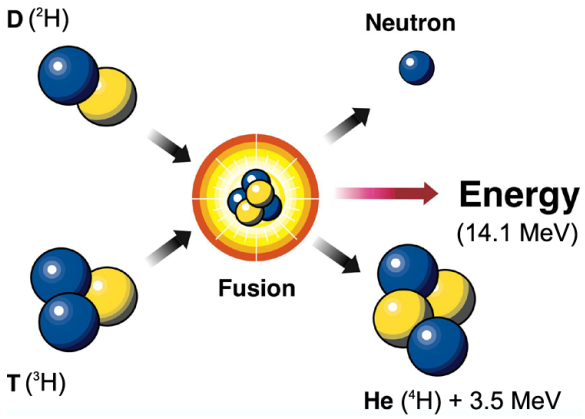

Figure 1.2: Diagram of the D-T reaction (`http://iter.rma.ac.be`).

[1]The Lawson criterion, first derived by John D. Lawson in 1955 and published in 1957, defines the conditions needed for a fusion reactor to reach ignition, that is, that the heating of the plasma by the products of the fusion reactions is sufficient to maintain the temperature of the plasma against all losses without external power input.

As mentioned earlier, deuterium is a naturally present in water and therefore is universally available. Tritium occurs naturally only in negligible amounts due to short radioactive life. Consequently, the deuterium-tritium fuel cycle requires the breeding of tritium from lithium using one of the following reactions:

$n + {}^{6}Li \rightarrow T + {}^{4}He$

$n + {}^{7}Li \rightarrow T + {}^{4}He + n$

1.1.3 Magnetic Confinement Fusion

Magnetic confinement fusion is an attempt to contain the electrically conductive plasma with magnetic fields, providing the conditions needed for fusion energy production. In a basic concept, there is a balance between magnetic pressure and plasma pressure. Magnetic confinement is one of two major branches of fusion energy research, the other being inertial confinement fusion. The magnetic approach is more highly developed and is usually considered more promising for energy production. A 500-MW heat generating fusion plant using magnetic confinement is currently being built in France (ITER) (Ongena and Van Oost, 1999).

The pressure achievable in MFE is low ($\sim$ 1 bar) and with a confinement time of only a few seconds. In Inertial Fusion Energy (IFE), inertial confinement has in contrast much higher pressures but much lower confinement times. Generally, magnetic confinement schemes also have the advantage of being steady state, as opposed to the intrinsically pulsed operation of inertial confinement (Ongena and Van Oost, 1999).

The simplest magnetic configuration is a solenoid, a long cylinder wound with magnetic coils producing a field with the lines of force running parallel to the axis of the cylinder. However, such configuration would stop ions and electrons from being lost radially, but not from being lost from the ends of the solenoid (Ongena and Van Oost, 1999).

Two approaches are commonly proposed to solving this problem. One consists in stopping the particles from being lost at the ends of the solenoid with magnetic mirrors. The other consists in eliminating the ends altogether by bending the solenoid around to close on itself. This last solution is known as *toroidal field*.

1.1.4 Toroidal Machines

One of the proposed toroidal machines for MFE is the *tokamak*. In tokamaks, plasma is confined in a toroidal vessel by a magnetic field with two main components: the first (toroidal) field is produced by coils placed around the reactor vessel. The second (poloidal) field is added to counteract the natural pressure inside the plasma which tends to make it expand and it is generated by the large plasma current which is also used to heat the plasma. Tokamaks generally work in pulse mode (EC Energy Research, 2008).

The largest current tokamak experiment is the Joint European Torus (JET)[2] (Figure 1.3), which is the largest nuclear fusion experimental reactor yet built. The construction started in 1978. In 1997, JET produced a peak of 16.1 MW of fusion power with a gain[3] of 0.65, and fusion power of over 10 MW sustained for over 0.5 s. During 2004, JET was shut down for a series of upgrades increasing the total available heating power to over 40 MW, preparing the ground for further studies relevant to the development of ITER[4] (Figure 1.4) to be undertaken (Nuclear Fusion Power, 2007).

In June 2005, the construction of the experimental reactor ITER was announced. "*ITER will produce 500 million watts of fusion power for a period of at least 400 seconds.*"[5] The heat produced by ITER will be many times greater than the external power provided to initiate the fusion. A gain of over 10 will be achieved. After ITER,

[2] `http://www.jet.efda.org`

[3] gain is the ratio of the plasma output power and the input power provided to the plasma

[4] International Thermonuclear Experimental Reactor.

[5] `http://www.pppl.gov/projects/pics/ITER4pg.pdf`

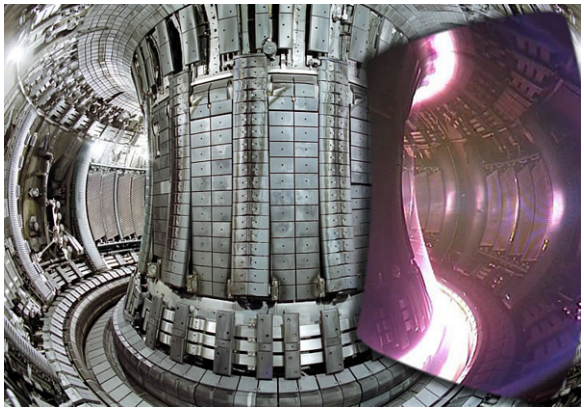

Figure 1.3: Internal view of the JET tokamak superimposed with an image of a plasma taken with a visible spectrum video camera. ©EFDA-JET (`http://fusionforenergy.europa.eu/4_3_picture_gallery_en.htm`)

an experimental reactor will be constructed to provide the first real fusion power plant example (and an important step forward from the previous physics experiments). The Demonstration Power Plant (DEMO) will produce $2,500 \times 10^6$ W of fusion thermal power of which 40 % (corresponding to $1,000 \times 10^6$ W) will be continuously converted in electricity with a gain of over 25.

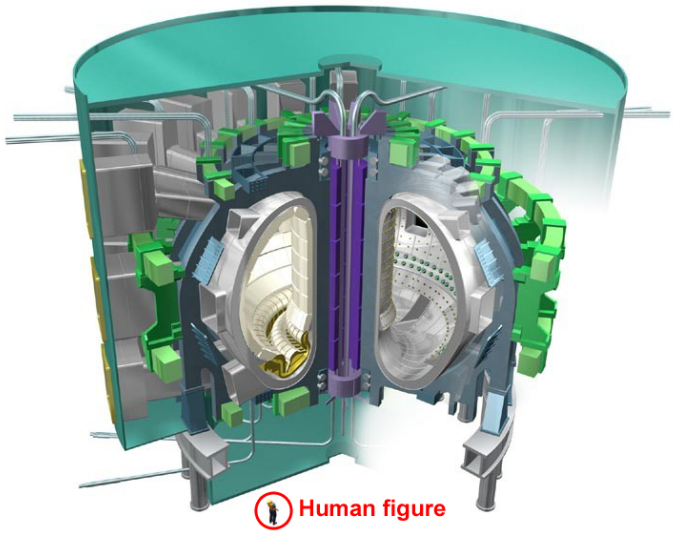

Figure 1.4: ITER is a very large tokamak (`http://www.jet.efda.org/pages/jet-iter/about/index.html`).

Another topology of toroidal machine for MFE is the *stellarator*. The stellarator concept was proposed in 1951 by Lyman Spitzer of Princeton University. Its name

means "star machine", because stars produce energy from fusion. This star machine is similar to a tokamak since it uses strong magnetic fields to confine the plasma in a torus-shaped vessel. The difference is that in stellarators the plasma is confined entirely by magnetic fields produced by external coils. This eliminates the need of a toroidal plasma current but it results in a more complex shape for the coils than in tokamaks. Stellarators are designed to operate at steady state. Instabilities and other plasma events associated with the energy of a large (several million A) toroidal current do not occur or are strongly reduced (EC Energy Research, 2008). Najmabadi (2006) reports that a study of compact stellarator power plants, ARIES-CS (Figure 1.5), was initiated recently to explore attractive compact stellarator configurations and to define key R&D areas.

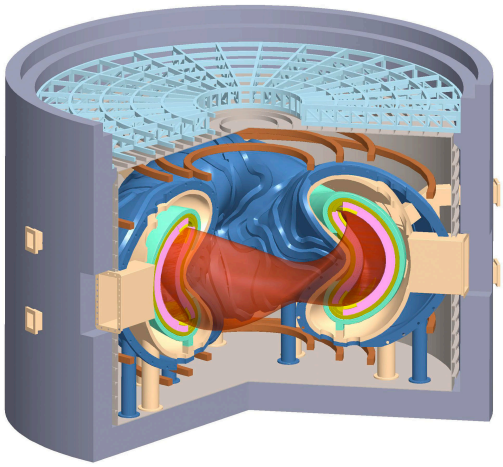

Figure 1.5: The ARIES Compact Stellarator Power Core has a radius R=7.75 m (`http://www-ferp.ucsd.edu/LIB/CAD/FIGURE/ARIES-CS/`).

1.1.5 The Divertor

During the operation of a fusion reactor, fusion reaction ash (α-particles) and eroded particles from the reactor become present in the plasma. These products and unburned fuel reduce the quality of the plasma and hinder further fusion reactions. In magnetic confinement reactors, *divertors are crucial components* since:

1. They remove these unwanted products from the plasma

2. A significant fraction ($\sim$ 15 %) of the total fusion thermal power is removed by the divertor coolant

Electromagnetic fields are used to remove these particles from the plasma and focus them onto a target called the divertor (Figures 1.6). The incident surface heat load distribution on the divertor depends on the surface topology, location, reactor type, and plasma conditions; peak surface heat fluxes on the order of 10 MW/m^2 are expected with a surface temperature in the region of 1,200 °C to 1,500 °C. Helium has been proposed as the divertor coolant vs. water primarily because of its material compatibility due to its chemical inertness and because of its ability to operate at high temperatures, which enhances the thermal efficiency of the power conversion systems (Crosatti et al., 2007).

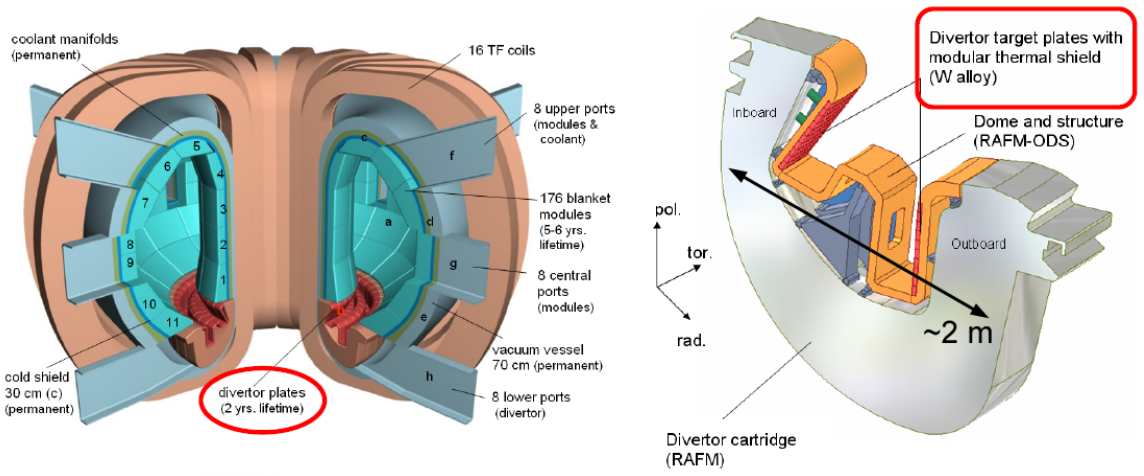

Figure 1.6: Reactor model (left) and divertor cassette (right).(Norajitra et al., 2003b) The PFC components subject of this research study are design to protect the divertor target plates (red [dark] surface).

The directly cooled heat transfer parts of the gas cooled divertor target are made from tungsten (W) alloy. The low temperature ductility and the ductile to brittle transition temperature (DBTT) of a tungsten alloy can be dramatically improved by alloying other elements. For an improved tungsten alloy a DBTT of 600 °C and a

recrystallization temperature of 1,300 °C were judged to be a reasonable estimation, which was used as design limits for the current design approach (Ihli et al., 2005).

Divertors are relatively large devices. Although they remove "only" ~ 15 % of the total reactor thermal power, they need to cover a large surface area (up to ~ 50 m^2). The only existing example of an actual divertor design is the *ITER* divertor (Figure 1.7) which is a water-cooled type (Norajitra et al., 2007). The ITER divertor uses water rather than He because of its experimental nature. This experimental reactor is not designed to address the issues related to the collection and conversion of the heat load incident upon the divertor. This water-cooled divertor is less efficient and it operates at lower temperatures than an He-cooled one. Its solid surface is made of copper rather than a tungsten alloy.

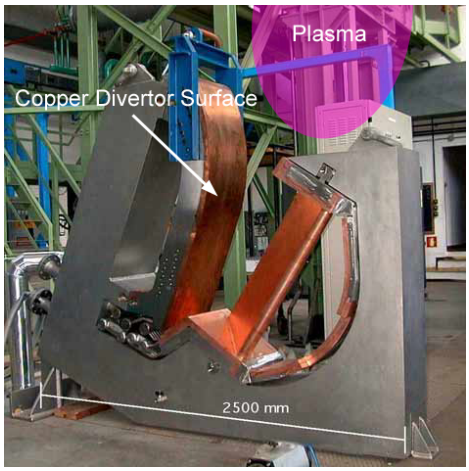

Figure 1.7: ITER — Full scale divertor integration prototype. Courtesy of EFDA. (`http://fusionforenergy.europa.eu/4_3_picture_gallery_en.htm`)

1.2 Motivation

Recently, several helium-cooled divertor concepts have been proposed: their main advantages derive from their compatibility with a variety of blanket concepts and ability to operate at high temperatures, which enhances the thermal efficiency of the power conversion systems. Several designs have been considered, including a modular T-tube design (Ihli et al., 2005), a large tungsten plate design (Hermsmeyer and

Malang, 2002) and a modular "finger" configuration with jet impingement cooling from perforated end caps which requires a very large number of modules (Ihli et al., 2006; Norajitra et al., 2003a). These proposed configurations are all designed to accommodate a peak heat load of 10 MW/m^2. The T-tube modular design based on jet impingement cooling was selected by the *ARIES−CS* conceptual design study because it could accommodate the expected high heat fluxes, while using intermediate-size modules, thereby reducing the complexities associated with manufacturing and assembly of the much smaller modules of the finger design (Raffray et al., 2006). The helium-cooled multi-jet (*HEMJ*) modular "finger" configuration with jet impingement cooling from perforated end caps has been proposed as the lead divertor design for the post-*ITER* demonstration reactor (*DEMO*). Its compact size is necessitated by the need to minimize the thermal stresses in the divertor module.

Analyses have been performed to characterize the divertor geometry, location, and heat load distribution (Mau et al., 2006). Detailed analyses have been performed using the *FLUENT*® CFD software package to evaluate the thermal performance at the nominal design and operating conditions. Extremely high heat transfer coefficients (~50,000 W/(m^2·K)) have been predicted (Shin et al., 2005). Because these values of heat transfer coefficient are considered to be "outside of the experience base" for gas-cooled systems, *an experimental investigation was undertaken to validate the results of the numerical simulations.*

Because of the natural inertness and high-temperature power conversion cycle compatibility, He is proposed as the ideal coolant for these PFCs. The drawback is its comparatively low heat exchange capability. This, however, can be enhanced in various ways, e.g., by promoting turbulence and/or by increasing the solid/fluid interface area (Norajitra et al., 2007). This increases the complexity of the divertor geometry, with reverse flows, stagnation regions, and high-shear regions–all of which make numerical simulations more difficult. The results of this investigation will be

used to validate state-of-the-art CFD codes used to model complex flow geometries of divertors and other applications that require such heat removal enhancement (e.g., cooling of turbine blades, electronic components, etc.).

This experimental investigation on the T-tube and the HEMJ "finger" will provide additional data on jet impingement cooling. The results will be used for many other high heat flux engineering applications.

The experimental results obtained with these test modules will establish a design database that will be useful for designers of MFE power plants. Specifically, these data will be used to validate numerical models for predicting the thermal-hydraulic behavior of helium-cooled divertors. These numerical models, implemented in commercially available software, will in turn be used to evaluate and improve the performance of gas-cooled high heat-flux plasma-facing components, thereby improving the long-term performance of MFE reactor designs.

Developing divertors that can withstand the extreme heat fluxes and temperature gradients typical of tokamak plasmas is required to maintain the purity of the plasma for long-term operation of MFE devices. This research will therefore contribute to new, robust and reliable MFE power plant designs.

1.3 Objective

The primary objective of this doctoral thesis is to experimentally validate the thermal performance of leading design configurations of helium-cooled divertor modules for magnetic fusion energy (MFE) applications. This research focuses on the thermal performance of the T-tube divertor design selected by the *ARIES* team (Section 2.2.1) and the "finger" design proposed by the European Union for the post-ITER demonstration reactor (Section 2.2.2). Numerical and experimental investigations have been performed to support both design configurations. Specifically, extremely high heat transfer coefficients predicted by CFD calculations for the jet impingement adopted

in both the $T-tube$ and *HEMJ* divertor designs were experimentally validated. The investigation was performed by comparing the numerical predictions of CFD software package (*FLUENT*®) to experimental data obtained in air flow loop tests.

A test module which closely simulates the planar jet impingement concept used in the proposed He-cooled T-tube divertor has been designed, constructed, instrumented and tested using air as the coolant while maintaining the same dimensionless parameters range as the He-cooled T-tube divertor design (Chapter 3). Axial and azimuthal variations of the local heat transfer coefficient have been measured over a wide range of operating conditions.

The test module used in those experiments, however, did not duplicate the exact geometry of the T-tube divertor, particularly the single-sided nature of the incident heat flux. Therefore, the thermal performance of a prototypical T-tube divertor module has been experimentally and numerically examined. The test module has been designed and constructed to match the geometry, dimensions, material properties, and single-sided heating configuration of the actual T-tube divertor. Experiments have been conducted using air as the coolant with different values of the incident heat flux (Chapter 4). As in the previous case, the coolant flow conditions have been selected to span the expected range of dimensionless parameters for the actual helium-cooled T-tube divertor design.

A test section that duplicates the HEMJ "finger" divertor design has also been designed, constructed, instrumented and tested (Chapter 5). Similar to the T-tube experiment, air has been used as the coolant while maintaining the same dimensionless parameters of the proposed He-cooled divertor design (Section 2.2.2.1). Once again, the experimental results were compared with the code prediction over a wide range of operating conditions.

Conclusions and recommendations derived from the results of this investigation are presented in Chapter 6.

CHAPTER II

LITERATURE REVIEW

This chapter presents an overview of the jet impingement cooling techniques and its general applications in industry. Additionally, the leading divertor designs studied in this thesis are described; other divertor designs are also presented.

2.1 Jet Impingement Cooling Technique

2.1.1 Industrial Applications of Jet Impingement Cooling Technique

In this section, earlier studies on jet impingement cooling are presented. Jet impingement can achieve a high heat/mass transfer rate on the surface of an object. It has therefore been adopted in the leading divertor designs, including those examined in this investigation. In the steel or glass industry, impinging jets are applied to temper products after rolling. In the aviation industry, impinging jets are used for cooling turbine blades in gas turbine engines. In the electronics industry, impinging jets are applied to cool electronic components in order to meet the demand of compactness and high power consumption. In addition to the above cooling applications, in the paper industry, impinging jets are adopted to enhance drying processes (Incropera and DeWitt, 2002).

2.1.2 Single Jet Impingement

A large amount of work relating to axisymmetric single-jet impingement heat transfer has been reported in the literature (see, for example, Garimella and Rice (1995); Fitzgerald and Garimella (1998); San et al. (1997)). Gardon and Akfirat (1966) studied impinging two-dimensional air jets. According to Martin (1977), the flow field of an impinging jet can be divided into three separate regions: the free jet region

(near the nozzle exit), the impingement region where the jet approaches the surface, and the wall jet region that runs parallel to the surface where the jet "bifurcates" (Salamah and Kaminski (2005), Figure 2.1). In the case of *submerged* jets, i.e., jets surrounded by the same fluid as the jet (like those studied in this investigation), the entrainment of the surrounding fluid cannot be neglected. The entrainment of still surrounding fluid causes mixing in the free-jet region. Salamah and Kaminski (2005) report that for the low Reynolds numbers this mixing affects the mid-plane velocities, resulting in a lower heat transfer coefficient (HTC) with increasing nozzle height h. Salamah and Kaminski (2005) also report that at Re above 2,750, the HTC increases with increasing elevation of the jet. This is due to the effect of turbulence; the decrease in jet velocity is compensated by an increased jet turbulence (Salamah and Kaminski, 2005), which increases continuously with the distance h (Lin et al., 1996). The turbulence intensity along the centerline of the jet is generated by mixing and is much higher than that of pipe flow and can reach levels in the order of 30 % (Lin et al., 1996).

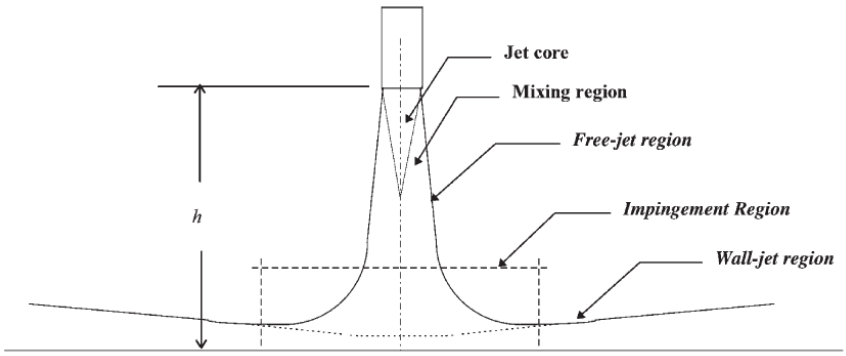

Figure 2.1: Schematic of a single jet impinging on a surface (Salamah and Kaminski (2005), Figure 1).

The flow in the free jet region is axial in direction and is not affected by the presence of the impingement surface. In the impingement region, however, the flow is affected by significant changes in the velocity direction which turns from perpendicular to nearly parallel to the impingement surface (Salamah and Kaminski, 2005).

Based on velocity field measurement, Gardon and Akfirat (1966) found that the jet starts being influenced by the impingement surface approximately 1.2 nozzle diameters from the surface. In this impingement region, the flow is decelerated in the axial direction and accelerated in the radial direction. Very close to the wall, a stagnation region exists, and classical stagnation flow solution can be applied (Salamah and Kaminski, 2005). Throughout the impingement region the boundary layer (BL) has a constant thickness (Gardon and Akfirat, 1966), but it begins to thicken in the absence of the positive pressure gradient in the stagnation region. This is based on BL analyses predicting an "*exact balance between the thinning of the boundary layer due to stream acceleration and the thickening due to shear diffusion*" (Salamah and Kaminski, 2005).

The local heat transfer coefficient on the impingement surface has been found to have a bell-shaped distribution with respect to radial distance from the stagnation point. The maximum local value occurs near the stagnation point and decreases symmetrically with radial distance. However, several investigators have reported secondary maxima in the local heat transfer coefficient curves (with air jets and submerged liquid jets) (Garimella and Rice, 1995). All of these studies indicate that this secondary peak occurs near a nondimensional radial coordinate of $r/d \approx 2$ (where r is the radial coordinate from the center of the jet and d is the diameter of the jet). "*According to Martin (1977), the boundary layer typically becomes turbulent at the beginning of the wall jet region, giving rise to a secondary peak in the heat transfer coefficient*" (Garimella and Rice, 1995). Garimella also reports that the transition to turbulence was established as a likely cause for the secondary peak by the hot-wire anemometry measurements of den Ouden and Hoogendoorn performed in 1974. Typical values of the stagnation Nusselt number Nu_{sg} for submerged air jets are shown in Figure 2.2. The stagnation Nusselt number increases linearly with the Reynolds number of the jet.

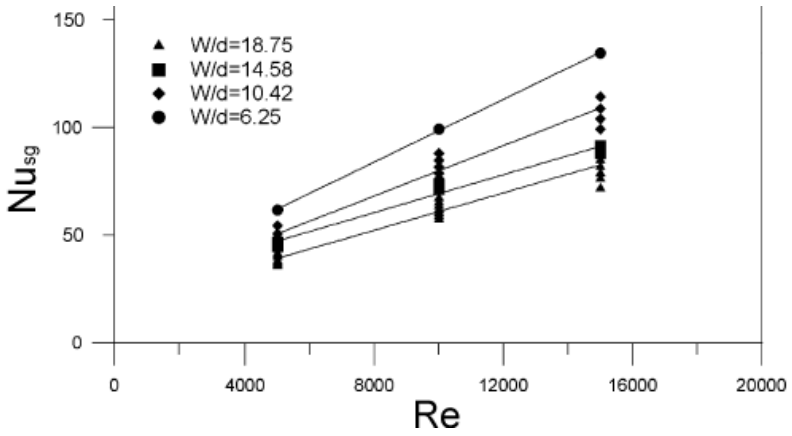

Figure 2.2: Measured Nu at the jet stagnation point for different Re and plate width W (San et al. (2007), Figure 5).

The majority of the studies on impinging gaseous jets involved a single round jet or a rows of such jets. Due to the three-dimensional nature of the flow structure and complicated heat transfer distribution, there are very limited previous studies on impinging rectangular jet heat transfer (Zhou and Lee, 2007). Figure 2.3 depicts the variation of the lateral heat transfer rate with respect to the jet Reynolds number in the range of $Re \approx 2.7 \times 10^3$ to $\approx 2.5 \times 10^4$ at fixed nozzle-to-plate spacing $Z/B = 4$ (here Z is the nozzle-to-plate distance and B is the nozzle width). Except for the case of $Re = 2715$, the general shape of the local Nusselt number distribution is similar, although the magnitude increases with jet Reynolds number. The local Nu is maximum near the stagnation line and exhibits a peak at around $X/B = 0.35$ (where X is the lateral coordinate measured from the jet centerline). The local heat transfer rate decreases rapidly with increasing values of X (Zhou and Lee, 2007). The lateral distribution of the local Nusselt number has a second peak locating at $X/B = 2.36$-2.89 except for the case of $Re = 2,715$. Beyond the peak the local Nusselt number decreases monotonically. The second peak occurs only for higher jet Reynolds number and lower nozzle-to-plate spacing, behaving as circular air jets (Zhou and Lee, 2007).

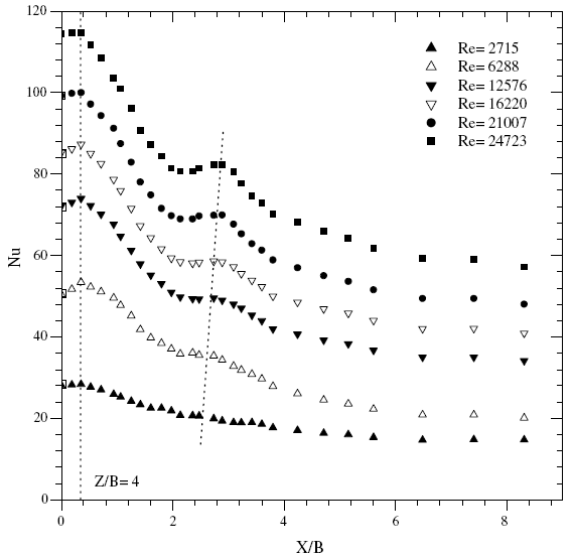

Figure 2.3: Lateral variation of the local Nusselt number at a given nozzle-to-plate spacing $Z/B = 4$ (Zhou and Lee (2007), Figure 8).

2.1.3 Effect of Jet-to-Wall Spacing in Jet Impingement

San and Shiao (2006) investigated the effects of plate size and plate spacing on the stagnation Nusselt number for a round air jet impinging on a flat surface. Figure 2.4 indicates that the stagnation Nusselt number decreases with an increase of the plate spacing-to-jet diameter ratio H/d (here H is the jet-to-place distance and d is the jet diameter). A larger spacing between the jet plate and impingement plate allows a longer distance for the jet to mix with the recirculation flow before the jet reaches the impingement plate. As mentioned earlier, this flow mixing deteriorates the heat transfer. Thus the result shows that the stagnation Nusselt number decreases with an increase of H/d.

Zhou and Lee (2007) investigated the effects of nozzle-to-plate spacing for rectangular (slot) jets. Figure 2.5 illustrates the lateral variation of the local Nusselt number with the nozzle-to-plate spacing at $Re = 12,500$. Independent of the nozzle-to-plate spacing, the local Nu increases initially with the lateral distance from the stagnation line and then decreases beyond the first peak at about $X/B = 0.35$.

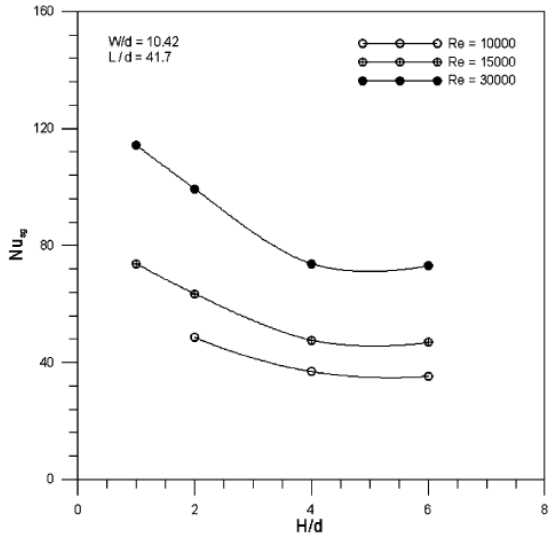

Figure 2.4: Effect of H/d on the Nusselt number at the stagnation point (Nu_{sg}) (San and Shiao (2006), Figure 8).

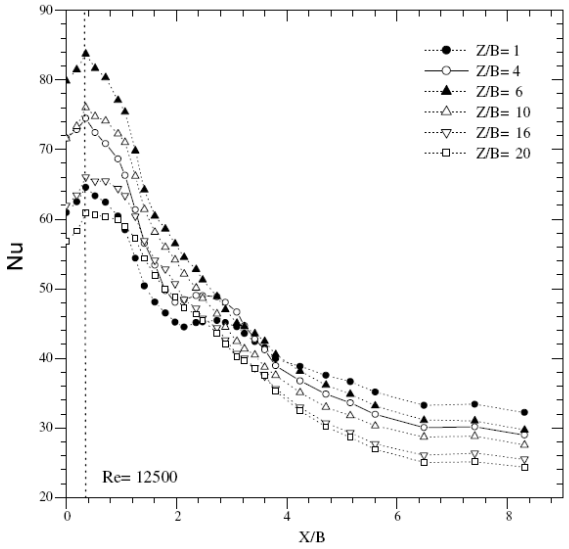

Figure 2.5: Lateral variation of the local Nusselt number at $Re = 12,500$ for several nozzle-to-plate Z/B spacing (Zhou and Lee (2007), Figure 9).

For a lower nozzle-to-plate spacing of $Z/B \leqslant 4$, the lateral distribution of the local heat transfer rate has two peaks. As the jet impinges onto the heater surface, the flow is forced to stagnate and then accelerate radially outward. At a lower nozzle-to-plate spacing, the formation of the convecting wall eddies on the impingement plate produces a larger turbulence intensity, leading a higher heat transfer rate there. The

combined effects of the turbulence intensity and the possible transition from laminar to turbulent flow caused the second peak phenomenon (Zhou and Lee, 2007).

The data suggest that the nozzle-to-plate spacing has a more significant influence on the local Nusselt number near the stagnation point. It can also be noted that nearly same Nu at the stagnation region is obtained at $Z/B = 16$ and 1 despite a larger difference of the axial distance (Zhou and Lee, 2007). Hence, if a more uniform heat transfer is sought, either a very large or a very small nozzle-to-plate spacing is preferred.

2.1.4 Effect of Jet-to-Jet Spacing in Multi-Jet Impingement

A considerable amount of research relating to multiple-jet impingement heat transfer was conducted in the past few decades. Gardon and Akfirat (1966) investigated the heat transfer characteristics of two-dimensional air jets impinging perpendicular to an isothermal flat plate. Kercher and Tabakoff (1970) measured the average Nusselt number of an in-line array of confined circular air jets impinging perpendicular to a flat plate. Metzger et al. (1979) investigated the heat transfer characteristics of in-line and staggered arrays of circular air jets impinging on an isothermal plate (San et al., 2007).

Saripalli (1983) conducted a flow visualization for multi-jet impingement. A fountain between two adjacent jets was observed. From the results of Saripalli's flow visualization, the heat transfer of an impinging jet array is believed to be strongly affected by jet interference *before* impingement and/or because of the jet fountain. The jet interference before impingement happens in the case of small jet spacing (Figure 2.6 [left]). For a small jet spacing, due to shear layer expansion, an interference between two adjacent jets will occur before impingement. This would weaken the jets and degrade the heat transfer of the jet array. The jet fountain is mainly attributed to the encounter of the two adjacent wall jets (Figure 2.6 [right]). The flow of the

fountain will recirculate and because of the entrainment effect, the heated air will reenter the core of the jets, affecting the heat transfer of the jet array.

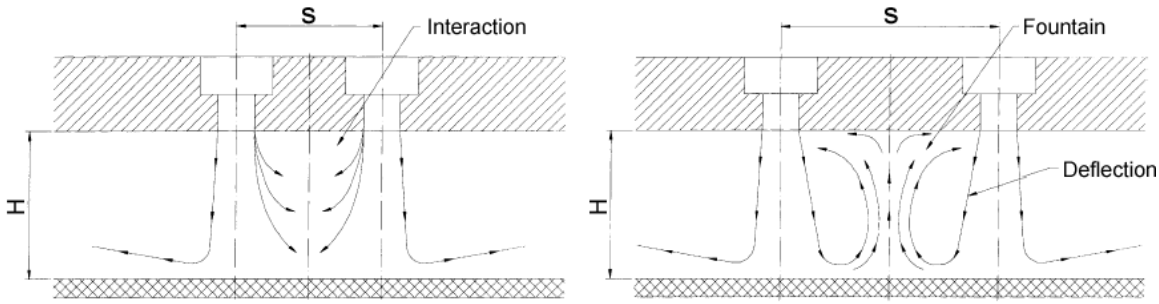

Figure 2.6: Jet interference before impingement [left] and jet fountain in a multi-jet impingement [right] ((San and Lai, 2001), Figures 4 and 5).

The interaction between the fountain and the two jets was found to increase with decreasing jet spacing. Behbahani and Goldstein (1983) obtained the local Nusselt number for staggered arrays of circular air jets impinging on a constant heat flux surface. A relative maximum of Nusselt number, between two adjacent jets in the streamwise direction, was clearly observed. The occurrence of this maximum is attributed to an increase of the turbulence intensity resulting from the interaction of the two jets (San and Lai, 2001).

Figure 2.7 exhibits the effect of Re on the stagnation Nusselt number for $H/d = 2.0$. Clearly, there exists a *maximum* Nu_{sg} for each curve. To the left of the maximum the jet fountain is strong. Thus, as the non-dimensional jet-to-jet spacing s/d increases, the fountain effect rapidly diminishes. This results in an increase of Nu_{sg} with s/d. To the right of the maximum point, due to an increase of the heated area under the jet array, Nu_{sg} begins to decrease with increasing s/d. Figure 2.7 indicated that the *optimum* s/d, corresponding to the *maximum* Nu_{sg}, is 8.0 for all Reynolds numbers. This implies that Re has very little effect on the optimum s/d (San and Lai, 2001).

With increasing jet-to-wall spacing H/d, the effect of the fountain becomes weaker. For $H/d = 3.0$, the optimum s/d, corresponding to the maximum Nu_{sg}, is 12.0. For jet-to-wall spacing $H/d > 3.0$ there exist two relative maxima of Nu_{sg} for $Re > 20,000$.

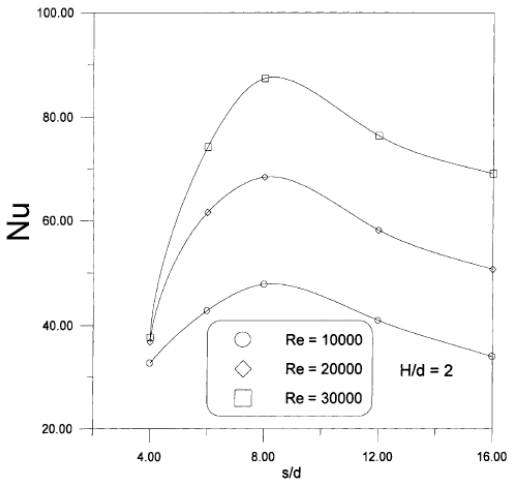

Figure 2.7: Effect of Re on the stagnation Nusselt number Nu_{sg} for $H/d = 2.0$ (San and Lai (2001), Figure 9). Clearly, an optimum value of the jet-to-jet spacing can be observed ($s/d \approx 8$).

Huber and Viskanta (1994) investigated the effect of jet-to-jet spacing on the heat transfer for confined jet arrays. The result reveals that, for large jet height (plate spacing), jet interference causes a significant degradation of the heat transfer. Dano et al. (2005) investigated the effect of nozzle geometry on the heat transfer for an in-lined array of impinging jets (San et al., 2007).

2.1.5 Modeling of Jet Impingement with k-ϵ Turbulence Models

The k-ϵ model is *a two-equation model* where model transport equations are solved to monitor the evolution of two turbulent quantities: the turbulent kinetic energy, k, and the turbulent dissipation, ϵ. Using these quantities one can form dimensionless groups like a lengthscale $l = k^{3/2}/\epsilon$, a timescale $\tau = k/\epsilon$, a turbulent viscosity $\nu_T = k^2/\epsilon$, etc. For this reason, two-equation models like the k-ϵ can be complete[1] (Pope, 2000).

The k-ϵ model is one of the most widely used turbulence models, and it is often incorporated in most commercial CFD codes. The concept was first introduced

[1] "A model is deemed complete if its constituent equations are free from flow-dependent specifications" (Pope, 2000). Only the material properties (e.g., ρ, ν), boundary and initial conditions need to be specified.

by Harlow and Nakayama (1968), but Jones and Launder (1972) are the creators of the *standard* k-ϵ (Pope, 2000). The *RNG* k-ϵ model was developed using Re-Normalization Group (RNG) methods by Yakhot and Orszag (1986) to re-normalize the Navier-Stokes equations. In the *RNG* model there is an additional term in the ϵ equation, which is an attempt to account for the different scales of motion through changes to the production term (CFD Online, 2007).

Salamah and Kaminski (2005) numerically investigated the heat transfer from an array of turbulent slot jets impinging on a flat plate using a k-ϵ model. Their numerical data showed good comparison with experimental data. Model results showed that the Nusselt number reaches a maximum at the stagnation point and decreases with distance along the plate. At some point, heat transfer may exhibit an increase due to transition to turbulence (Figure 2.8, right). There is also a local maximum in the Nusselt number at the midpoint between two jets, where the jets collide (Figure 2.8, left). The uniformity of heat transfer on the plate is a function of where and whether transition to turbulence occurs and the magnitudes of heat transfer at the stagnation and collision points. The k-ϵ modeling approach effectively captured both the stagnation region behavior and the transition to turbulence.

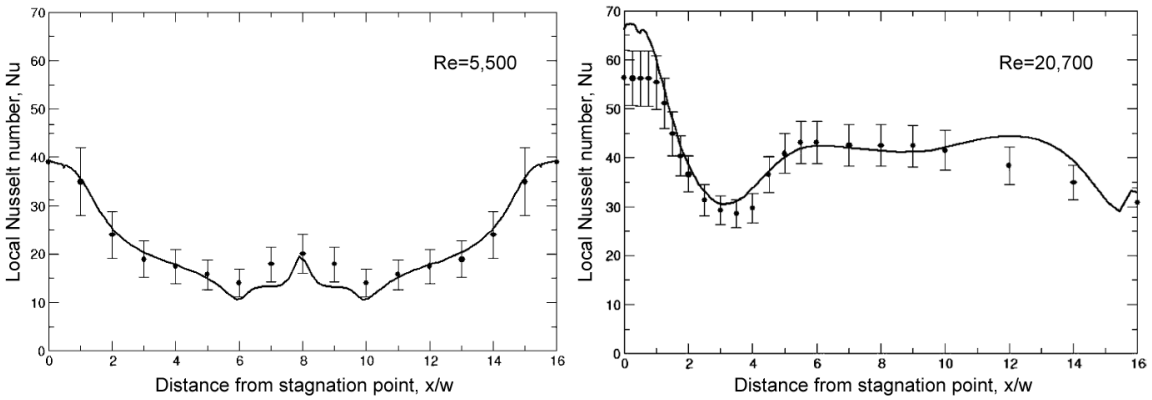

Figure 2.8: Comparison of prediction (lines) and experimental data (symbols). The Nusselt number is maximum at the stagnation point and a relative maximum in Nusselt number is at the midpoint between two jets, where they collide (adjacent jets, left). The heat transfer can undergo an increase due to transition to turbulence (single jet, right) ((Salamah and Kaminski, 2005), Figures 8 and 10).

El-Gabry and Kaminski (2005) used both the standard k-ϵ turbulence model and the low Reynolds number Yang-Shih turbulence model to simulate the heat transfer characteristics on a smooth surface under an array of angled impinging jets. The results show that both the numerical models were able to predict the periodic variation of the spanwise average Nusselt number on the impingement plate (San et al., 2007).

2.2 Leading Divertor Designs

This section details the leading He-cooled divertor designs studied in this thesis: the *ARIES* T-tube and the FZK "finger" module.

2.2.1 ARIES T-Tube Divertor Design

The T-tube divertor module is shown in Figure 2.9. Helium (He) enters the T-tube at 10 MPa and 600 °C, and exits at ~9.9 MPa and 680 °C. Preliminary design calculations show that a mass flow rate per unit length of 0.4 kg/(s·m) allows the divertor to withstand an incident heat flux of 10 MW/m^2 without exceeding the maximum allowable temperature for the tungsten alloy pressure boundary (Ihli et al., 2006; Raffray et al., 2006).

For each T-tube divertor module, the coolant enters a concentric cartridge through an inlet port located mid-way along its length (Figure 2.9, dark blue arrow). As shown in the cross-section of Figure 2.10 (right), this portion of the T-tube consists of two concentric tubes with a 1.25 mm wide annular gap; the flat tungsten armor layer is placed atop the outer tube. Both ends of the tubes are capped. The inner tube (cartridge) has a narrow (0.5 mm wide) slit along its entire length. The coolant enters the inner tube and is accelerated through the slit toward the inner surface of the outer tube (Figure 2.10).

The results shown previously in Figure 2.5 justify the choice of the small jet-to-wall spacing $H/B = 2.5$. A very small jet-to-wall spacing offers a more uniform heat transfer rate, which is sought in this application to limit the temperature gradients

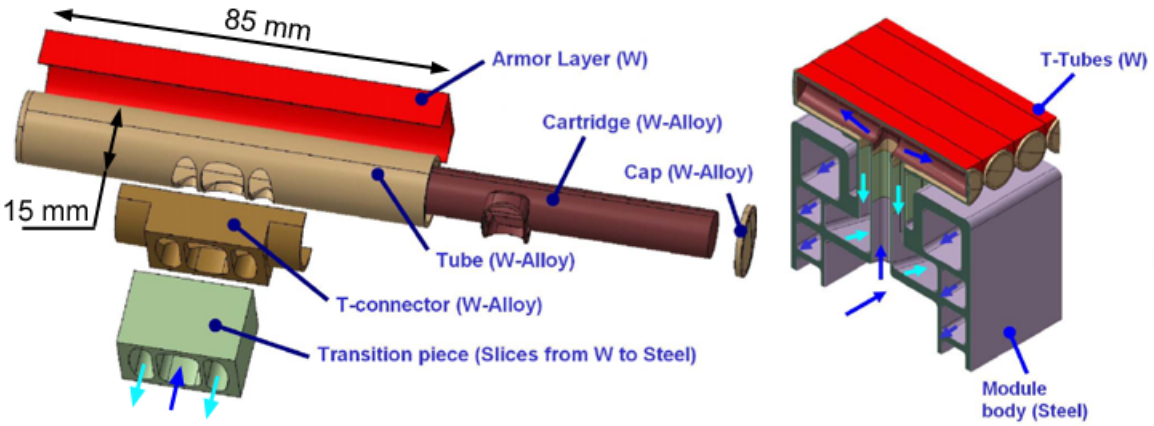

Figure 2.9: T-tube divertor module geometry (Ihli et al., 2005). The basic T-tube is shown on the left: the coolant will enter at the center location and exit at the two symmetrical outlets on the sides. The basic modules will then be connected side by side to form a target plate.

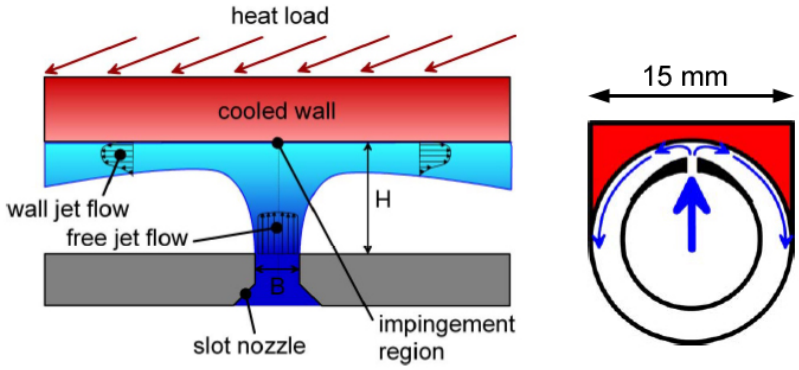

Figure 2.10: Sketch of the impinging jet cooling method (Ihli et al., 2005). The reference value for the slot width $B = 0.5$ mm and for the annular gap $H = 1.25$ mm.

in the T-tube module. The stagnation point flow generated by the impingement of the quasi-2D rectangular jet on this heated surface is used to cool the divertor with a moderate pressure drop. Downstream of the stagnation location, the He forms a turbulent wall jet along the inside surface of the outer tube, and is then removed through the two exit ports near the center of the module (Figure 2.9, light blue arrows).

As mentioned in Section 1.1.4, instabilities and other plasma events do not occur or are strongly reduced in stellarators; therefore the requirements on the armor layer

are much less stringent than those for tokamaks. A flat basic armor layer with a minimum thickness of 0.3 mm was used in these studies (Figure 2.9); an additional layer can, however, be brazed onto this basic armor if required.

2.2.1.1 Thermal Performance of T-Tube Divertors

As a part of the divertor design selection process, two and three-dimensional analyses were performed to assess the thermal performance of the helium-cooled T-tube divertor at nominal design and operating conditions.(Shin et al., 2005) Parametric analyses were also performed to assess the sensitivity of the thermal performance to changes in geometry and operating conditions due to manufacturing tolerances and/or flow mal-distribution between modules. All analyses were performed using the *FLUENT*® (V6.1) software package. The results show that for an incident heat flux of 10 MW/m^2 and a volumetric heat generation rate of 53 MW/m^3 (due to the incident neutrons), the maximum temperature for the tungsten alloy pressure boundary (outer tube) is 1523 K, which is well within the limits dictated by material properties (Ihli et al., 2006; Raffray et al., 2006); the corresponding pressure drop is 106 kPa, while the maximum tungsten armor layer temperature is 1700 K. These results were obtained using the standard k-ϵ turbulence model with enhanced wall function. Parametric analyses show that the calculated maximum temperatures are only slightly affected by the choice of the turbulence model used in the *FLUENT*® code. Parametric analyses were also performed to assess the sensitivity of the calculated thermal performance to changes in geometry (slit width and annular gap between cylinders) and operating conditions (inlet pressure and mass flow rate per unit length). Based on these analyses, it was concluded that the modular T-tube divertor design selected by the ARIES-CS team can accommodate an incident heat flux of up to 10 MW/m^2. It was also concluded that the T-tube design is "robust" with respect to anticipated changes in geometry and operating conditions resulting from manufacturing tolerances and/or

flow mal-distribution among the modules.

Close examination of the above-described thermal performance results obtained using the *FLUENT*® model show that the predicted heat transfer coefficient along the inner surface of the outer tungsten alloy tube is extremely high; values in excess of 40 kW/(m^2·K) were obtained near the stagnation point immediately opposite to the inner tube slit (Figure 2.11). Such values were judged to be "outside the experience base" for gas-cooled engineering systems. Hence, it was deemed necessary to experimentally validate these results.

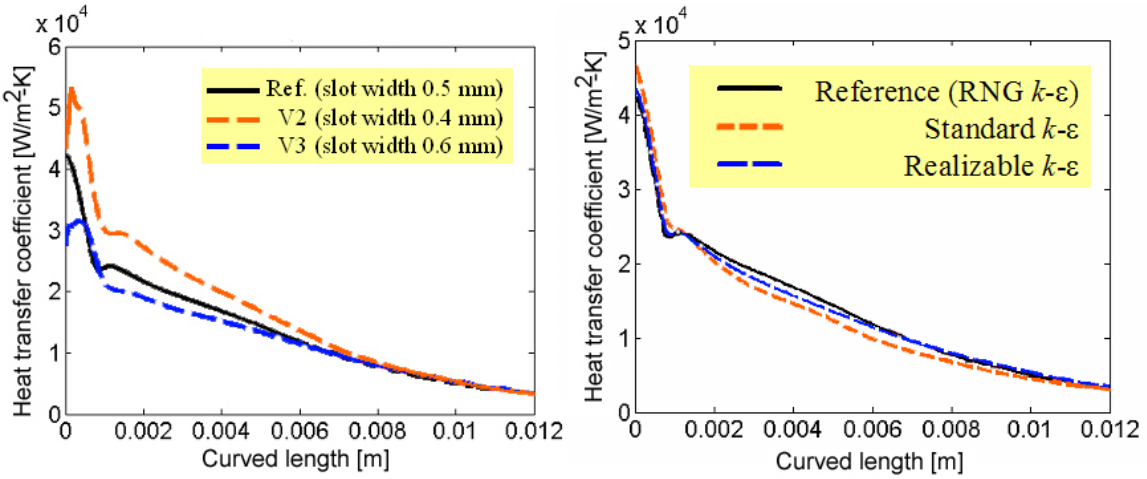

Figure 2.11: Heat transfer coefficient vs. position along the inner surface of the outer tube measured from the slit (2D *FLUENT*® simulations) (Shin et al., 2005). Slot width parametric results for reference turbulence model (RNG k-ϵ) [left]. The effect of turbulence model choice on the heat transfer coefficient is minimal [right] (reference slot width — 0.5 mm).

2.2.2 He-cooled Modular Divertor Concept with Jet Array

The Karlsruhe Research Center (FZK) in Karlsruhe, Germany has proposed several divertor designs which are capable of withstanding the required nominal incident heat load of 10 MW/m^2 using helium with an inlet temperature of 600 °C and at a pressure of 10.0 MPa (Section 2.3.6 and 2.3.7). The leading design relies on enhancement of the convective heat transfer coefficient through the use of multiple impinging jets. This design is called the helium-cooled Multi-Jet (*HEMJ*) divertor. The plasma-facing target is a tungsten armor plate which is attached to a tungsten-alloy (WL10) cap. A cylindrical steel cartridge that has twenty-four 0.6 mm diameter holes which surround a single 1.0 mm diameter hole in the center is secured below the cap (Figure 2.12). The jets are spaced by ≈ 2 mm on a staggered grid.

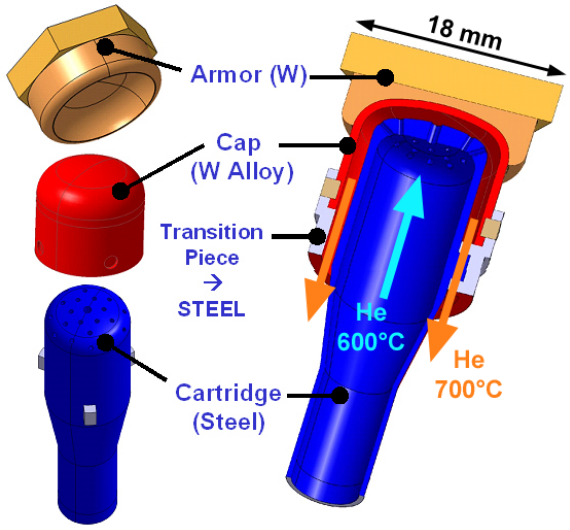

Figure 2.12: Schematic of the FZK HEMJ divertor finger module (Ihli, 2005).

Helium enters the cartridge and is accelerated through the twenty-five holes to create a jet impingement on the capped inner surface of the tungsten alloy. Downstream of the jet impingement location, the helium forms a turbulent wall jet along the surface of the cap (Figure 2.13). The helium then exits the divertor at approximately 700 °C by flowing through a $H = 0.9$ mm gap between the cartridge and the cap.

As in the T-tube case, the very small jet-to-wall spacing (H/D = 1.5 for the smaller holes) may have been chosen to obtain a more uniform heat transfer. However, the jet-to-jet spacing s/D = 3.33 is far from the optimum value s/D = 8.0 found in the literature for H/D = 2.0 (Figure 2.7).

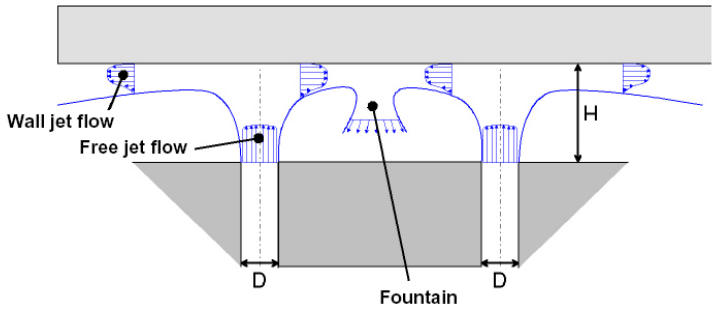

Figure 2.13: Multi-jet impinging cooling technique (Norajitra et al., 2005b)

.

2.2.2.1 Thermal Performance of HEMJ Divertors

Numerical and experimental analyses have been performed at FZK to characterize the divertor geometry, select appropriate materials, simulate heat removal capability, and develop high tolerance manufacturing of the proposed HEMJ divertor.(Norajitra et al., 2005b) Parametric analyses were performed to determine the sensitivity of the design to changes in geometry and operating conditions. Further experimental tests of the HEMJ divertor are needed to validate the heat removal capability predicted by computational fluid dynamics (CFD) software packages. These experimental tests are necessary because the high convective heat transfer coefficient (~50,000 W/(m^2·K)) predicted near the impinging jets is out of the experience base of high power density gas-cooled components.

2.3 Other He-cooled Divertor Designs

This section summarizes other He-cooled divertor designs with their heat transfer enhancement mechanism. This literature review was initially reported by Weathers (2007).

2.3.1 Porous Medium Concept

Heat transfer enhancement through the use of a porous medium has been proposed as a method capable of withstanding an incident heat flux of up to 5.5 MW/m^2 (Hermsmeyer and Kleefeldt, 2001; Kleefeldt and Gordeev, 2000). The heat transfer enhancement is due to two factors: the cooling surface area is greatly increased by the use of the porous medium; the irregular coolant flow pattern in the porous medium increases the turbulent mixing and thus the heat transfer capability (Incropera and DeWitt, 2002). This design will operate at 8 MPa with helium at an inlet temperature of 632 °C and an exit temperature of 800 °C. The predicted effective heat transfer coefficient is 20,000 $W/(m^2 \cdot K)$ (Hermsmeyer and Kleefeldt, 2001). Helium is forced through a slot at the top of the coolant inlet tube into a circular porous wick that has a void fraction of 40 % (Hermsmeyer and Kleefeldt, 2001). The helium flows through the wick around the outer surface of the coolant outlet tube before exiting through a slot on its bottom (Figure 2.14 [left]).

The coolant in the porous medium heats up in the azimuthal direction due to the local energy deposition rather than accumulating heat along the entire channel length. This feature is desirable for non-uniform heating profiles (Hermsmeyer and Kleefeldt, 2001). To obtain a uniform flow distribution, the coolant inlet tube flow area is decreased while the coolant outlet tube flow area is increased along the length of the divertor channel (Figure 2.14 [right]). A molybdenum or tungsten alloy are proposed for the construction of this channel. Since this enhancement method also relies on an increased surface area, it depends on the thermal conductivity of the

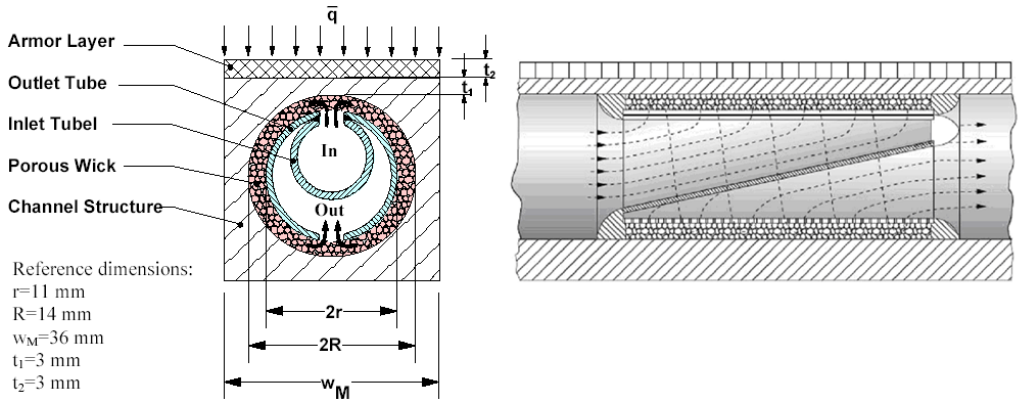

Figure 2.14: Cross-section of the porous medium divertor [left]. The coolant enters the inner tube, flows though the slot and the porous wick and finally exits through the slot at the outlet tube bottom. Longitudinal view of the porous medium concept [right]. The coolant enters the module on the left, flows though the slot and the porous wick and finally exits on the right (Hermsmeyer and Kleefeldt, 2001).

materials used for the porous medium (Baxi and Wong, 2000).

2.3.2 Multi-Channel Concept

The aim of the multi-channel divertor concept is to minimize thermal stresses by reducing the temperature difference across the divertor channel. It is designed to withstand an incident heat flux up to 5 MW/m^2 when operated at 14 MPa with helium entering at 500 °C. The estimated heat transfer coefficient varies from 15,000 to 20,000 W/(m^2·K) (Hermsmeyer and Kleefeldt, 2001). A double-wall coolant pipe is divided into halves with an insert to create a cold leg that consists of four sub-channels and a hot leg consisting of a single channel (Figure 2.15). The heat transfer coefficient is enhanced by the higher coolant velocities through the sub-channels of the cold leg. The larger relative hydraulic diameter of the hot leg section helps minimizing the pressure drop across the divertor (Hermsmeyer and Kleefeldt, 2001). However, the exit temperature of 551 °C does not offer an ideal input to the gas turbine power conversion system, when compared to the higher temperatures achieved with the T-tube or the HEMJ designs.

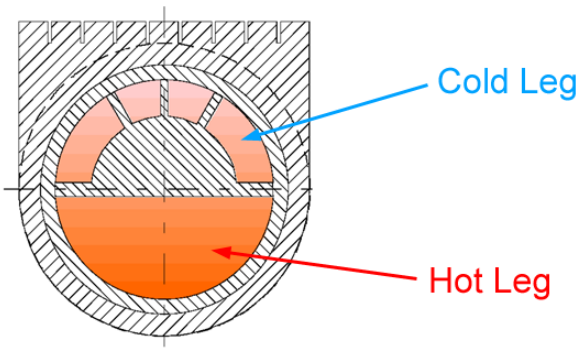

Figure 2.15: Cross-section of the multi-channel divertor concept (Hermsmeyer and Kleefeldt, 2001).

2.3.3 Eccentric Swirl Promoter Concept

In the eccentric swirl promoter concept, the heat transfer coefficient is enhanced by increasing the coolant velocity on the heated side of the coolant channel, in a similar manner to the multi-channel concept. A non-axisymmetric insert with helical fins that vary periodically around the spiral direction of the coolant channel is used to create the enhancement (Figure 2.16). This design is operated with helium at 14 MPa and capable of withstanding incident heat fluxes up to 5 MW/m^2. Helium enters the coolant channel at 600 °C and is heated to 800 °C. An effective heat transfer coefficient of 21,000 W/(m^2·K) can be obtained with this design (Hermsmeyer and Kleefeldt, 2001).

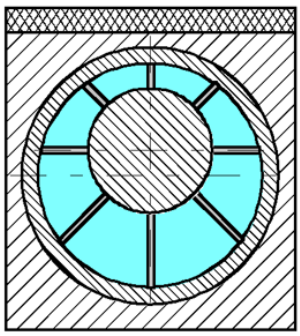

Figure 2.16: Cross-section of the eccentric swirl promoter divertor (Hermsmeyer and Kleefeldt, 2001).

2.3.4 Slot Concept

The slot concept evolved from the porous medium design. In this design, instead of having the coolant flowing azimuthally through a porous medium, a narrow gap of 0.1 to 0.2 mm is used (Figure 2.17 [left]). This eliminates bonding issues of the porous medium. The coolant channel diameters are tapered longitudinally in the same manner as for the porous medium design (Figure 2.14 [right]). Helium will operate at 14 MPa and an inlet temperature of 600 °C; the slot concept is able to withstand incident heat fluxes up to 5 MW/m^2 and deliver helium at 800 °C. The predicted average heat transfer coefficient is 14,000 W/(m^2·K) (Hermsmeyer and Kleefeldt, 2001).

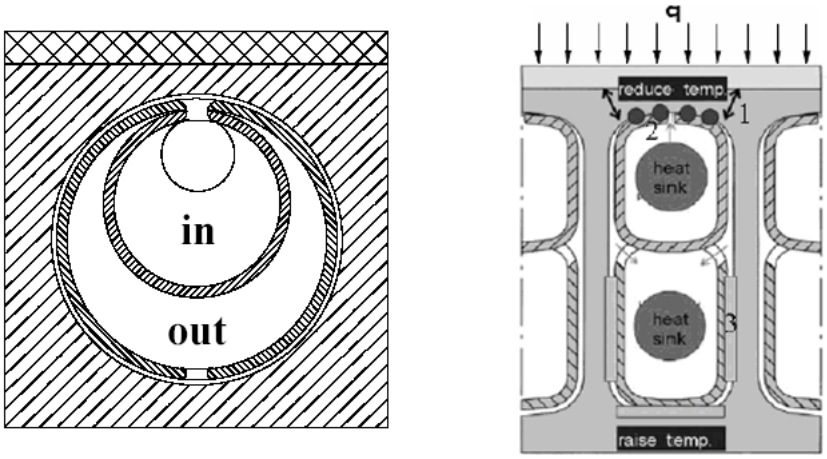

Figure 2.17: Cross-section of the slot divertor (left, Hermsmeyer and Kleefeldt (2001)) and modified slot principle divertor (right Norajitra et al. (2007)).

An enhanced version of the slot design that increases the peak heat flux capability to 10 MW/m^2 has been proposed (Hermsmeyer and Malang, 2002; Malang and Hermsmeyer, 2001). The modified design uses a narrow gap of 0.1 mm thickness to increase the coolant velocity upon exiting the inlet channel. The coolant then passes through an array of cylindrical studs and into the outlet channel. The maximum local heat transfer coefficient expected from the modified slot design is 56,000 W/(m^2·K) (Malang and Hermsmeyer, 2001).

2.3.5 High Efficiency Thermal Shield Concept

The high efficiency thermal shield (HETS) concept also enhances the heat transfer coefficient by creating a jet impingement on the heated surface. This design is based on an axi-symmetric cap geometry with a single jet impinging on a curved heated surface upon exiting a 7 mm diameter nozzle (Norajitra et al., 2005a). The coolant then flows through the gap between the inner nozzle structure and the cap (Figure 2.18). The HETS design was originally developed for water-cooling, but has been adopted for helium-cooling. It is capable of sustaining an incident heat flux up to 10 MW/m^2 when operating at 10 MPa with an inlet temperature of 600 °C (Boccaccini et al., 2005). In the HETS concept He would reach an exit temperature of 669 °C (Boccaccini et al., 2005). The predicted maximum local heat transfer coefficient for the HETS concept is approximately 55,000 - 60,000 W/(m^2·K) (Norajitra et al., 2005a; Karditsas and Taylor, 2002) and the typical average value is 30,000 W/(m^2·K) (Boccaccini et al., 2005).

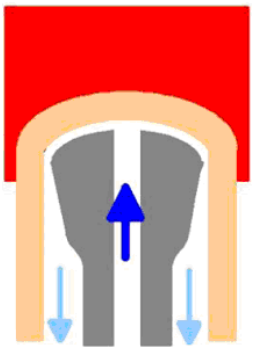

Figure 2.18: Cross section of the HETS divertor concept (Boccaccini et al., 2005).

2.3.6 He-cooled Modular Divertor Concept with Pin Array

The helium-cooled modular divertor concept with pin array (HEMP) is a variant of the modular cap geometry that is used for the HETS concept. Rather than using a jet impingement method, the coolant is forced through a staggered tungsten pin array (Figure 2.19). The staggered pin array enhances the heat transfer capability by

increasing the surface area and promoting turbulent mixing. This heat transfer enhancement mechanism results in a predicted maximum local heat transfer coefficient of 56,000 W/(m^2·K) in reference to the modified slot design using a pin array (Malang and Hermsmeyer, 2001) or 35,000 W/(m^2·K) from widely extrapolated data measurements (Kleefeldt and Gordeev, 2000). It is capable of withstanding an incident heat flux up to 10 MW/m^2 with helium operating at 10 MPa and an inlet temperature of 600 °C. The coolant would exit at a temperature of approximately 700 °C (Kruessmann et al., 2004). A challenge to the realization of the HEMP module is the effect of manufacturing tolerances on the pin array.

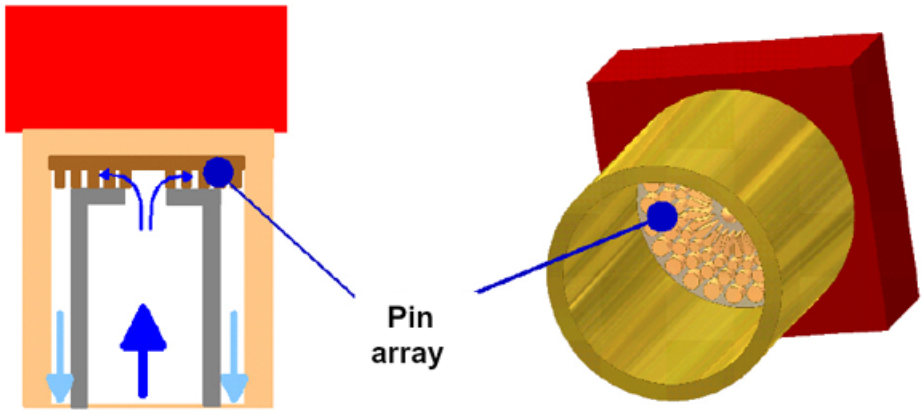

Figure 2.19: Multi-pin (HEMP) impinging cooling technique (Norajitra et al., 2005b).

2.3.7 He-cooled Modular Divertor Concept with Slot Array

A proposed improvement upon the HEMP concept is the helium-cooled modular divertor with slot array (HEMS). The HEMS concept uses a tungsten flow promoter in the form of radial slots to increase the surface area and thus enhance the heat transfer capability (Kruessmann et al., 2004). Similar to the HEMP design, the coolant enters the slot array from the center of the module. After flowing outward in the radial direction it exits the module by flowing through the gap between the inlet channel and outer support structure (Figure 2.20). The HEMS concept is capable

of withstanding an incident heat flux of 10 MW/m^2 under operating conditions of 10 MPa and helium inlet temperature of 634 °C. The maximum local heat transfer coefficient predicted for this design is 43,000 W/(m^2·K) and the average value is 24,000 W/(m^2·K). Helium would exit at an outlet temperature of 713 °C (Kruessmann et al., 2004).

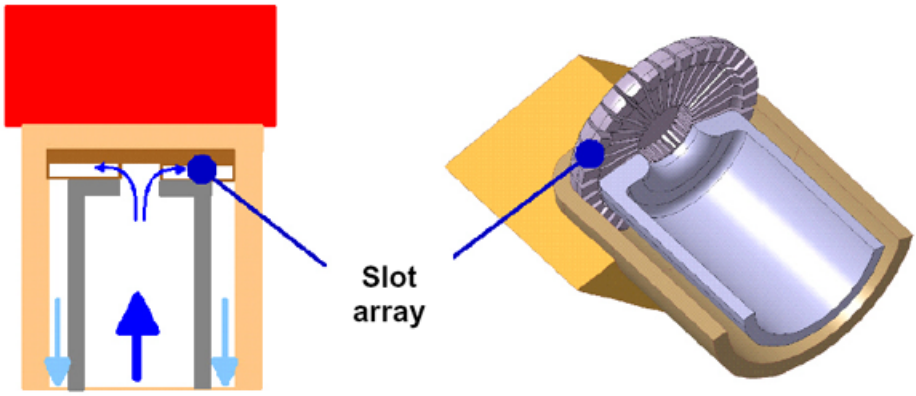

Figure 2.20: Multi-slot (HEMS) impinging cooling technique (Norajitra et al., 2005b).

2.3.8 Post-ITER He-cooled Divertor Designs

The fusion power plant DEMO that has been proposed as the follow-on to ITER would shift the primary focus from experimental fundamental studies to the ultimate application of electricity generation. In power plant designs, a high thermal efficiency and thus high temperature coolant is desired. Several methods of enhancing the heat transfer coefficient of helium-cooled divertors have been proposed and studied (Table 2.1). The results are obtained from numerical simulations. The operating conditions (i.e., inlet temperatures and pressure) are inputs to the predictions. Using a gas coolant requires significant heat transfer enhancement to withstand peak incident heat fluxes of 10 MW/m^2. Very few experimental studies have been carried out in what appear to be quite complex geometries with reverse flows, stagnation regions, and high-shear regions – all of which make numerical simulations more difficult.

To this end, this study is aimed at experimentally verifying the thermal performance of the leading divertor designs, namely the *T-tube* design and the *HEMJ* design. The data obtained in this investigation is compared with predictions from commercially available CFD codes used to design plasma facing components for magnetic fusion application.

Table 2.1: Comparison of Divertor Cooling Designs (*refers to a maximum local value).

Concept	**Heat Flux**	**HTC**	**Pressure**	T_{in}	T_{out}
	[MW/m^2]	[W/(m^2·K)]	[MPa]	[°C]	[°C]
T-tube	10.0	40,000*	10	600	680
HEMJ	10.0	31,000	10	630	700
		55,000*			
Porous Medium	5.5	20,000	8.0	632	800
Multi-channel	5.0	20,000	14	500	551
Eccentric Swirl	5.0	21,000	14	600	800
Slot	5.0	14,000	14	600	800
Modified Slot	10.0	56,000*	10	640	712
HEMP	10.0	35,000	10	600	700
		56,000*			
HEMS	10.0	24,000	10	634	713
		43,000*			
HETS	10.0	30,000	10	600	669
		57,000*			

CHAPTER III

T-TUBE APPARATUS: UNIFORM AZIMUTHAL HEATING

This chapter describes the experimental studies performed using a test section that simulates the planar jet impingement cooling concept of the T-tube divertor module. The test module is designed to produce an axisymmetrically uniform heat flux on the heated surface. While the actual divertors are subject to single-sided heating on the plasma-facing surface, the use of this simplified axisymmetric geometry provides the means to examine the behavior of the essential design feature, namely jet impingement cooling. Experimental work performed in this study using prototypical T-tube and HEMJ geometries is presented in Chapter 4 and 5, respectively. The remainder of this Chapter is organized as follows. First, the experimental apparatus and procedures used in this part of the investigation are described. Second, the numerical model corresponding to the test section geometry is presented. Finally, the experimental and numerical results are presented, compared and discussed.

3.1 Experimental Apparatus and Procedures

3.1.1 Test Section with Slit

The test section used to simulate the planar jet impingement concept used in the T-tube divertor module consists of two concentric tubes separated by an annular gap of 1.1 mm (Figure 3.1). The inner diameter of the outer tube (14.9 mm) and the outer diameter of the inner tube (12.7 mm) are nearly identical to those for the concentric tungsten alloy tubes of the T-tube divertor module (Section 2.2.1), while the annular gap thickness is in the range of gap dimensions (1.0 to 1.25 mm) considered in the

parametric studies of the divertor thermal performance (Section 2.2.1.1).

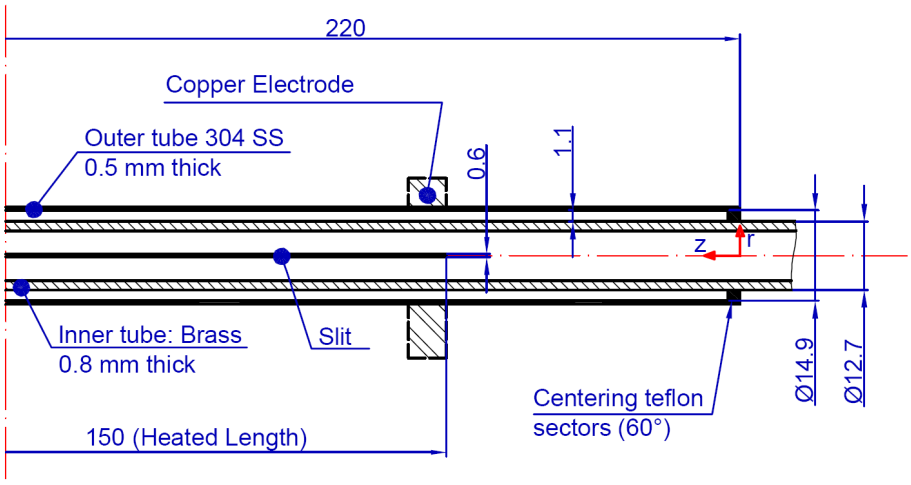

Figure 3.1: Schematic of the test section showing the outer and inner tubes, the electrodes and the slit.

The 12.7 mm OD inner tube is made of brass with a wall thickness of 0.80 mm. The total length of the inner tube is 660 mm; a slit of width $B = 0.60$ mm and length 150 mm centered along the tube length is cut through the tube wall using a micro-milling technique (Figure 3.2 [right]). Two 1.2 mm long (z-dimension) "bridges" span the slit at equal axial intervals (50 mm) along its length to ensure that the slit width remains constant along the axial direction (Figure 3.2 [right]).

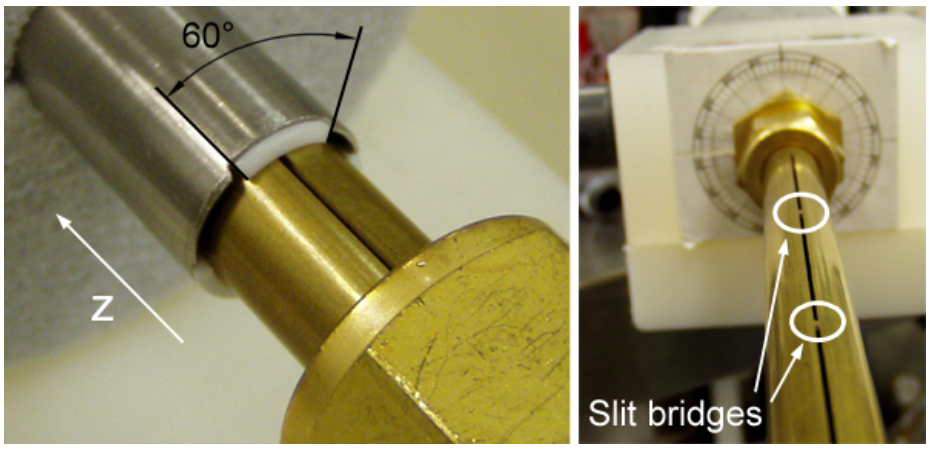

Figure 3.2: Close-up of the 0.6 mm wide slit and centering Teflon® sectors [left]. Close-up of the inner tube slit bridges [right].

The 220 mm long (z-dimension) outer tube is made of 15.9 mm OD thin-walled

SS 304 tubing with a wall thickness of 0.51 mm. A 150 mm long section of the outer tube centered along its 220 mm length and aligned with the slit in the inner tube is electrically heated by applying a DC voltage to the tube wall via two copper electrodes clamped around the tube; the power input to the test section, i.e., the surface heat flux on the outer tube, is set by controlling the applied voltage between the electrodes.

The voltage is supplied by a DC power supply (Rapid Power Technologies, Model #1198224) with an output range of 0–18 V and 0–2500 A, well in excess of the needed power input (50–540 W with a maximum current of 300 A). The power input is determined from the measured current and voltage drop; the current is measured using a calibrated 300 A shunt (Deltec Company MKB-600-100), while the voltage drop along the tube is measured using an Agilent data acquisition unit (model #34970 with A/D card #34901). The current and voltage are both measured using a four-wire method.

The outer tube is thermally insulated using high performance melamine foam pipe insulation (Figure 3.3). The temperature of the insulation outer surface is monitored with a IR thermometer (Raytek Raynger MX2).

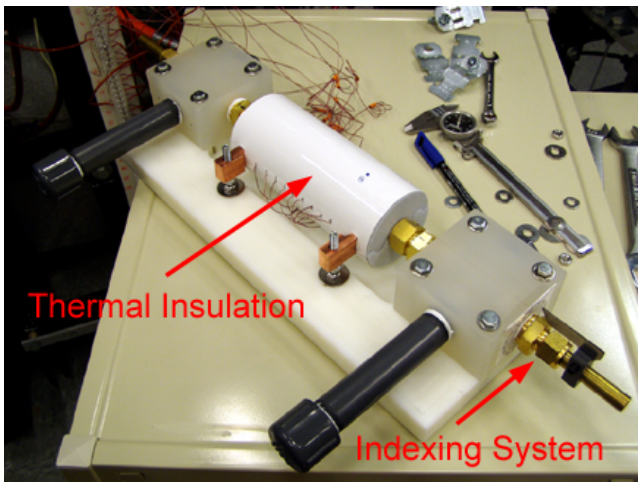

Figure 3.3: Complete assembly of the test section with the insulation and indexing system for the rotation of the inner tube.

Bored-through Swagelok® heat exchanger fittings are used to ensure that the axial position of the inner tube slit remains constant with respect to the heated section of the outer tube, and to ensure that the inner and outer tubes remain concentric. The uniformity of the annular gap between the tubes is maintained over the total axial (z) extent of the outer tube (220 mm) by placing three Teflon® spacers at each end of the outer tube; each spacer has an azimuthal extent of about 60° (Figure 3.2 [left]).

The outer surface of the outer tube is instrumented with nine self-adhesive E-type thermocouples (TCs) (*OMEGA*® SA1). The approximately 1 mm diameter TC beads are located at axial locations 1–9, corresponding to axial positions z = (20.6, 34.2, 47.8, 61.4, 75, 88.6, 102.2, 115.8, 129.4) mm (Figure 3.4a). All TCs are fixed to the surface and aligned at the same azimuthal location (Figure 3.5).

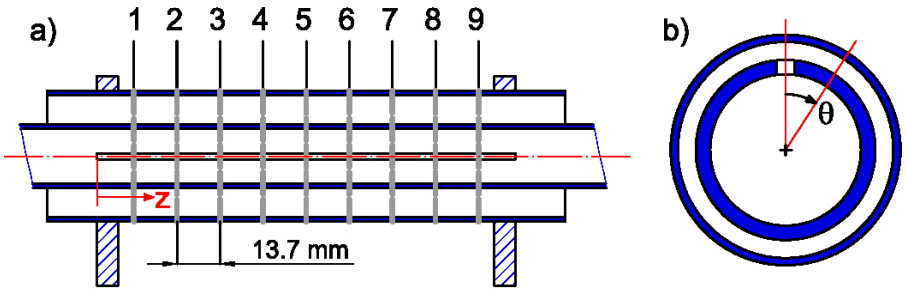

Figure 3.4: Definition of axial coordinate z showing the TC positions (a) and azimuthal coordinate θ (b).

Since the bored-through fittings allow rotation of the outer tube relative to the inner tube, the nine TCs can be positioned at any azimuthal location θ measured with respect to the slit in the inner tube (Figure 3.4b). Hence, azimuthal profiles of the outer tube surface temperature at the nine axial locations can be obtained by simply rotating the outer tube relative to the inner tube. Typically, data are obtained for θ = 0 to 360° in 20° increments. A scribe mark and an angular scale are used to indicate the azimuthal position of the thermocouple relative to centerline of the inner tube slit (Figure 3.6). The azimuthal resolution of temperature measurement is limited by the size of the thermocouple beads which have a diameter of ~ 1 mm,

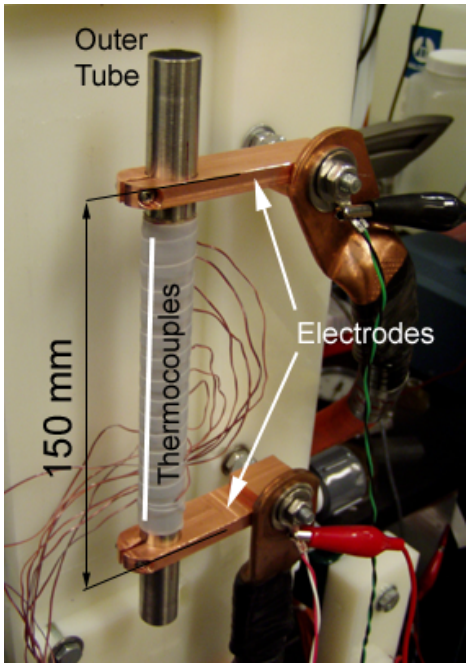

Figure 3.5: Image showing the outer tube, electrodes and nine thermocouples (TCs). The TCs are secured at nine different axial locations.

corresponding to an angular extent of 7.2°, and errors in the angular positioning, estimated to be about 2.5°; the estimated uncertainty in the azimuthal position based upon both of these factors of the temperature data is 7.6° (Appendix A).

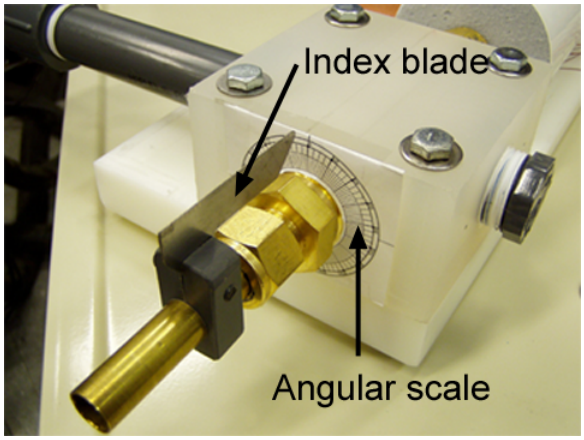

Figure 3.6: The angular indexing system used to set the azimuthal position θ of the TCs.

3.1.2 Test Section with Row of Holes

As discussed previously, maintaining a uniform slit width required leaving two bridges along the slit. Given the difficulties in machining the slit, even with these two bridges, and the even greater challenge of machining such a slit in the much harder tungsten alloy proposed for the T-tube (vs. the brass used here), an alternate test section where the slit in the inner tube was replaced by a row of fifty-one 1 mm diameter holes with a center-to-center spacing of 3 mm (Figure 3.7). This row of holes spans the 150 mm heated length of the tube.

Figure 3.7: This photograph shows the inner tube with the fifty-one jets. The jets diameter is 1 mm and they are 3 mm apart center-to-center.

3.1.3 Experimental Flow Loop

Although the prototypical T-tube divertor uses helium gas as its coolant, the experimental studies presented here used air as the working fluid. The thermal-hydraulic behavior of the T-tube is studied for a range of experimental parameters that match the important dimensionless groups corresponding to the operating conditions of the actual divertor module. As shown in Figure 3.8, air is supplied to the test section from a compressed-air line at gauge pressures up to ~690 kPa (100 psi); the air is discharged to the surroundings after flowing through the test module.

The test section inlet pressure is set by the air supply pressure regulator. The mass flow rate through the test section is controlled by a needle valve at the outlet, and calculated from measurements of the volume flow rate and the air density determined from the inlet and outlet temperatures and pressures. In some cases the valve was placed at the inlet, and the outlet pressure was atmospheric, since the air was

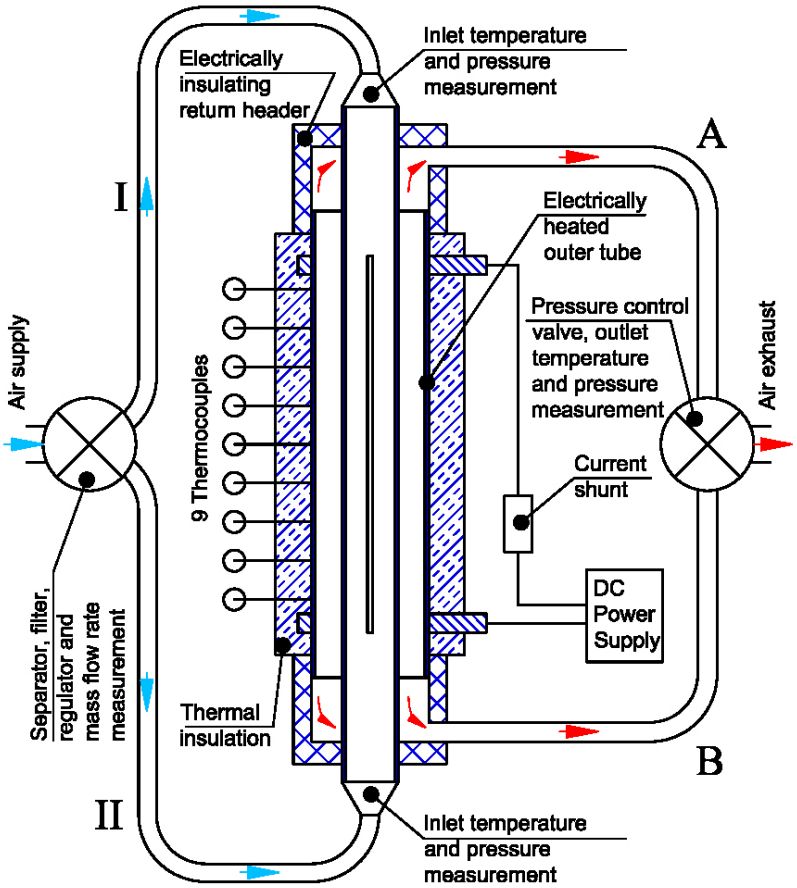

Figure 3.8: Schematic of the experimental flow loop detailing the flow paths and instrumentation (double inlet configuration).

vented to the surroundings. Multiple flow meters spanning different ranges of volume flow rates were used to ensure accurate measurements over the entire experimental parameter range. Both a calibrated orifice flow meter with a 8.0 mm diameter orifice (Meriam, S/N 647640-S1) upstream of the test section and a positive displacement gas flowmeter (Rockwell International R-315) at the exit were used to measure the volume flow rates.

The inlet and exit air temperatures are measured with E-type TCs (*OMEGA*® EMQSS-125E-6); the inlet and exit gauge pressures are measured using pressure transducers (*OMEGA*® PX180-060DV) and the pressure drop across the orifice is measured using differential pressure transducers with appropriate ranges (*OMEGA*®

PX26-xxxDV). Finally, the ambient pressure is measured using an absolute pressure transducer (*OMEGA*® PX302-015AV), and a mercury barometer.

The data acquisition system consists of a 60-channel data acquisition unit (Agilent #34970A, with three A/D cards #34901A, each with 20 channels), connected to a PC through a RS-232 serial cable. The Agilent Bench Link Data Logger 3 software package is used to configure the unit and monitor the data on the PC display. Only steady state data are stored for each experiment.[1]

3.1.4 Flow Configurations

Three different flow configurations have been examined using this test section (Figure 3.8 and 3.9); experiments have been conducted using all three flow configurations:

1. *Double inlet*, where the coolant enters the inner tube at both ends (I and II) and exits at both ends of the outer tube (A and B). This flow configurations is the closest to the expected flow configurations in the T-tube. Given the symmetry of this configuration, the flow will tend to "stagnate" near the center of the inner tube mid-way along the slit length.

2. *Counter flow*, where the coolant enters the inner tube only from one end (e.g., at I) and exits the outer tube at A, i.e., the same end. In this configuration, a fluid particle must exit at the same end as it entered, resulting in significantly reduced velocities near the opposite end.

3. *Parallel flow*, where the coolant enters the inner tube only from one end (e.g., at I) and exits the outer tube at B, i.e., the opposite end. A fluid particle in this configuration must traverse the entire axial extent of the text section before exiting, resulting in a fairly uniform flow along the length of the test section.

[1]The temperatures were assumed to have reached "steady-state" when the thermocouple probe readings sampled at 0.2 Hz remained constant within ±0.5 °C for 2–3 min.

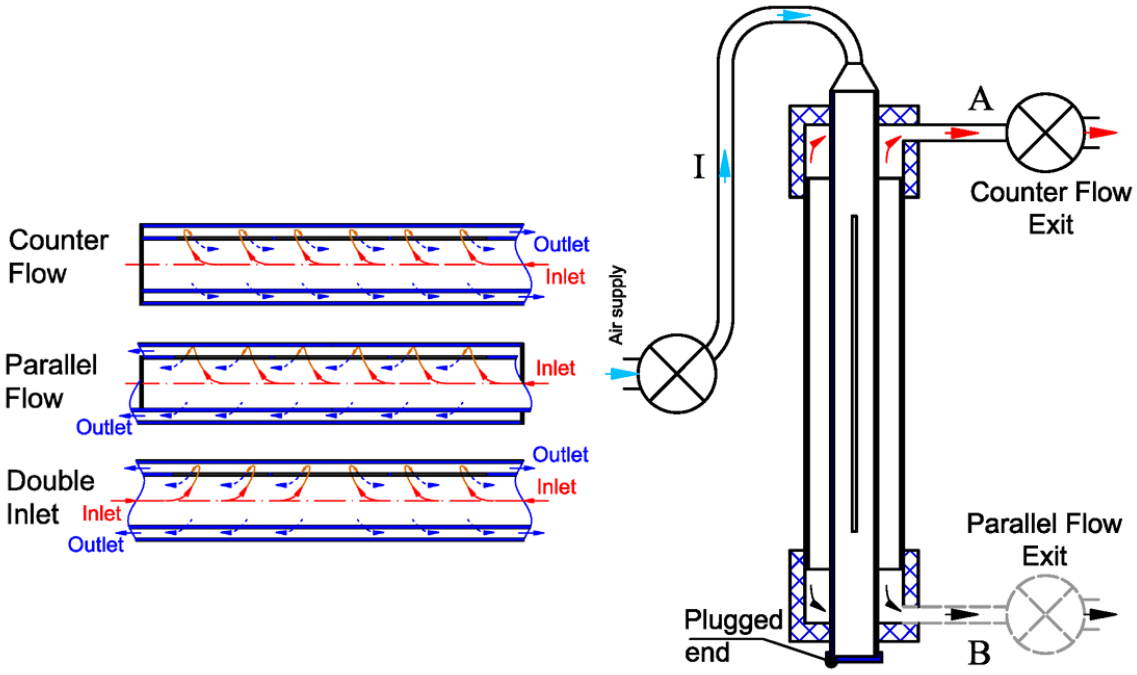

Figure 3.9: Sketch of the flows in the counter flow, parallel flow and double inlet flow configurations [left]. Schematic of the experimental flow loop for counter and parallel flow configurations [right].

3.1.5 Experimental Parameters and Procedures

The test conditions studied here bracket the values of the important dimensionless groups for the actual helium-cooled divertor module. The most important dimensionless group is the Reynolds number based on the *hydraulic diameter of the slit* in the inner tube $D_h = 2B$, the average speed $\overline{V}$ and the coolant properties at the test section inlet:

$$Re_{slot} = \frac{D_h \overline{V}}{\nu_{in}} = \frac{D_h \dot{m}}{A_{slot} \mu_{in}} \tag{3.1}$$

Table 3.1 compares the test conditions for three different experiments for the test section with the slit against the flow conditions for the T-tube divertor. The experimental Reynolds number varies between 2.9×10^3 and 2.0×10^4, vs. a nominal design value of 1.9×10^4 for the helium cooled divertor at its nominal operating conditions. The difference between the Prandtl numbers for air (0.71) and helium

(0.66) should have a small effect on the measured Nusselt number since for turbulent flows Nu depends on a Pr power which is less than unity (Gardon and Akfirat, 1966):

$$Nu \propto Re^{m_1} Pr^{n_1} \qquad m_1 \approx 0.6 \text{ for } 2.7 \times 10^3 \lessapprox Re \lessapprox 2.5 \times 10^4 \text{ and } n_1 = 0.4 \text{ for air} \quad (3.2)$$

Table 3.1: Comparison of thermal-hydraulic parameters for the proposed helium-cooled T-tube divertor and the experimental studies using air (double inlet flow configuration).

Parameter		**Air Cases**[2]			**He**
P_{oper}	[kPa]	103	207	240	10,000
ΔP	[kPa]	11.9	33.6	206	100
$\dot{m}_\ell$	[g/(s·m)]	25.3	86.7	180	400
$\dot{q}''_{avg}$	[MW/m^2]	0.018	0.042	0.077	10.0
T_{in}	[°C]	20	20	20	600
μ_{in}	[kg/(m·s)]$\times 10^{-5}$	1.85	1.85	1.85	4.16
Re	[-]	2,900	11,000	20,000	19,000
Pr	[-]	0.71	0.71	0.71	0.66

In most cases the power input was limited so that the temperatures on the outer surface of the tube did not exceed 177 °C, or the maximum rated temperature for the adhesive attaching the nine TCs. In all cases, the range of outer surface temperatures was maximized with this upper limit to minimize experimental errors. In a few rare cases, the outer surface temperature briefly exceeded this value, going up to 200 °C, during the experimental run. The value of the heat load has been therefore intentionally limited to avoid detachment of the TCs.

Each experiment is performed as follows:

1. With the flow loop closed, the test section is pressurized to a value close to that of the operating pressure using the pressure regulator at the inlet.

[2]The condition corresponding to the highest Re was tested only for the double inlet flow configuration.

2. The desired mass flow rate is set with the needle valve at the exit (or inlet).

3. The test section inlet pressure is then set to the desired value by adjusting the inlet pressure regulator (note that the pressure will change after step #2 because the flow will introduce a pressure drop).

4. The power input is then slowly increased to the desired input value (based on the limitations described above) by adjusting the output current of the power supply.

5. Once the temperatures in the test section reached steady state, the axial temperature profiles at the instrumented angular position θ is recorded (all nine TCs).

6. The azimuthal position of the instrumented location, θ, is adjusted (usually by 20°) by loosening the Swagelok nuts and rotating the inner tube (Figure 3.6).

7. Repeat steps 5 and 6 until the entire range of theta from 0 to 360° is complete for a given mass flow rate, power input, and inlet pressure and temperature (within experimental error).

The experimental set-up (steps 1–5) required about 30–45 min, while each experiment at a given θ (steps 6 and 7) took between 5 and 15 min, depending on θ. An experimental run spanning the entire 360° range usually took 3–4 h. Table 3.2 summarizes the experiments performed for the three flow configurations. For each experiment, data were acquired at nineteen angular positions from 0° to 360° in 20° increments. These experiments are referred to with the designation "*TS*#" where the "*T*" refers to the "tube" geometry and the "*S*" refers to the slot configuration.

Table 3.2: List of experiments for the T-tube test module with axisymmetrically uniform heating. Each experiment spans nineteen distinct angular positions.

Exp. #	$\dot{m}$ ($\dot{m}_\ell$) [g/s] ([g/(s·m)])	Re [-]	P_{in} [kPa (psi)]	ΔP [kPa (psi)]	$\dot{Q}$ [W]	$\dot{q}''_{avg}$ [kW/m^2]
Double Inlet						
*TS*1	3.8 (25.3)	2,900	103 (15)	11.9 (1.72)	130	18.6
*TS*2	13 (86.7)	11,000	207 (30)	33.6 (4.87)	296	42.3
*TS*3	27 (180)	20,000	241 (35)	206 (29.9)	539	77.0
Counter Flow						
*TS*4	3.9 (26)	2,900	29.2 (4.23)	29.2 (4.23)	52	7.43
*TS*5	14 (93.3)	11,000	241 (35)	210 (30.5)	120	17.1
Parallel Flow						
*TS*6	2.5 (16.7)	1,800	8.2 (1.19)	8.2 (1.19)	90	12.9
*TS*7	14 (93.3)	11,000	281 (40.8)	108 (15.6)	165	23.6

Experiments on the test section with a row of holes (instead of a slot) were performed over a range of parameters similar to those for the test section with a slit (Table 3.3). The Reynolds number for these experiments, however, is based on the *diameter of the hole D*:

$$Re_{holes} = \frac{D\overline{V}}{\nu_{in}} = \frac{D\dot{m}}{A_h \mu_{in}} \tag{3.3}$$

Table 3.3: Comparison of thermal-hydraulic parameters for the proposed helium-cooled T-tube divertor and the test section with a row of holes using air as the coolant (double inlet flow configuration).

Parameter		**Air Cases**			**He**
P_{oper}	[MPa]	0.414	0.414	0.414	10.0
ΔP	[kPa]	9.3	36.7	75.2	100
$\dot{m}$	[g/s]	7.5	14	18	34
$\dot{q}''_{avg}$	[MW/m^2]	0.028	0.043	0.057	10.0
T_{in}	[°C]	20	20	20	600
μ_{in}	[kg/(m·s)]×10^{-5}	1.85	1.85	1.85	4.16
Re	[-]	10,000	19,000	27,000	19,000
Pr	[-]	0.71	0.71	0.71	0.66

Because the area of the holes ($A_h = 40$ mm^2) is much smaller then the area of the slot ($A_{slot} \sim 90$ mm^2), the air mass flow rate $\dot{m}$ required to match Reynolds numbers

is much less for this test section geometry than for that with the slit. The maximum *Re* for this test section geometry is therefore significantly higher than that for the test section with the slit (cf. Table 3.1). The double inlet, parallel and counter flow configurations were also studied, as summarized in Table 3.4. These experiments are referred to with the designation "*TH#*" where the "*H*" refers to the multiple holes arrangement versus the slot opening used in the "*TS#*" experiments.

Table 3.4: List of experiments for the T-tube test module for the test section with a row of holes. All experiments were performed at a gauge pressure $P = 414\ kPa\ (60\ psi)$. Each experiment spans nineteen angular positions.

Exp. #	$\dot{m}$ [g/s]	Re [-]	ΔP [kPa]([psi])	$\dot{Q}$ [W]	$\dot{q}''_{avg}$ [kW/m^2]
Double Inlet					
*TH*1	7.4	10,000	9.3 (1.3)	200	28.6
*TH*2	14.3	19,000	36.7 (5.3)	300	42.9
*TH*3	20.1	27,000	75.2 (11.1)	400	57.1
Counter Flow					
*TH*4	7.5	10,100	22.0 (3.2)	200	28.6
*TH*5	14.3	19,000	90.9 (13.2)	300	42.9
*TH*6	19.0	25,000	152.8 (22.2)	400	57.1
Parallel Flow					
*TH*7	7.4	10,000	18.6 (2.7)	200	28.6
*TH*8	14.3	19,000	80.4 (11.7)	300	42.9
*TH*9	19.5	26,400	143.2 (20.8)	400	57.1

3.2 Numerical Modeling

As described before, *a priori* numerical simulations were performed to predict the wall temperature distributions and heat transfer coefficients for the experimental test module geometry and conditions using the same methodology (i.e., FLUENT® code options) used to analyze the thermal performance of the actual helium-cooled T-tube divertor (cf. Sec. 2.2.1.1). This section describes these numerical simulations; the predicted and measured heat transfer coefficients are compared in Section 3.3.2.

3.2.1 Model Geometry

Depending on the flow configuration to be used in an experiment, either a quarter- (double inlet) or half-model (counter and parallel flows) geometry is used in the numerical simulations (Figure 3.10). Both models included the two concentric tubes and the surrounding insulation; the quarter-model also included the electrodes connected to the outer tube, fittings, and mounting brackets. Inclusion of these components is necessary to assure an accurate energy balance consistent with the measurements.

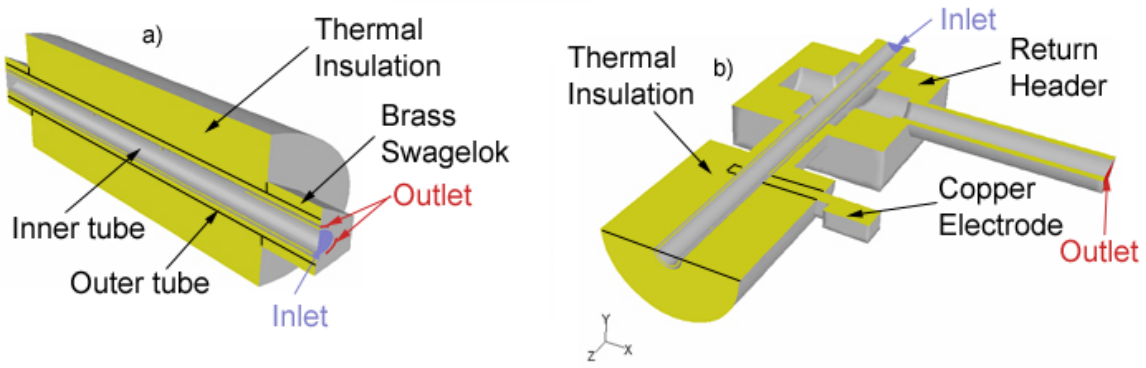

Figure 3.10: Typical half- and quarter-models showing the two tubes surrounded by insulating foam (a) and the tubes, foam, mounting brackets and electrodes (b).

Since geometric models such as the one represented in Figure 3.10b were not computationally efficient with respect to the simpler geometry represented in Figure 3.10a, the former option has been discarded once the energy balance was validated and the heat losses were experimentally verified. This model simplification *did not affect* the prediction of temperature and heat transfer coefficient profiles, but rather influenced the prediction of outlet temperature and pressure drop in the test section, as compared to the experimental measurements.

3.2.2 Grid Generation

The geometric wireframe and surfaces have been constructed using 3D CAD software (Solidworks® 2006). The surface mesh and 3D volume grid have been implemented

in *Gambit*® 2.2.30. Simulations are carried out using computational grids with up to 10^6 cells (Figure 3.11).

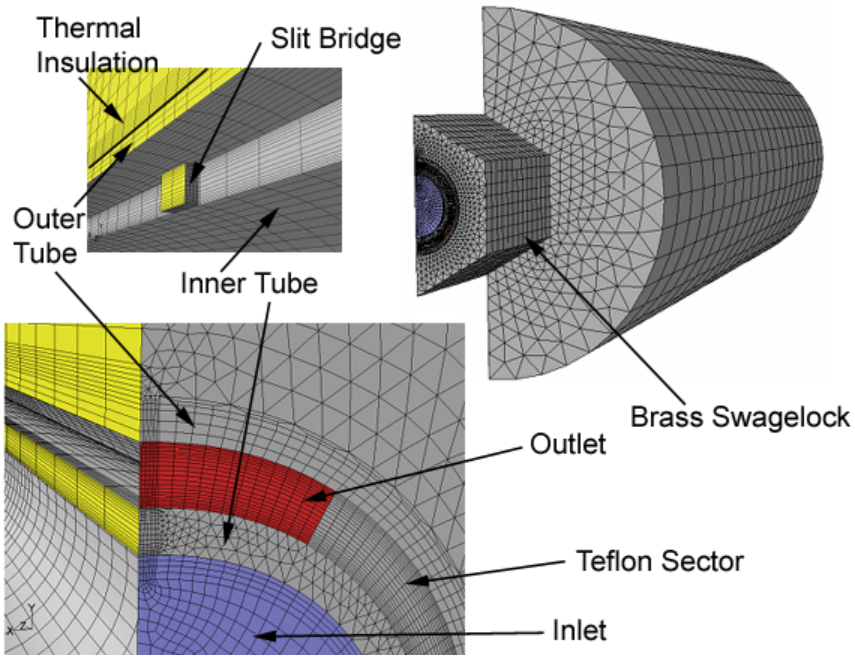

Figure 3.11: Typical computational grids. The use of multi-block technique allowed the stratification of the grid in the small gap between inner and outer tubes.

Because of the extremely large aspect ratio of the slit and the gap, the construction of the grid has been challenging. While the impinging jet width (0.6 mm) is comparable to the annular gap size (1.1 mm), the length of the heated tube is two orders of magnitude greater (200 mm). For this reason, after importing the CAD model into the meshing software, the geometric volumes were split into smaller blocks, in order to optimize the quality of the grid (*multi-block technique*). By using this technique it was possible to create layered grids in the small gap between the inner and outer tube, by sweeping the face mesh generated on the inlet and spacer faces along the axis of the tubes (Figure 3.11). Furthermore, it was preferable to "sacrifice" the axial resolution of the grid and refine the resolution in the radial and azimuthal directions. This grid construction choice is consistent with the *nearly 2D nature* of the impinging jet flow, whose features are essentially independent of the z-position. Successful

preparation of the grid usually took 2–3 weeks.

The numerical models used for test section with the row of holes are identical to those for the test section with the slit except, of course, for the inner tube geometry. A grid with a finer mesh near the impinging region was again developed from the CAD model using Gambit, as shown in Figure 3.12. Although the radial and azimuthal grid spacing were identical to those used for the test section with the slit, the axial grid spacing was reduced to resolve the individual round jets.

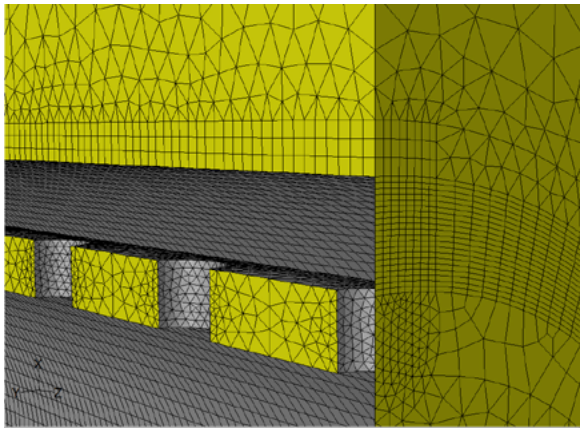

Figure 3.12: Close-up of the computational grid for the T-tube test module with a row of holes. This geometry requires a finer axial grid resolution compared to the rectangular jet grid.

The presence of round jets, vs. a rectangular jet resulted in a strongly *three-dimensional* flow. This required a much finer grid resolution than that used for the geometry with the slit. Because of limitations in computational resources, grid convergence was only achieved for the quarter-model geometry (used for the double inlet flow configuration). Grids with up to 1.3×10^6 cells (960,000 nodes) and 2.0×10^6 cells (800,000 nodes) were used for the quarter- and half-model geometries, respectively.

3.2.3 Boundary Conditions

The boundary conditions (BCs) used in the simulations are defined in *FLUENT*® and they specify:

- $\dot{Q}_v'''$: The power input to the outer tube, i.e., the uniform heat generation rate per unit volume [W/m^3] (experimentally produced by Ohmic heating).
- $\dot{m}_{in}$: Coolant mass flow rate at the inlet [kg/s].
- T_{in}: Coolant temperature at the inlet [°C].
- P_{out}: Gauge exit pressure [Pa].
- P_{oper}: Operating pressure [Pa].
- h_{amb}: Heat transfer coefficient for accounting heat losses from the test module to the surroundings (i.e., outer insulation surface) [W/(m^2·K)].

The latter is based on estimates made using natural convection correlations from vertical cylinders ($h_{amb} \sim$ 5–10 W/(m^2·K)), while all other parameters correspond to their respective measured values for each experiment to be analyzed. In addition to the above BCs, all the material properties had to be defined. Table 3.5 shows the material property values used in the numerical simulations.

Table 3.5: Properties of the materials used in the numerical calculations.

Material	ρ [kg/m^3]	k [W/m·K]	c [J/kg·K]
304 SS (Heated tube)	8027	16.26	502
Brass (Inner tube)	8800	116	380
Melamine (Insulating foam)	11	0.0375	1210
Nat. Polypropylene (Headers)	905.5	0.16	1900
PVC (Outlet tubes)	1400	0.147	1050

The experimentally measured (Section 3.1.1) external temperature of the insulation has been compared to the model prediction, in order to validate the values of h_{amb} and obtain a more realistic energy loss to assure accuracy of the overall energy balance. Because of the relatively low power input used in these experiments, the experimental temperature of the insulation surface ranged between 35°C and 45°C.

The numerical prediction was usually in good agreement with the measured surface temperature values (within ±5°C). Exact matching of the heat loss, however, has been challenging, since it depends on the properties of the thermal insulation.

The air density was calculated using the ideal-gas equation of state. The specific heats (c_p, c_v), thermal conductivity (k) and molecular viscosity (μ) of the air at room temperature were kept constant during the calculations (the default in *FLUENT*®).

3.2.4 Convergence of Solution

From a numerical standpoint, the convergence of the solution is deemed acceptable once the equations scaled residuals do not change with further iteration steps (Figure 3.13). Grid convergence studies with 2×, 1.2× and 1.3× the axial, azimuthal and radial resolutions, respectively, indicated that the CFD solution had converged for all cases shown here. In most cases, the CFD solutions converged within 5 h on a Pentium® IV 3.4 GHz workstation with 2 GB RAM.

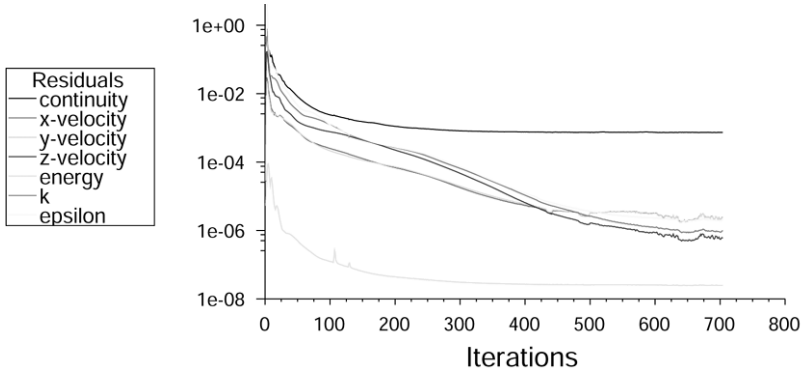

Figure 3.13: Plot of the scaled residuals of the equations involved in the calculation showing convergence of the solution.

3.3 Results and Discussion

3.3.1 Nominal Test Case *FLUENT*® Results

The *nominal test case* refers to the test for which conditions are the closest to the actual T-tube module operating conditions. For the experimental test module described before, the nominal test case is the double inlet configuration at $Re = 20,000$

(Exp. #*TS*3). In this section the numerical results of the nominal test case will be shown and general thermal-hydraulic behavior will be deduced.

Figure 3.14 shows the temperature profiles on the cooled surface of the outer tube, i.e., the heated tube for the double inlet configuration (Exp. #*TS*3). The top portion (blue) represents the region of jet impingement. As one would expect, the temperatures are the lowest in this area. While moving away from the jet stagnation point, the temperatures progressively increase and reach a maximum in the region opposite to the jet (red), where the flow tends to stagnate.

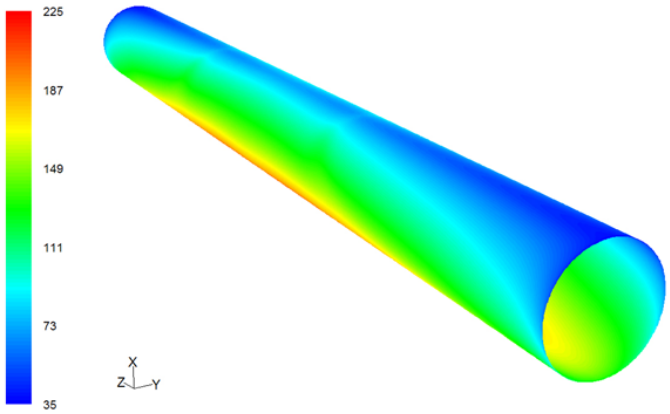

Figure 3.14: Contours of wall temperature (°C) on the cooled surface of the heated tube for double inlet configuration ($Re = 20,000$).

In addition, it is worth noting that the lower portion of the tube (red) experiences the highest temperature because the heating is *uniform* along the circumference, whereas the jet is cooling on a *single stagnation line*. Hence, it is reasonable to expect a "hot region" in this portion of the heated tube. The area of the cooled surface is $A_{cooled} = 7 \times 10^{-3}$ m^2 and therefore the average heat flux is $\dot{q}''_{avg} = 0.077$ MW/m^2 (Exp. #*TS*3), based on the total power input $\dot{Q} = 539$ W.

Figure 3.15 shows the wall heat transfer coefficient (HTC) profiles on the cooled surface of the outer tube for the same case described above. The qualitative thermal-hydraulic behavior discussed above for the temperature profiles is evident from for the contours of the heat transfer coefficient. The top portion of the tube (red) represents

the region of jet impingement. Here the heat transfer coefficient is maximum, because of the high-velocity coolant issuing through the slit. While moving away from the jet stagnation point, the heat transfer coefficient quickly drops and reaches a minimum at the bottom region of the tube (blue).

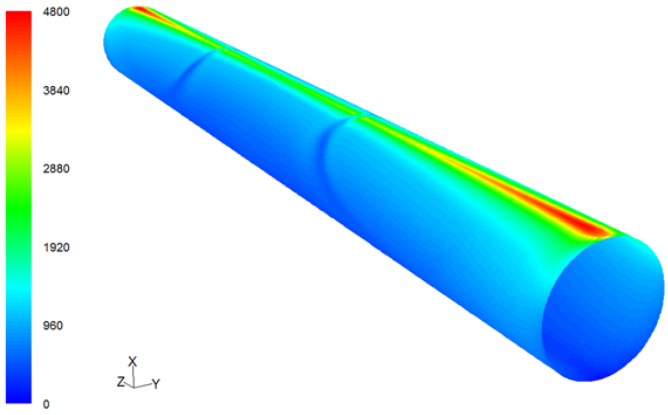

Figure 3.15: Contours of wall heat transfer coefficient (W/m^2·K) on the cooled surface of the heated tube (double inlet, $Re = 20,000$).

The contours in Figure 3.15 show the *axial* degradation of the heat transfer coefficient. The axial gradients are due to the flow distribution in the test module. The coolant tends to "escape" more easily near the outlets, and because the inlets and outlets are on the same sides (see Figure 3.8 and Figure 3.9) the flow forms a *stagnation plane* at the axial center of the test module. Therefore, the highest cooling effect is experienced near the outlets, while the lowest cooling effect is experienced at the center location.

Clearly the peak values shown in Figure 3.15 (~4.8 kW/(m^2·K)) are well below the calculated peak values for the actual helium-cooled T-tube divertor (~50 kW/(m^2·K)). This is expected since the thermal conductivity of helium at 10.0 MPa and 600 °C is more than an order of magnitude higher than that for air at 0.3 MPa and 20 °C so that for the same value of the local Nusselt number (Equation 3.4), a significantly higher HTC is obtained in the helium-cooled system with the same geometry and

Reynolds number (Table 3.6).

$$Nu = \frac{D_h \cdot h}{k} \tag{3.4}$$

Table 3.6: Effect of coolant thermal conductivity on the predicted HTC for air and helium.

Coolant		**Helium**	**Air**
Inlet Temperature	[°C]	600	20
Inlet Pressure	[MPa]	10	0.414
Re	[-]	19,000	20,000
k^a	[W/(m·K)]	0.3326	0.02517
k^b		0.323	0.0263
Predicted h_{max}	[W/(m^2·K)]	50,000	4,800

[a]Source: Engineering Equation Solver (EES) V7.964 (08/21/07)
[b]Source: Incropera and DeWitt (2002).

Another interesting flow feature is evident from the depicted contours in Figure 3.15. The darker blue "curls", at approximately 1/3 and 2/3 of the axial length of the tube, show the effect of the bridges left uncut in the rectangular jet. This blockage region helps in visualizing the flow path in the test module. After entering the inner tube on each end, the coolant flows through the slit, impinges the inner surface of the outer tube and then flows along the gap between the tubes as a turbulent channel flow. The coolant, however, needs to exit the test module once again through each end: it is this feature that forces the axial component of the flow and therefore its *three-dimensionality* (Figure 3.16). While the flow wake left downstream of the bridges affects the *local* heat transfer coefficient, it does not seem to affect the temperature profiles, because of conduction in the tube wall (Figure 3.14).

Figure 3.17 shows the coolant path lines for the counter and the parallel flow configurations. In both cases, the coolant highest speeds are experienced in the narrow passage between the centering Teflon® sectors. Because of the low operating pressure, the flow was nearly choked (with Mach number $M = 1$) at this location in some of the counter flow cases. Although the path-lines show similar patterns for

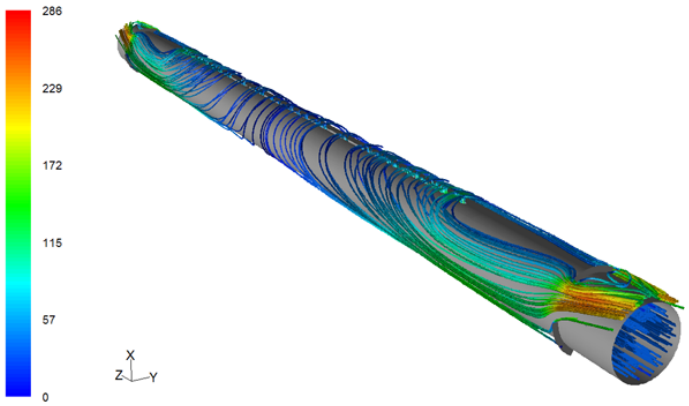

Figure 3.16: Coolant path lines colored by velocity magnitude [m/s] (double inlet, $Re = 20,000$).

both cases, the inlets are located at *opposite sides* of the test section. In both cases, however, the flow is stagnant in proximity of the plugged end (Figure 3.9). Here the cooling effect is minimum because of the low coolant speed. For both scenarios, on the other hand, the maximum cooling effect is experienced in vicinity of the outlets, where the coolant speeds are higher (as in the double inlet case).

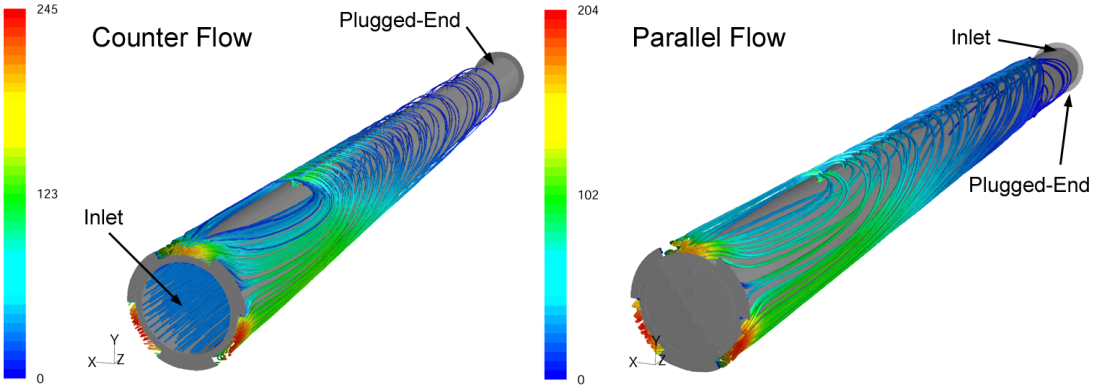

Figure 3.17: Coolant path lines colored by velocity magnitude [m/s] for counter [left] and parallel [right] flow configurations ($Re = 11,000$).

Typical results for the HTC prediction for the test section with the row of holes are shown in Figure 3.18 [left]. This contour plot should be compared with Figure 3.15. The maximum predicted values for the HTC are very similar (because Re are the same), but the distribution is quite different. While the azimuthal decay seems to be

comparable, the axial HTC gradients are far more uniform. Although locally the heat transfer coefficient undergoes steep gradients, the wall temperatures are not affected because of the conduction in the tube (Figure 3.18 [right]). The cooling performance, however, is maintained along the axial extent of the tube because of the uniform flow distribution across the jets.

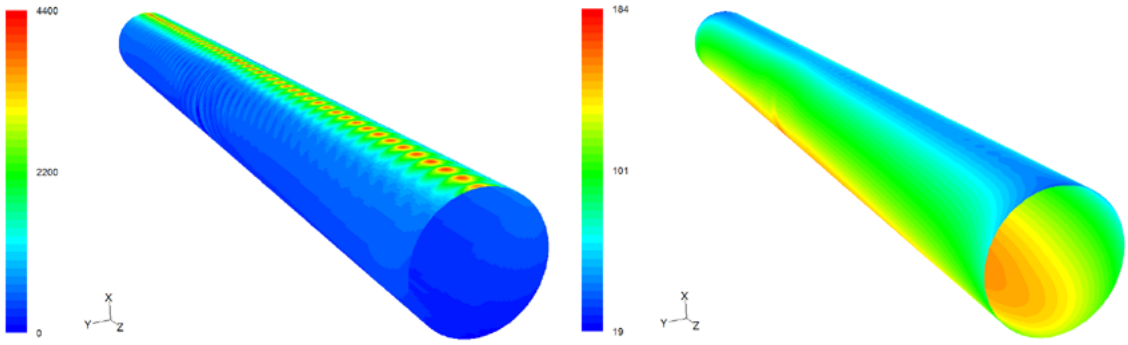

Figure 3.18: Contours of wall heat transfer coefficient ($W/m^2 \cdot K$) on the cooled surface of the heated tube [left] and contours of wall temperature (°C) [right] (double inlet, $Re = 19,000$).

3.3.2 Comparison of Experimental and Numerical Results (Slit)

In this Section, comparison is made between the experimental data and predictions of the *FLUENT*® model described above. Figure 3.19 shows the experimental and numerical azimuthal temperature profiles for the outer tube surface at two axial locations for the double inlet flow configuration at $Re = 11,000$ (Exp. #*TS2*). These results pertain to axial locations #2 (▲) and #8 (●), which are symmetrically located along the inner tube slit length (Figure 3.4). The solid and dashed lines denote *FLUENT*® results obtained using *standard* and *RNG* k-ϵ models, respectively.

The error bars in the angular position represent positioning errors (cf. Section 3.1.1), while those in the temperature T represent the standard deviation in the estimated measurement errors averaged over the two symmetric azimuthal locations with respect to the slit (e.g., $\theta = 20°$ and $340°$). An error analysis of the experimental data is given in Appendix A.

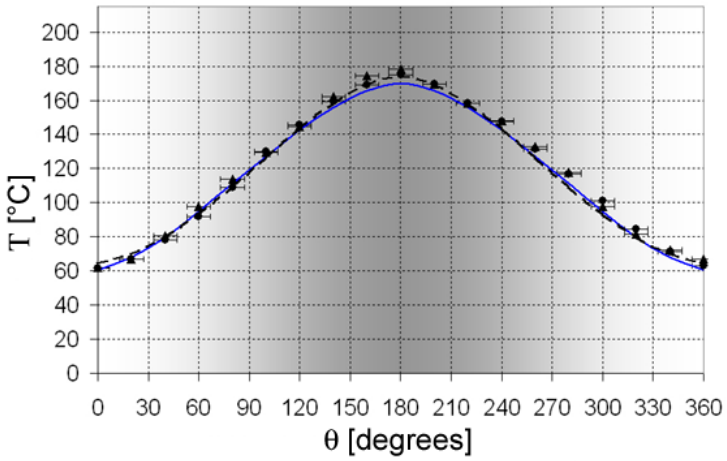

Figure 3.19: Experimental (●) and numerical (solid and dashed lines using *standard* and *RNG* k-ϵ models, respectively) results for $T(\theta)$ at TC locations #2 and #8 (double inlet, $Re = 11{,}000$).

The agreement between the experimental profiles for the two axial TC locations suggests that, as expected, the flow in the test section is symmetric about the slit midpoint, i.e., the stagnation plane at $z = 75$ mm (axial location #5 in Figure 3.4). The maximum temperature occurs at the stagnation point away from the slit ($\theta = 180°$) where the two opposed channel flows in the gap between inner an outer tubes meet. As can be seen in Figure 3.19, the *FLUENT*® results are essentially identical for the two different turbulence modeling options; therefore, only the results obtained using the standard k-ϵ model will be shown.

Figure 3.19 shows good agreement between the measured and predicted temperatures of the outer tube (i.e., heated surface). One would, therefore, expect the azimuthal variations of the local heat transfer coefficient (HTC) at these two axial locations to be also in agreement. It should be noted, however, that even though the outer tube wall is uniformly heated both axially and azimuthally by the applied DC current, the heat flux at the inner surface may not be uniform because of axial and azimuthal conduction through the tube wall. Hence, since the local heat flux cannot be easily measured experimentally, the calculated values of the local heat flux

($\dot{q}''_{CFD}$) are used in conjunction with the measured wall temperatures to determine the experimental heat transfer coefficients:

$$h_{exp} = \frac{\dot{q}''_{CFD}}{T_w - T_{in}} \tag{3.5}$$

Here T_w is the measured local wall temperature and T_{in} is the coolant inlet temperature. Figure 3.20 shows good agreement between the experimental and predicted values of the local heat transfer coefficients.

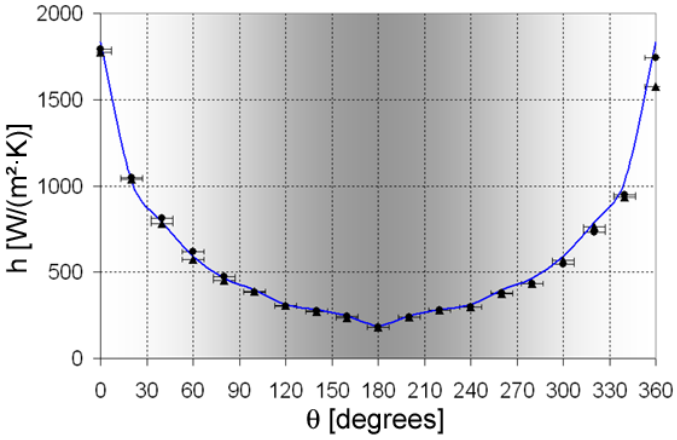

Figure 3.20: Experimental (●) and numerical (line) results for $h(\theta)$ at TC locations #2 and #8 (double inlet, $Re = 11,000$).

These results show that the peak values of the local HTC occur at the stagnation point ($\theta = 0°$ and $360°$) where the rectangular jet issuing from the inner tube slit impacts the inner surface of the outer tube (Figure 3.4b). The values of the HTC quickly drop as the distance from the stagnation point increases.

Figure 3.21 shows axial variations (z-profiles) of the experimental and predicted values of the local heat transfer coefficient for the same experiment described above (double inlet flow configuration at $Re = 11,000$). Values of the HTCs at all nine instrumented axial locations (Figure 3.4a) are shown for $\theta = 0°$ (■), $20°$ (◆), $60°$ (▲), $120°$ (●) and $180°$ (■). The lines denote the values predicted by the *FLUENT*® model (interpolation between the nine axial locations), while the symbols denote the experimental values.

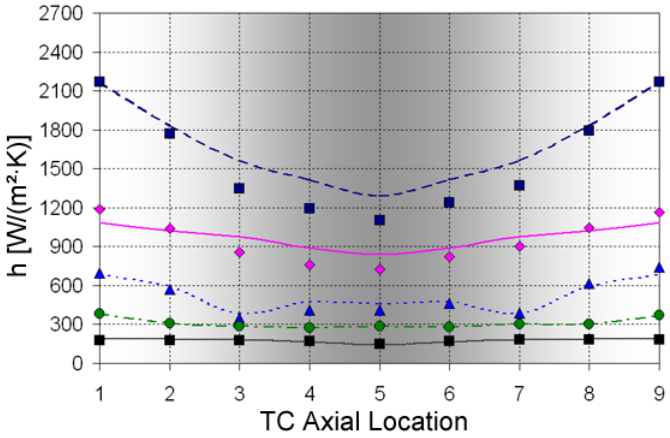

Figure 3.21: Axial distribution of the heat transfer coefficient at instrumented TC locations for $\theta = 0°$ (■), $20°$ (◆), $60°$ (▲), $120°$ (●) and $180°$ (■) (double inlet, $Re = 11,000$).

As expected for this opposing double inlet flow configuration, the HTC reaches a minimum near the midway plane along the inner tube slit (TC location #5). For a given axial location, the HTC decreases as the two channel flows proceed azimuthally away from the stagnation point where the jet issuing from the inner tube slit impacts the inner surface of the outer tube ($\theta = 0°$). For θ values greater than about $20°$, the HTC is essentially independent of axial location.

Results similar to those shown in Figures 3.19–3.21 for the parallel flow arrangement (Figure 3.9) at $Re = 11,000$ are shown in Figures 3.22 and 3.23, respectively. Again, these results show good agreement between the experimental data and model predictions.

Small differences in the measured temperature near the stagnation point ($\theta = 0°$ and $\theta = 360°$ in Figure 3.22, left) result in larger differences in the corresponding HTC. The discrepancy between measured temperatures at $\theta = 0°$ and $\theta = 360°$ is due to changes in the BCs, because of the time span between the two measurement (up to 3–4 h as mentioned earlier). Nevertheless, the associated fractional uncertainty in $h(\theta)$ (Figure 3.22, right) given by the error bars is generally less than 10 %. Although the azimuthal profiles for the local HTC show the same trend observed for the double

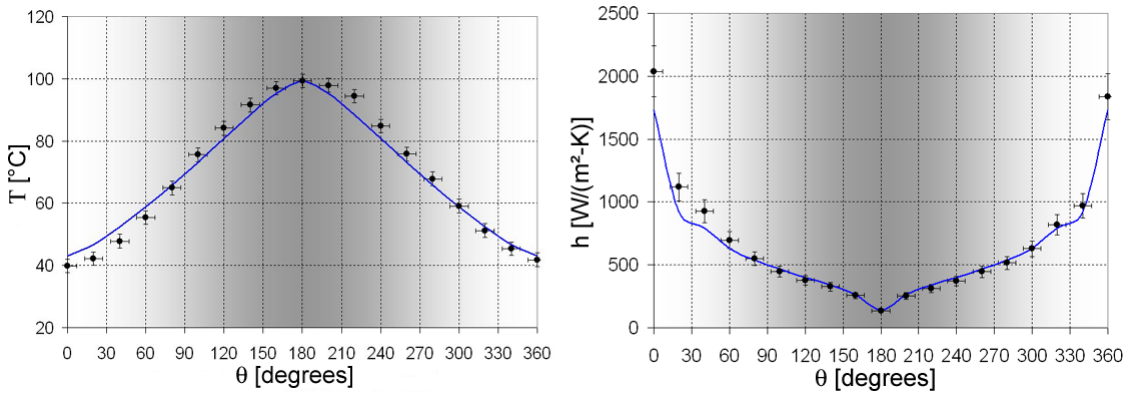

Figure 3.22: Experimental (●) and numerical (line) results for $T(\theta)$ [left] and $h(\theta)$ [right] at TC location #3 (parallel flow, $Re = 11,000$).

inlet flow configuration (i.e., the HTC quickly drops while moving away from the stagnation point), the axial distribution of the local HTC is quite different. While the magnitude for the values of the HTC are similar (because of the equivalent Re), the profile is now asymmetric (Figure 3.23). The flow tends to stagnate near the test module inlet, affecting the flow distribution (Figure 3.17); here the minimum cooling effect is experienced. On the other hand, the maximum cooling effect is experienced near the outlet, where the coolant is free to escape and expand. Here, the coolant velocity is maximum, and so is the local HTC (Figure 3.23). The slight fluctuations in the values of the heat transfer coefficient at axial locations #3 and #7 are likely due to the presence of the bridges spanning the slit.

When considering the counter flow configuration (Figure 3.9), the azimuthal profiles for the local HTC show the same trend already observed (Figures 3.19 and 3.22). Nevertheless, the axial distribution of the local heat transfer coefficient has changed (Figure 3.24). Once again the maximum cooling effect is experienced near the outlet, while the minimum cooling effect is experienced where the flow tends to stagnate (dead-end, Figure 3.17).

The axial variations in HTC shown in Figures 3.21, 3.23 and 3.24 can assist the designer in selecting an optimal module length (and flow configuration) to avoid

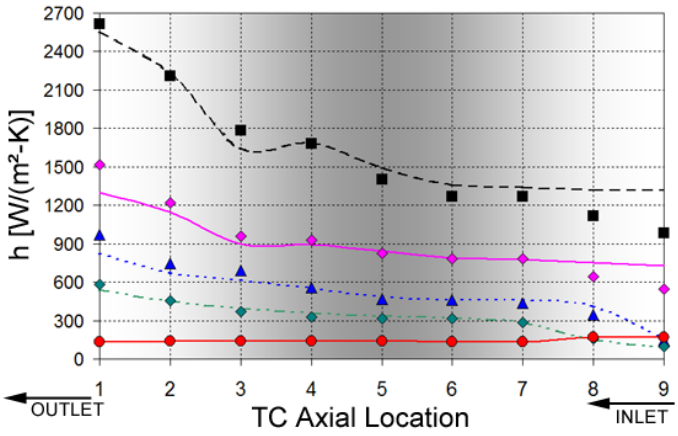

Figure 3.23: Axial distribution of the heat transfer coefficient at instrumented TC locations for $\theta = 0°$ (■), 20° (◆), 60° (▲), 120° (◆) and 180° (●) (parallel flow, $Re = 11,000$).

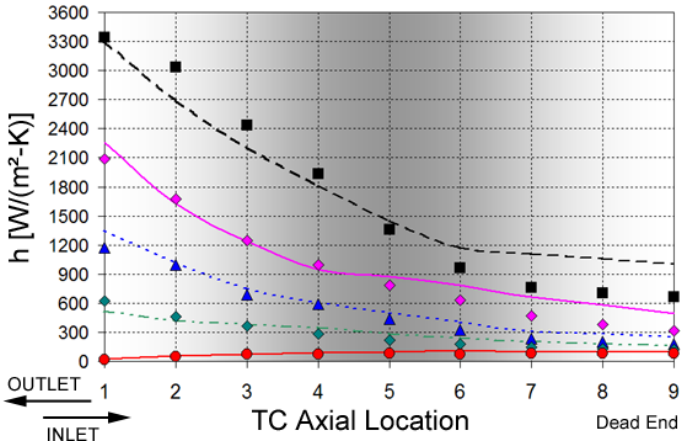

Figure 3.24: Axial distribution of the heat transfer coefficient at instrumented TC locations for $\theta = 0°$ (■), 20° (◆), 60° (▲), 120° (◆) and 180° (●) (counter flow, $Re = 11,000$).

significant degradation in the axial distribution of the local heat transfer coefficient. Degradation of the HTC along the axial extent of the test module (and T-tube module) is undesirable, since it results in large temperature gradients and therefore deformation of the module due to thermal stresses. Table 3.7 summarizes the axial cooling performance of the three flow configurations. The values shown in this Table can be easily obtained from the axial plots of HTC shown before. The axial change in HTC $\Delta h = 80.2\%$ is the greatest for the counter flow configuration. In other words, the

counter flow arrangement presents the worst cooling performance with respect to the other configurations. The superior performance of the double inlet configuration is to be expected since it effectively is only half as long as the other two flow configurations.

Table 3.7: Analysis of the axial thermal performance of the three flow configurations (experimental values, $Re = 11,000$).

Configuration	h_{max} [W/m^2·K]	**axial** Δh [W/m^2·K (%)]	**Performance**
Double Inlet	2,168	1,066 (49.2)	Best
Parallel Flow	2,613	1,630 (62.4)	Intermediate
Counter Flow	3,345	2,683 (80.2)	Worst

The deduction drawn above is also confirmed by the experimental data shown in Table 3.2. For a given Reynolds number, the total power input $\dot{Q}$ necessary to operate the test section under the limits described in Section 3.1.5 is the smallest for the counter flow configuration (compare experiment #*TS*4 vs. #*TS*1 and #*TS*6, and experiment #*TS*5 vs. #*TS*2 and #*TS*7).

In addition to comparing the results for temperature and heat transfer coefficient, one can also investigate on the pressure drop prediction. Unfortunately it is not possible to directly compare the experimental results with those for the actual T-tube design, because of the differences in slot length and flow set-up. Nevertheless, it is possible to compare experimental and numerical results for the test module described in this chapter. Table 3.8 compares the pressure drop in the experimental test section and the numerical model for all the test cases.

The *FLUENT*® prediction seems to be in reasonable agreement with the data for the lower Reynolds numbers, i.e., experiments #*TS*1, #*TS*2, #*TS*4, #*TS*6 and #*TS*7. The reason of the large difference between experimental values and numerical predictions in experiments #*TS*3 and #*TS*5 is related to the test module design. Figure 3.2 shows the three Teflon® spacers used to maintain the concentricity along the length of the outer tube. The annular gap area between the inner and outer tube measures

Table 3.8: Comparison of the pressure drop in the test module (ΔP_{exp}) and the numerical prediction (ΔP_{CFD}).

Exp. #	Re [-]	gauge P_{in} [kPa (psi)]	ΔP_{exp} [kPa (psi)]	ΔP_{CFD} [kPa (psi)]
Double Inlet				
$TS1$	2,900	103 (15)	11.9 (1.72)	12.6 (1.83)
$TS2$	11,000	207 (30)	33.6 (4.87)	33.7 (4.88)
$TS3$	20,000	241 (35)	206 (29.9)	141 (20.5)
Counter Flow				
$TS4$	2,900	29.2 (4.23)	29.2 (4.23)	22.0 (3.19)
$TS5$	11,000	241 (35)	210 (30.5)	112 (16.2)
Parallel Flow				
$TS6$	1,800	8.2 (1.19)	8.2 (1.19)	10.9 (1.58)
$TS7$	11,000	281 (40.8)	108 (15.6)	103.8 (15.1)

~ 46.8 mm^2, and 50 % of the area is blocked by the three 60° Teflon® spacers. The rectangular jet area measures 90 mm^2, about twice as much the outlet area for the double inlet arrangement and about four-times the outlet area for the counter and parallel flow arrangements (remember that two sides are engaged for the double inlet configuration, but only one is for counter and parallel flows). This means that the narrowest passage for the coolant is found between the Teflon® sectors rather than through the slot. In experiments #$TS3$ and #$TS5$ the mass flow rate is large enough to cause choking of the flow at the outlet, i.e., the flow becomes *sonic* in the small openings between the spacers[3]. The very large pressure drop (~ 210 kPa) supports this conjecture.

The small sectors are included in the *FLUENT*® model and the solution shows the significant blockage effect due to this details (Figure 3.16 shows the highest flow speed is experienced at the passage between the Teflon® spacers at the outlet). However, choked flow that is experimentally observed cannot be predicted in the numerical

[3]For experiments #$TS3$ and #$TS5$ $\overline{V} = \frac{\dot{m}}{\rho A} \approx 240$ m/s or $M \approx 1$ (the air is discharged at room pressure).

model because the thermodynamic properties are kept constant in the simulations.

It can also be noticed that for a given Reynolds number the smallest pressure drop is experienced by the double inlet arrangement. Counter and parallel flow pressure drops are similar, with a slightly smaller pressure drop for the latter. The better numerical prediction for the double inlet configuration is due to the finer grid resolution. For the double inlet case only a quarter-model model geometry has been necessary, whereas half-model geometry had to be used for the single inlet configurations (Figure 3.10). Therefore, for the same number of grid elements, the grid resolution of the double inlet was doubled with respect to the resolution of the single inlet models.

Finally, one could wonder why for $Re = 11,000$ the flow is choked for the counter flow, but not for the parallel flow cases (compare experiments #*TS*5 and #*TS*7). The flow in experiment #*TS*5 choked because the outlet pressure was considerably lower than that for #*TS*7.

3.3.3 Nusselt Number Calculations

The Nusselt number was calculated based on the slit hydraulic diameter $D_h = 1.2$ mm, and a constant thermal conductivity $k = 0.02521\ W/(m \cdot K)$ — the default value in *FLUENT*® for air (Equation 3.4). Since Nu is proportional to the heat transfer coefficient, its behavior is similar to that of the local HTC.

Figure 3.25 shows the axial plot of the Nusselt number at the stagnation point ($\theta = 0°$) for the double inlet configuration at $Re = 2,900$, $11,000$ and $20,000$). This Figure shows the same trend observed for the local heat transfer coefficient (Figure 3.21). The highest cooling effect, and therefore the highest Nu, is experienced near the outlets — TC locations #1 and #9. The lowest cooling effect (hence lowest Nu) is experienced at the center of the test module — TC location #5, where the flow forms a stagnation plane.

Figure 3.26 shows the azimuthal plots of the Nusselt number for TC axial locations

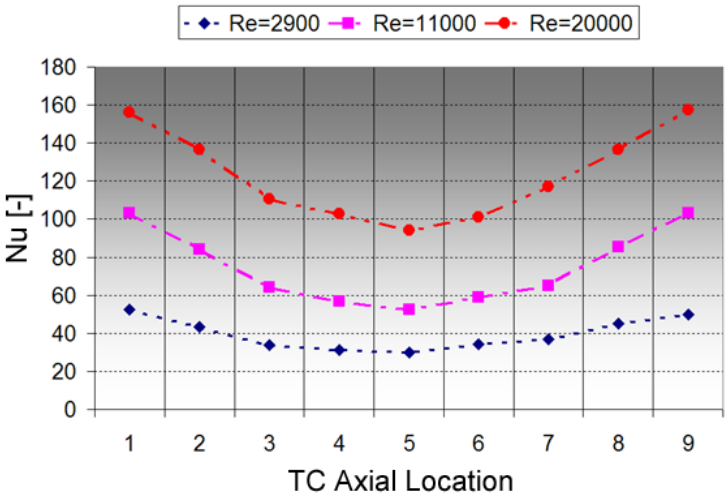

Figure 3.25: Axial plot of the experimental Nusselt number at the stagnation point ($\theta = 0°$) for three different Reynolds numbers (double inlet configuration). The lines only interpolate between the experimental data points.

#1 (left) and #5 (right), representing extreme conditions at the end and the center of the test section, for three different Reynolds numbers (double inlet configuration). The Nusselt number quickly drops while moving away from the stagnation point, $\theta = 0°$, and reaches a minimum at $\theta = 180°$, opposite to the impinging region (compare with Figure 3.20). The results shown in Figure 3.26 are in agreement with those found in the literature (Figure 2.3). The values of Nu are higher because of the smaller jet-to-wall spacing (here $H/B = 1.83$ vs. $Z/B = 4.0$ in Figure 2.3).

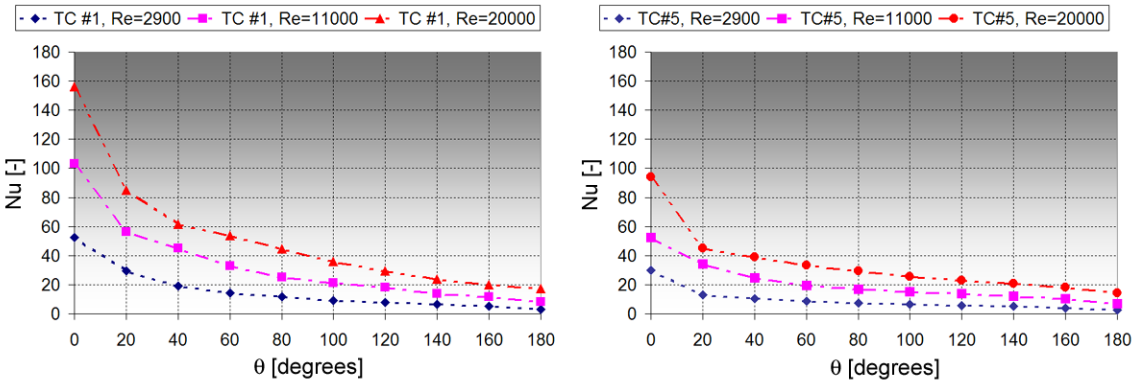

Figure 3.26: Azimuthal plot of the experimental Nusselt number for TC axial locations #1 (left) and #5 (right) for three different Reynolds numbers (double inlet configuration). The lines only interpolate between the experimental data points.

3.3.4 Comparison of Experimental and Numerical Results (Row of Holes)

Experimental and numerical temperature and local heat transfer coefficient profiles were also compared for this test section geometry. Figure 3.27 [left] shows the plot of the azimuthal temperature profiles for the axial TC locations 1–9 (symbols) and the corresponding *FLUENT*® prediction (lines) for the double inlet configuration for $Re = 19,000$ (exp. #*TH*2).

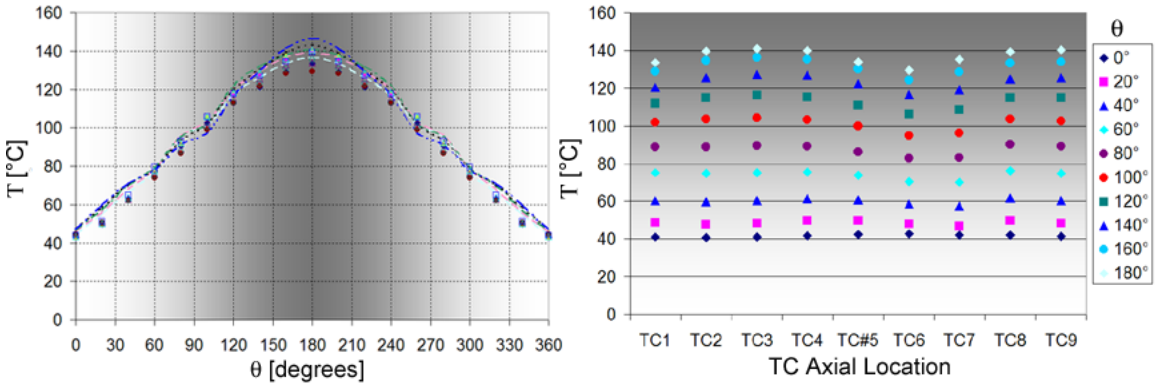

Figure 3.27: Plot of the azimuthal temperature profiles for the nine axial instrumented locations (symbols) and the corresponding numerical prediction (lines) [left] and plot of the axial temperature profiles at different azimuthal locations (symbols) [right] ($Re = 19,000$ — exp. #*TH*2).

These azimuthal profiles present the same trend shown in Figures 3.19 and 3.22. Since a quarter-model has been used for the numerical calculations, only five lines are represented (one through five) because of the symmetry of the flow about its centerline. The computer model prediction seems to be consistent at all the axial locations. The plot shows that the wall temperature is basically *independent* of the axial location, which can also be shown by plotting the axial temperature profiles at different azimuthal locations (Figure 3.27 [right]).

Figure 3.28 shows the azimuthal [left] and axial [right] HTC profiles. The azimuthal profiles are qualitatively very similar to the slot case (Figures 3.20 and 3.22), i.e., the HTC quickly drops as θ increases, reaching a minimum at $\theta = 180°$. The axial profiles show once again that the cooling performance is fairly *uniform* along z.

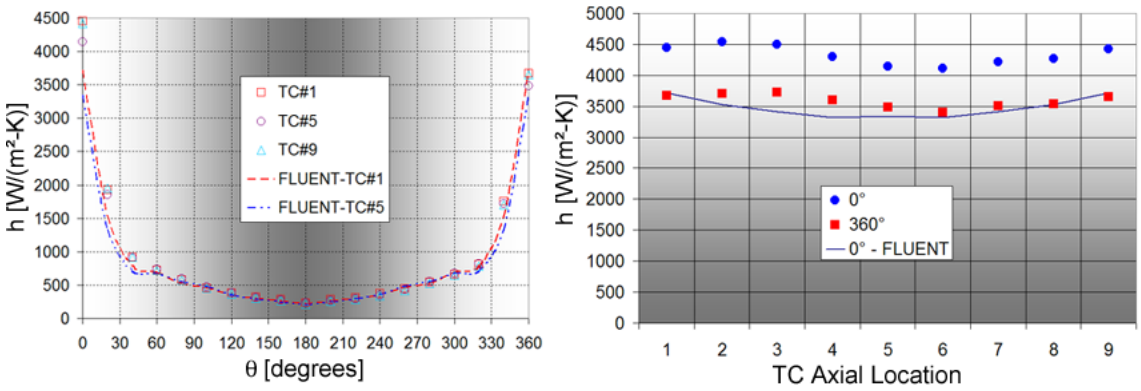

Figure 3.28: Azimuthal HTC profiles for the axial instrumented locations #1, #5 and #9 (symbols) and the corresponding numerical prediction (lines) [left]; axial locations #1 and #9 are symmetric about the centerline. Axial HTC profiles at the stagnation point, i.e., $\theta = 0°$ and $\theta = 360°$ (double inlet flow configuration at $Re = 19,000$ — exp. #*TH*2) [right].

As mentioned earlier, the difference between data values at $\theta = 0°$ and $\theta = 360°$ is related to changes in the experimental BCs during the time span of the test. Because of the jets along z, the local heat transfer coefficient undergoes steep gradients (see Figure 3.18). Therefore, the average numerical surface heat flux along a line at fixed azimuthal positions (e.g., $\theta = 0°,\ 20°, \ldots$) has been used for the calculation of both the numerical and experimental HTCs.

Table 3.9 summarizes the experimental pressure drop ΔP_{exp} and the numerical prediction ΔP_{CFD} for all the experimental cases reported in Table 3.4. The pressure drop prediction is in reasonably good agreement with the experimental data for the double inlet flow configuration.

Table 3.9: Comparison of the pressure drop in the test module (ΔP_{exp}) and the numerical prediction (ΔP_{CFD}) for the T-tube test module where the slit has been replaced by a row of small holes.

Exp. #	*Re* [-]	ΔP_{exp} [kPa (psi)]	ΔP_{CFD} [kPa (psi)]
Double Inlet			
*TH*1	10,000	9.3 (1.3)	9.85 (1.42)
*TH*2	19,000	36.7 (5.3)	36.3 (5.26)
*TH*3	27,000	75.2 (11.1)	78.5 (11.4)

3.3.5 Comparison of Slot and Holes Design Concepts

It has been briefly discussed how the cooling performance of this T-tube module with a line array of round jets differs from the performance of the rectangular (slot) jet — Section 3.3.1. The change in jet geometry did not seem to affect the azimuthal profiles of temperature and heat transfer coefficient (Figure 3.27 [left] and 3.28 [left]). However, a significant improvement in the performance along the axial direction was noticed. Figure 3.29 compares the axial Nu profiles for the array of round jets and the rectangular (slot) jet. The Nu for the round jets was calculated using the diameter of the holes $D = 1.0$ mm. The axial degradation of the heat transfer performance is negligible in the case of the round jets. This would eliminate axial temperature gradients, with benefits for the structural integrity of the T-tube module.

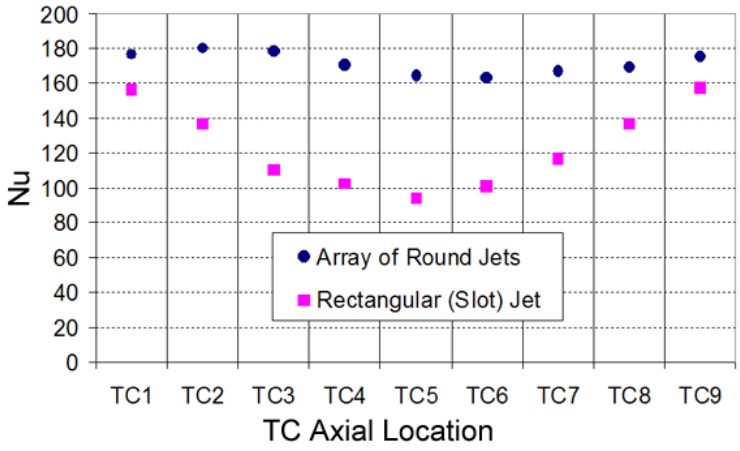

Figure 3.29: Comparison of Nu profiles at the stagnation point ($\theta = 0°$) for the array of round jets ($Re = 19,000$) and the rectangular (slot) jet ($Re = 20,000$).

Although the test section with the holes has just as good (or perhaps even better, depending upon the application) cooling performance than the test section with the slot, it has to be acknowledged that the total area of the holes ($A_h = 40$ mm^2) and the area of the slot ($A_{slot} = 90$ mm^2) are very different. Some implication can be deduced from Equations 3.1 and 3.3, which can also be re-written as:

$$\dot{m} = \frac{ReA\mu_{in}}{l} \tag{3.6}$$

For a selected cooling performance and type of coolant (i.e., same Re and μ_{in}) and if the characteristic length l is similar — compare $D_h = 1.2$ mm (slot) vs. $D = 1.0$ mm (holes), the required mass flow rate $\dot{m}$ will be inversely proportional to the jet(s) area A. Hence, by using round jets rather than a slot, it could be possible to utilize a smaller mass flow rate of coolant. For the same reason, the pressure drop in the module would be much smaller, because of the smaller mass flow rates involved while maintaining the same Re.

CHAPTER IV

T-TUBE APPARATUS: SINGLE-SIDED HEATING

This chapter describes experimental studies conducted on a test section duplicating the *ARIES* T-tube divertor module. For this test section the heat load is *single-sided* (i.e., incident only on one side of the test module) rather than axisymmetric across the periphery of the pressure boundary, therefore duplicating the actual configuration of the T-tube divertor. First, the experimental apparatus and procedures used in this investigation are described. Second, the numerical model is presented. Finally, the results of the investigations are shown and discussed. Comparison is made with the results obtained with the axisymmetrically heated test section shown in the previous chapter.

4.1 Experimental Apparatus and Procedures

4.1.1 Experimental Test Section

A schematic of the single-sided heated T-tube test apparatus is shown in Figure 4.1. The test section can be divided into two parts:

1. A concentric cartridge, which includes the *T-block*, inner *slotted tube*, and two *end caps*. This cartridge closely duplicates the proposed *ARIES* T-tube (Section 2.2.1). The brass T-block duplicates the tungsten armor and the pressure boundary of the proposed T-tube.

2. A heater, which consists of a tapered copper block (*concentrator*), housing three *cartridge heaters*. The concentrator provides the incident heat flux only onto one side of the brass cartridge, therefore duplicating the heating configuration typical of real divertors.

As shown in the cross-section of Figure 4.1 [left], the coolant (air) enters the concentric cartridge through an inlet port located mid-way along its length (light blue arrow). The air enters the slotted tube and is then accelerated through the slot because of the large reduction of the cross sectional area (Figure 4.1 [right]). After impinging upon the inner surface of the T-block, the air flows as a curved turbulent channel flow along the gap between the slotted tube and the inner surface of the T-block and is then removed through the two exit ports (Figure 4.1, red [dark] arrows).

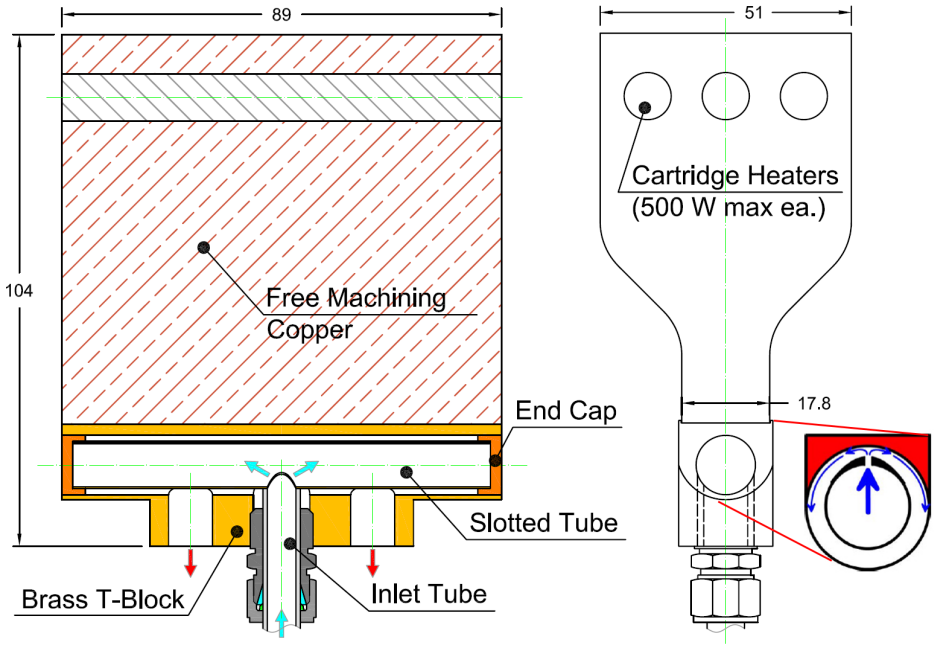

Figure 4.1: Cross-section (left) and side view (right) of the single-sided heated T-tube experimental apparatus. Shown dimensions are in mm.

The T-shaped cartridge block is made of C36000 free machining brass. As shown in Figure 4.2, this component is 89 mm long and 19 mm wide, vs. the 85 mm length and 19 mm width of the *ARIES* T-tube (Section 2.2.1). A circular cavity 12 mm in diameter, corresponding to the pressure boundary, is bored through the entire length of the block . The "top" flat portion of the T is subject to the incident heat flux (provided through the copper block); the "bottom" portion houses the coolant (air) fittings. One 1/4" NPT port is cut at the center location and is used as coolant *inlet*;

two 1/8" NPT *outlet* ports are symmetrically cut on both sides of the inlet port.

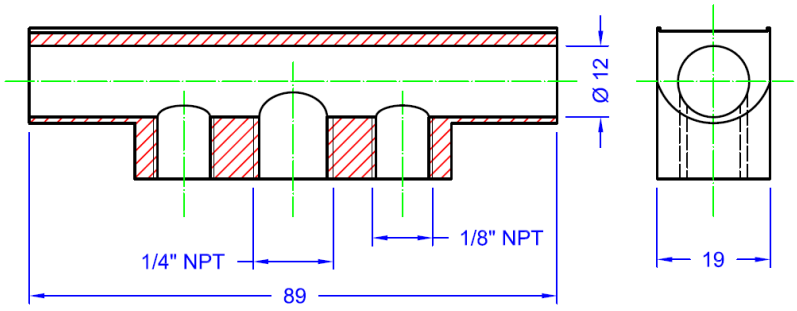

Figure 4.2: Cross-sectional view of the T-shaped brass block.

The T-block houses a 82.5 mm long brass inner tube which is placed inside the 12 mm cylindrical cavity. The inner tube OD is 9.5 mm (3/8") and it is selected so that the annular gap between the tube and the pressure boundary is 1.25 mm, which matches the gap thickness for the proposed T-tube divertor (Section 2.2.1.1). Two brass end caps are press-fit to the ends of the tube to ensure that the inner tube remains concentric within the cavity and secured to the T-block. A 71 mm long, 0.46 mm wide (0.018") slot is cut along the length of the inner tube (Figure 4.3).

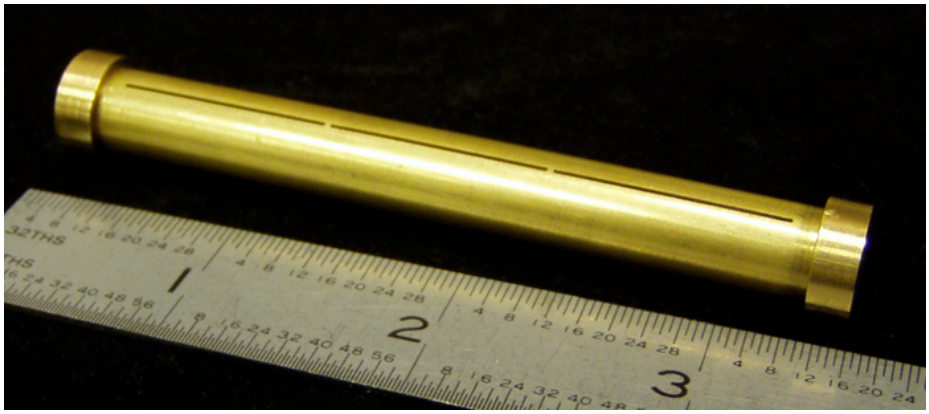

Figure 4.3: Photograph of the slotted inner tube and end caps.

Two 0.8 mm-wide bridges are left uncut at one-third and two-thirds of the slot length in order to prevent slot deformation due to residual stresses and maintain the uniformity of its width along the entire length. A 7.2 mm diameter hole is cut at the

center of the slotted tube on the opposite side of the slot. The air enters the inner tube through this inlet port.

The test module is assembled as follows:

1. The slotted tube with the end caps is inserted and axially centered in the T-block.

2. The slot is aligned to face towards the top flat portion of the outer block, i.e., facing the incident flux.

3. The end caps are then silver brazed to the T-block.

Figure 4.4 shows the inspection of the assembly from the bottom side. The coolant inlet hole in the inner tube is aligned with the threaded inlet port and the slot is facing towards the top of the T-block.

Figure 4.4: This view of the T-block/slotted tube assembly from the bottom side shows the inner tube coolant inlet hole aligned with the inlet port and the slot facing towards the top of the T-block.

A 3/8" diameter copper tube is secured to the slotted tube with epoxy cement, forming a T-junction as shown in Figure 4.5. Precise centering of the tubing is guaranteed by the use of a bored-through Swagelok® placed in the 1/4" NPT inlet port of the T-block. Proper mating of the surfaces is guaranteed by cutting a 3/8" diameter arch at one end of the copper tube. The copper tube is connected to the flow loop (Section 4.1.2); a pressure transducer (*OMEGA*® PX180-060DV) and a

thermocouple probe (E-type, *OMEGA*® EMQSS-125G-6) monitor coolant pressure and temperature at the inlet.

Figure 4.5: Sample of the T-union between the brass inner tube and the copper inlet tube.

The C14500 copper alloy block (the concentrator) is secured to the top side of the T-block by two stainless steel clamps. The copper block houses three 500 W cartridge heaters (*FAST – HEAT*® CH44126 120 V HB) which provide the thermal power (Figure 4.6). The concentrator is tapered in order to *focus* the heat load into a much smaller area, therefore increasing the incident heat flux on the connected brass T-block. An aluminum foil shim is placed between the copper heater and the brass block to ensure good thermal contact between the mating surfaces.

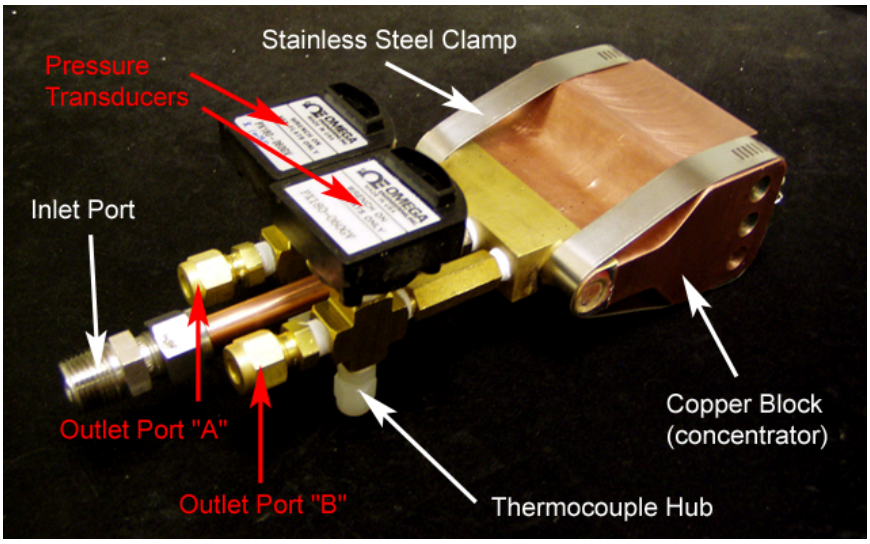

Figure 4.6: Complete assembly of the test section. The crosses at the outlet ports provide the instrumentation for coolant pressure and temperature measurements. The copper block will house three cartridge heaters which will provide the heat load.

Two 1/8" NPT brass crosses are connected to the outlet ports of the T-block. Each cross supports a pressure transducer (*OMEGA*® PX180-060DV) and a thermocouple probe (E-type, *OMEGA*® EMQSS-125G-6). The fourth port of each cross is prepared with a Swagelok® fitting, ready to be connected to the flow loop (Figure 4.6).

Fifteen E-type thermocouple probes (*OMEGA*® EMQSS-020G-6) are embedded in the T-block to measure axial and azimuthal wall temperature profiles. These probes are placed on planes at three different axial locations, specifically at 1/4, 1/2 and 3/4 of the axial extent of the T-block. At each plane, five probes are distributed around the periphery of the pressure boundary and they are equally spaced by 30° (Figure 4.7). The thermocouple beads are placed at $\theta = 0°$ (the impinging jet stagnation point) and $|\theta| = 30°$, 60°, 90° and 120° away from the stagnation point. The TC beads have a 0.5 mm radial offset (edge-to-edge) from the pressure boundary surface.

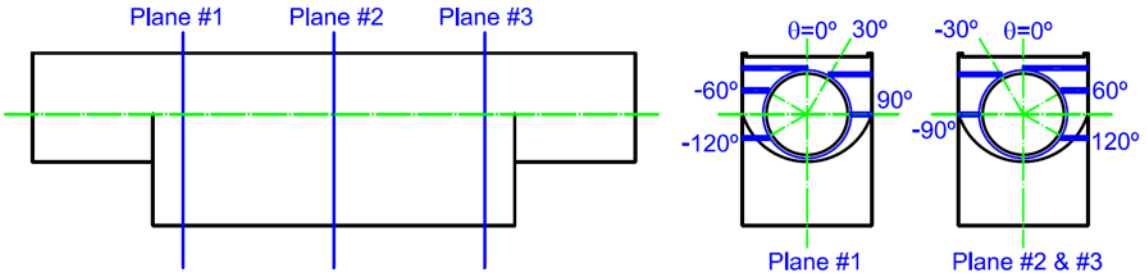

Figure 4.7: Schematics of the TCs bead location in the T-block.

Planes #2 and #3 are identical, but their axial position is different; hence, it is possible to monitor *axial* temperature gradients. With similar reasoning, planes #1 and #3 are symmetric with respect to the center, but the TCs azimuthal position is mirrored; therefore it is possible to verify the *azimuthal symmetry* of the test module.

Six E-type thermocouple probes (*OMEGA*® EMQSS-032G-6) are embedded in the "neck" of the concentrator to measure the incident heat flux. The TCs are located on two planes ("A" and "B") at one-third and two-thirds of the copper block length. The TCs distances from the contact surface with the T-block are (3.0, 7.0, 12.0) mm as shown in Figure 4.8. The probes are embedded half-way in the material.

Two additional TCs (E-type, *OMEGA*® EMQSS-062U-6) are located between the cartridge heaters in order to monitor the maximum temperature of the copper block. The completed test module is then insulated with 2"-thick panels of mineral wool.

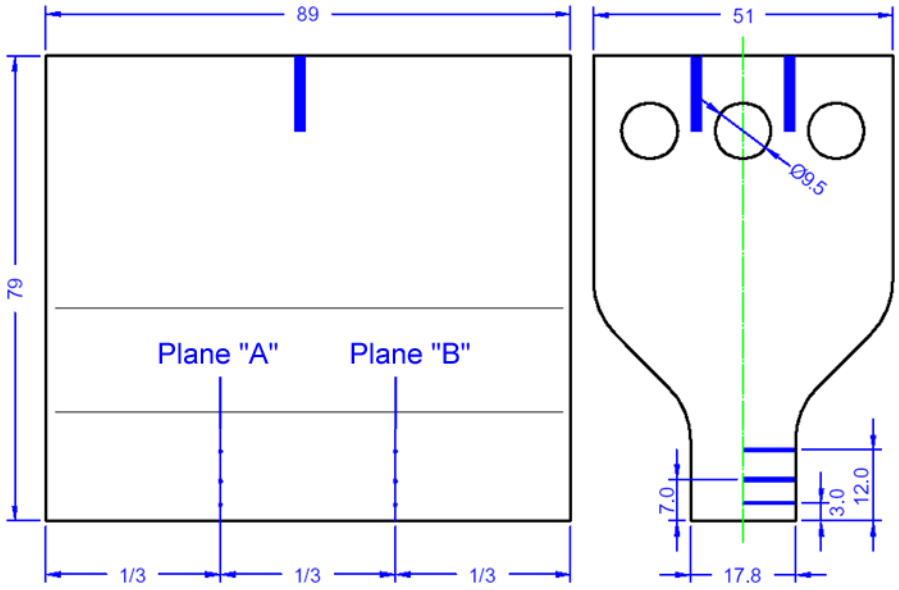

Figure 4.8: Schematic of the TCs positioning in the heater block. Six TCs are located in the thinner region to measure the incident heat flux and two TCs between the cartridge heaters are used to monitor the maximum temperature in the copper.

4.1.2 Experimental Flow Loop

Figure 4.9 shows the diagram of the flow loop. Air from a compressed-air line at a controlled gauge pressure up to ~690 kPa (100 psi) enters the flow loop and is discharged to the surroundings after flowing through the test module. Pressure and mass flow rate in the test section are controlled by a needle valve located at the exit of the test module. The outlet ports of the test module are joined before the needle valve with 1/4" OD brass tubing (Figure 4.10).

The thermal power input (i.e., the heat flux incident on the T-block) is provided by the three 500 W cartridge heaters described before. The heaters are connected in parallel and are powered by controlling their voltage with a variable autotransformer

(Staco Energy Products 3PN1010V). The voltage is measured with a digital multimeter (Hewlett Packard 34401 A) and the current is measured with an additional multimeter (Fluke 25) or a AC ammeter (Shurile Model 8508).

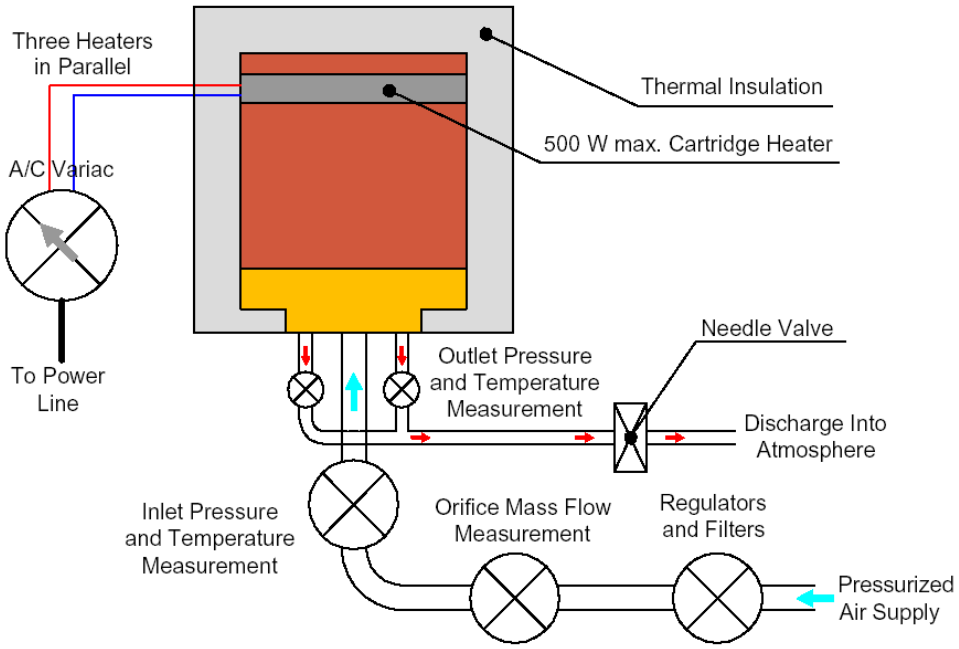

Figure 4.9: Schematic of the flow loop.

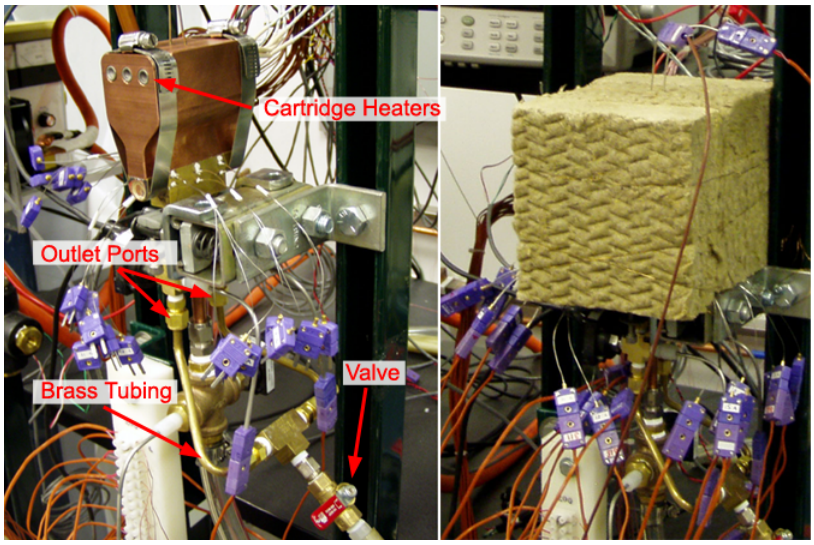

Figure 4.10: Photograph of the experimental test section without [left] and with [right] the thermal insulation. The symmetric outlet ports are joined with custom-made brass tubing before the discharge valve [left].

4.1.3 Experimental Parameters and Procedures

Table 4.1 lists the experiments conducted on the prototypical T-tube test module in order of increasing *Re* and power input. The Reynolds number varies between $4.8{\times}10^3$ and 30.4×10^3, vs. a nominal design value of 1.9×10^4 for the helium cooled divertor at its nominal operating conditions (Table 3.1). The Reynolds number is based on the *hydraulic diameter of the impinging rectangular jet* (Equation 3.1). The *nominal* incident heat flux $\dot{q}''_{nom}$ is calculated using the total power input to the cartridge heaters and the area of the concentrator "neck" ($A_{neck} = 1.58 \times 10^{-3}$ m^2). The *net* heat flux $\dot{q}''_{net}$ is calculated using the temperature measurements in the concentrator neck (Figure 4.8). For safety reasons, the power input was selected so that the temperature in the hotter portion of the concentrator, i.e., between the cartridge heaters, remained less than 500 °C (half the melting point of C14500 copper alloy).

Table 4.1: List of experiments for the T-Tube test module with single-sided heat load. All experiments were performed at a gauge pressure P =414 kPa (60 psi).

Exp. #	$\dot{m}$ ($\dot{m}_\ell$) [g/s] ([g/(s·m)])	*Re* [-]	ΔP [kPa (psi)]	$\dot{Q}$ [W]	$\dot{q}''_{nom}$ [MW/m^2]	$\dot{q}''_{net}$ [MW/m^2]
*TT*1	3.1 (43.7)	4,800	6.9 (1.00)	192	0.12	0.10
*TT*2	7.8 (110)	11,800	21.5 (3.12)	505	0.32	0.28
*TT*3	12.5 (176)	19,000	46.5 (6.74)	890	0.56	0.55
*TT*4	12.5 (176)	19,000	52.9 (7.67)	1035	0.65	0.61
*TT*5	20.0 (282)	30,400	141.7 (20.6)	1320	0.84	0.75
*TT*6	20.0 (282)	30,400	139.5 (20.2)	1350	0.85	0.81

Each experiment is performed as follows:

1. The power supply is slowly increased to the desired input value in order to warm up the test section (the copper block has a large thermal inertia). The test input power is based on the limitations described above, while trying to maintain the temperature range as high as possible, in order to limit experimental error in the temperature measurement.

2. With the flow loop closed, the test section is pressurized to a value close to that of the operating pressure with the pressure regulator at the inlet.

3. The desired mass flow rate is set with the needle valve at the exit.

4. The test section inlet pressure is then set to the desired value by adjusting the inlet pressure regulator (note that the pressure will change after step #3 because the flow will introduce a pressure drop).

5. Once the temperatures in the test section reach steady state, the data are collected.[1]

The test module required about 45-60 min to warm up, depending on the target heat flux/mass flow rate. An additional 30-45 min interval was required to reach steady-state temperatures. A complete experiment typically took 2 h.

4.2 Numerical Modeling

Numerical models were developed with the same CFD package used for the previous investigations (*FLUENT*® and *Gambit* 2.2.30). *A priori* calculations have been used to assist the design of the test module and the selection of the experimental parameters (Section 4.3.1). *A posteriori* calculations were used to compare the numerical prediction to the experimental data, with the intention to validate the numerical model (Section 4.3.2).

4.2.1 Model Geometry

The model wireframe structure was partly developed in *AutoCAD*® 2006 and partly constructed in *Gambit*® 2.2.30. The model includes the T-block, the slotted inner tube (with the slot bridges and the end caps), the copper inlet tube, the copper

[1]The temperatures were assumed to have reached "steady-state" when the thermocouple probe readings sampled at 0.2 Hz remained constant within ±0.5 °C for 10–15 data scans.

concentrator, the cartridge heaters, the thermal insulation and part of the inlet and outlet fittings. Because of geometric symmetry, a quarter-model has been used for all the simulations (Figure 4.11).

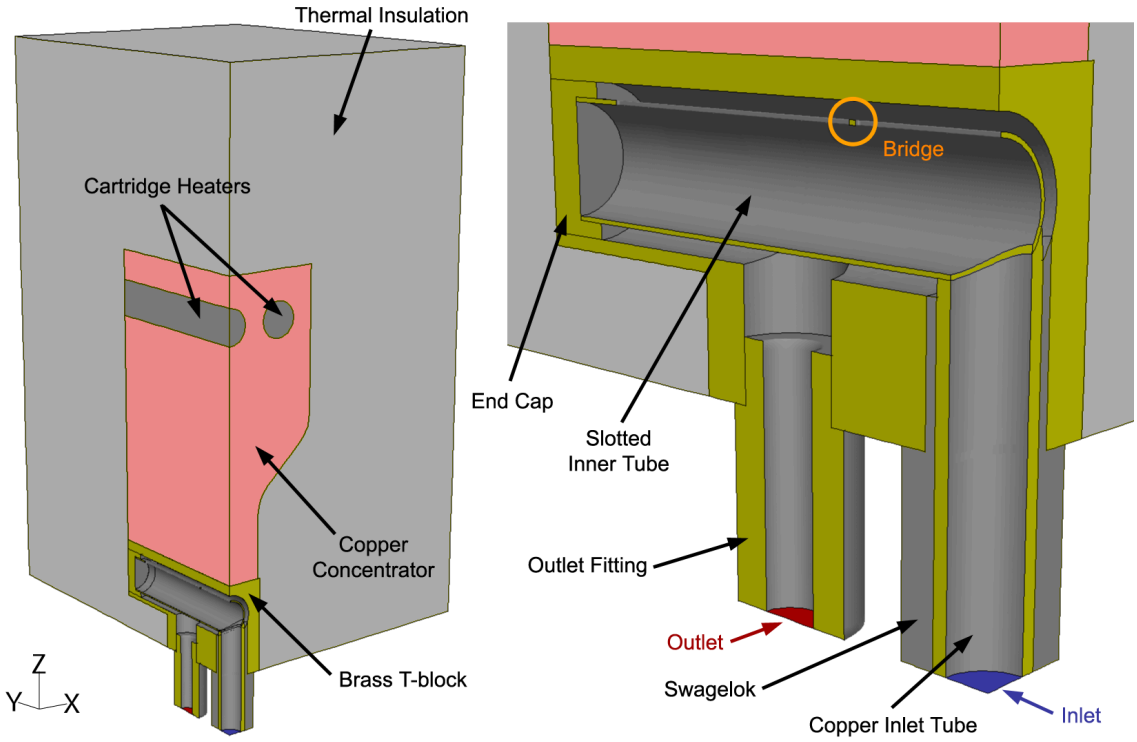

Figure 4.11: Quarter-model geometry used for the numerical calculations. The model includes all the components of the actual test module, including details such as the slot bridge.

4.2.2 Grid Generation

The model grid was built using *Gambit* 2.2.30. The grid consists of 1.4×10^6 cells (765,000 nodes). As in the case described in Section 3.2.2, the multi block technique has been used in order to optimize the topology and quality of the grid.

Figure 4.12 shows the model surface mesh. The grid is obviously much finer in the region of impingement/convective heat transfer [left]. A magnified view of this region [right] shows how the majority of the elements are brick-shaped rather than tetragonal, e.g., it was possible to create quadrilateral mesh faces in the annular gap and then sweep this face mesh along the axis of the model. Building such a grid

required more effort with respect to a non-structured tetragonal grid, but it allowed control of the node-to-wall distance in the gap between the inner tube and the pressure boundary. The criteria for the convergence of the numerical solution are the same as those described in Section 3.2.4; for this case, however, grid convergence studies were not performed.

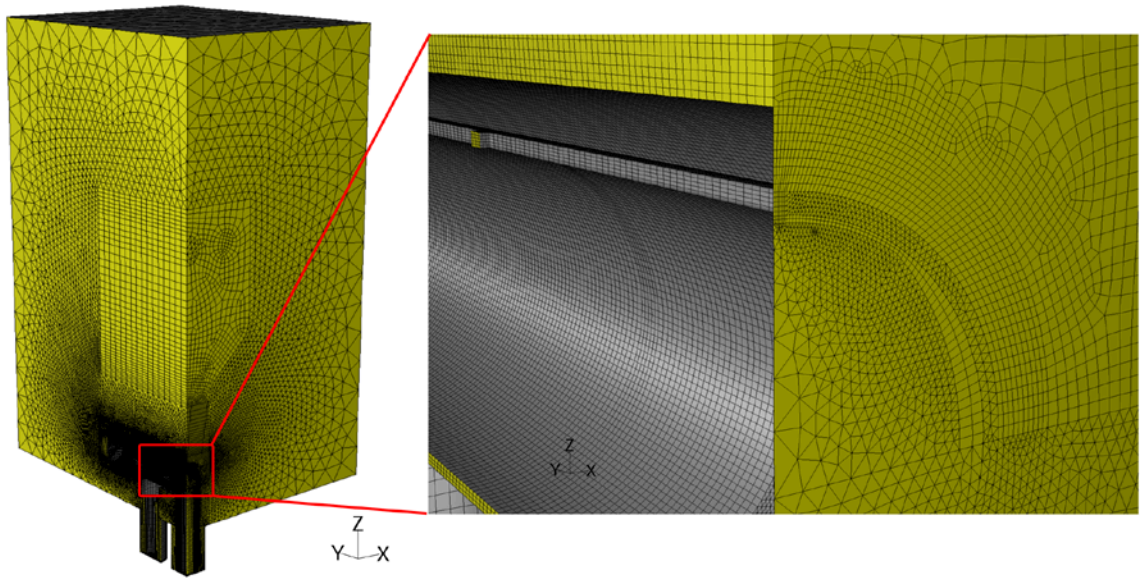

Figure 4.12: Grid of the quarter-model geometry used for the numerical calculations. The majority of the grid consists of *brick* (rather than tetragonal) elements.

4.2.3 Boundary Conditions

The boundary conditions used in the simulations are defined in *FLUENT*® and they specify:

- $\dot{Q}_v'''$: The power input to the heaters, i.e., uniform heat generation rate per unit volume [W/m^3]
- $\dot{m}_{in}$: Coolant mass flow rate at the inlet [kg/s]
- T_{in}: Coolant temperature at the inlet [°C]
- P_{out}: Gauge exit pressure [Pa]

- P_{oper}: Operating pressure [Pa]
- h_{amb}: Heat transfer coefficient between the test module and the ambient, i.e., outer insulation surface [W/(m^2·K)]

Empirical values for h_{amb} are based on the results obtained in the case of the axisymmetrically heated model (Section 3.2.3). All other parameters correspond to their respective measured values for each experiment to be analyzed. Table 4.2 shows the material property values used in the numerical simulations. Coolant (air) properties are identical to those reported in Section 3.2.3.

Table 4.2: Properties of the materials used in the numerical calculations.

Material	ρ	k	c
	[kg/m^3]	[W/m·K]	[J/kg·K]
316 SS	8027	16.26	502
Brass (C36000)	8800	116	380
Copper (C14500)	8940	354.8	376.8
Magnesium Oxide (Heaters)	3580	T [K] — k	877
		273 — 42	
		400 — 29	
		600 — 20	
		800 — 14	
		1000 — 11	
Mineral Wool (Insulation)	130	see Figure 4.13	840

As discussed in Section 3.2.3, the estimation of the heat loss required particular attention; the insulation outer surface temperature has been monitored with a IR thermometer (Raytek Raynger MX2) and then compared to the model prediction, in order to validate the boundary conditions. To improve the temperature prediction of the model, a *temperature-dependent* thermal conductivity k was used for the insulation (Figure 4.13) and the cartridge heaters (Table 4.2).

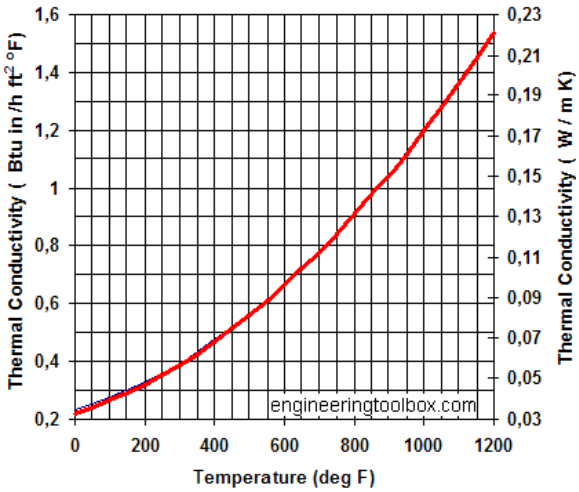

Figure 4.13: Temperature dependence curve for the thermal conductivity k of mineral wool (`http://www.engineeringtoolbox.com`).

4.3 Results and Discussion

4.3.1 Nominal Test Case Results

For the T-tube prototypical test module with single-sided heating, the tests where the conditions are the closest to the actual T-tube module operating conditions (i.e., *nominal test case*) are experiments #*TT*3 and #*TT*4 ($Re = 19,000$). In this section the numerical results of the nominal test case will be shown and general thermal-hydraulic behavior will be deduced.

Figure 4.14 shows the temperature profiles on the cooled surface of the T-block, i.e., the pressure boundary. The top portion (red) is the the region of jet impingement; it is also the side subject to the incident heat flux. Because of this, in contrast to the uniform azimuthal heating case (Figure 3.14), the temperatures are the highest in this area. While moving away from the heated side, the temperatures progressively decrease and reach a minimum in the opposite region (green-blue), where the coolant inlet and outlet ports are located.

The *axial* contours of temperature are fairly uniform. The middle section seems to be slightly cooler and the hottest spots are located at the ends of the module,

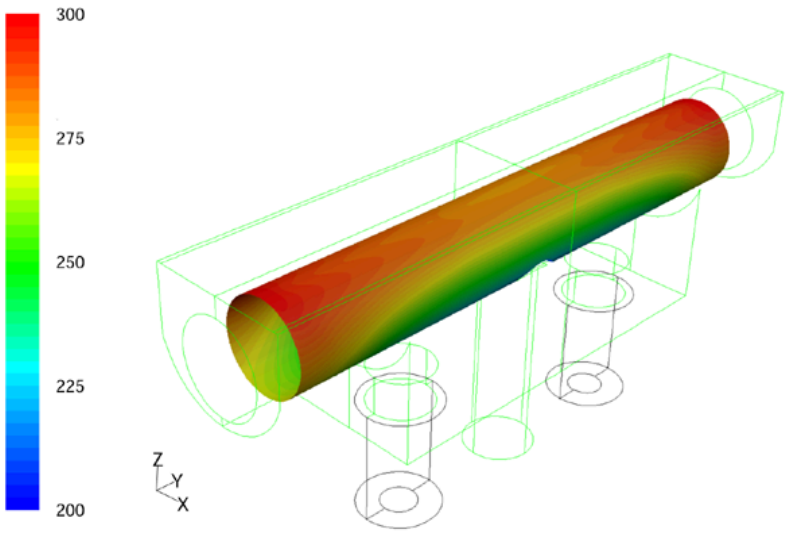

Figure 4.14: Contours of wall temperature (°C) on the cooled surface of the brass T-block ($Re = 19,000$).

because of the end caps and the flow distribution.

Figure 4.15 shows the wall heat transfer coefficient profiles on the cooled surface of the T-block for the same case described above. The red stripe at the top represents the region of jet impingement. Here the heat transfer coefficient is maximum, because of the high-velocity coolant exiting through the slit. While moving away from the jet stagnation point, the heat transfer coefficient quickly drops and reaches a minimum at the bottom region of the module (blue).

The contours shown in Figure 4.15 are very similar to the contours of Figure 3.15. These values of the local surface heat transfer coefficient are similar to the results obtained in the uniform heating case because of the equivalent *Re*. For the prototypical test module though, the *axial* distribution of the heat transfer coefficient has the opposite trend, i.e., the highest cooling effect is experienced at the center location of the module and the lowest cooling effect is experienced at the sides. The axial gradients are due to the flow distribution in the test module. The coolant enters at the center, flows through the slit and after cooling the pressure boundary exits at the ports on each side, leaving the ends of the module with lower speed flow (Figure 4.16).

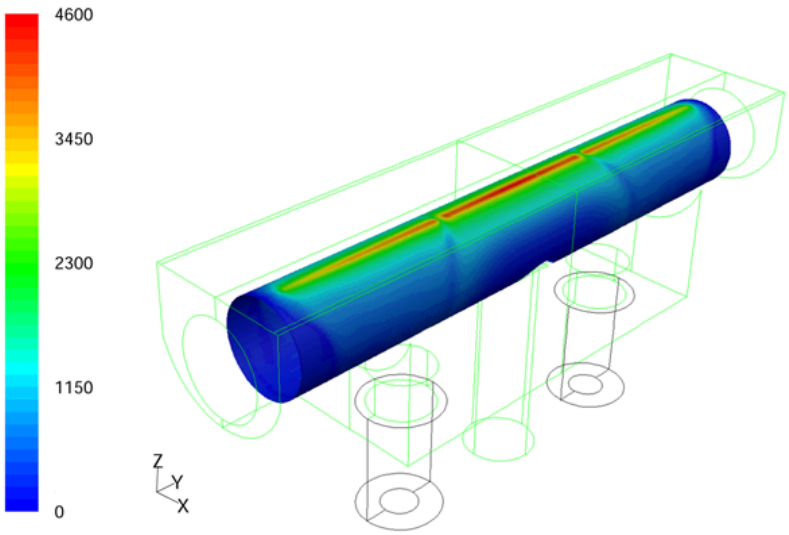

Figure 4.15: Contours of wall heat transfer coefficient (W/m^2·K) on the cooled surface of the brass T-block ($Re = 19,000$).

Once again, it is possible to recognize the effect of the bridges left uncut along the slot. While they seem to affect the local HTC (Figure 4.15), they have little if any effect upon the temperature distribution because of the thermal conduction in the brass (Figure 4.14).

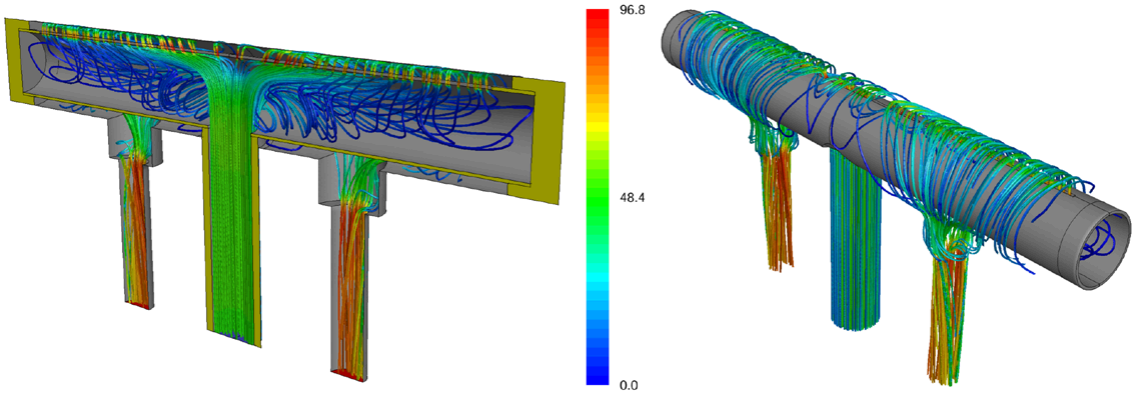

Figure 4.16: Coolant path lines colored by velocity magnitude [m/s] ($Re = 19,000$).

Finally, Figure 4.17, which shows the contours of temperature in the test module [left], demonstrates in a closeup of the "neck" of the concentrator [right], that the lines of constant temperature are horizontal, and hence, the heat flux incident on the brass T-block is planar (i.e., *one-dimensional*).

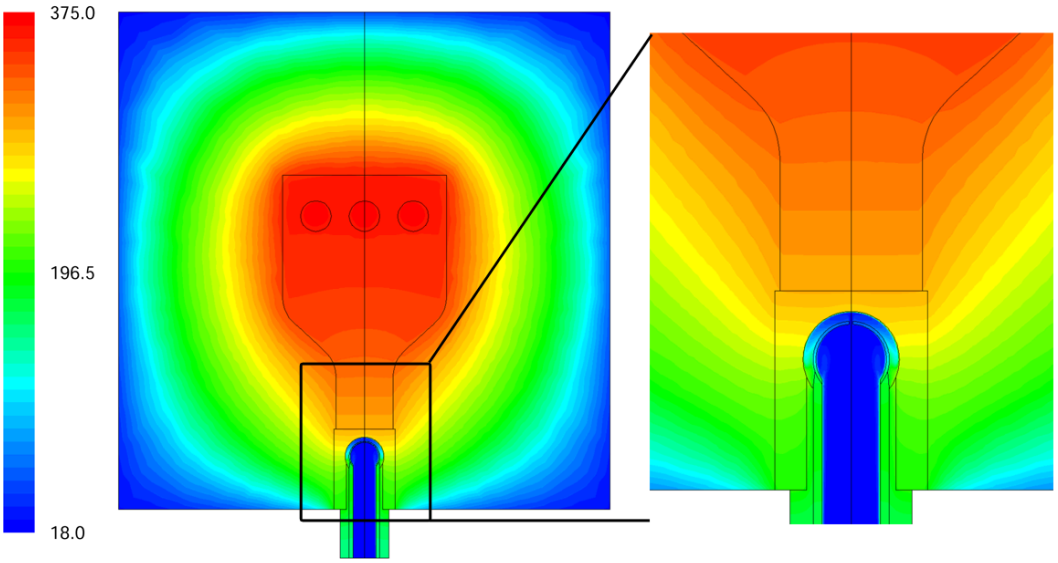

Figure 4.17: Contours of temperature across the test module (°C) [left] and magnification of the "neck" region [right]. The horizontal isotherms in the neck are proof of a planar incident heat flux.

4.3.2 Comparison of Experimental and Numerical Results

In this Section, the experimental data are compared to the model prediction described before. First, the heat transfer performance will be analyzed, followed by the pressure drop.

Figure 4.18 shows experimental (open symbols) and numerical (filled symbols) *azimuthal* temperature profiles for the experimental case #*TT*3. These results pertain to all the three axially instrumented locations. Planes #1 and #3 are symmetrically located along the T-block; plane #2 is in the center (Figure 4.7). The experimental data suggest, as expected, that the flow is symmetric with respect to the axial center line — compare results for the instrumented planes #1 and #3. Furthermore, the flow seems to satisfy azimuthal symmetry, since the same azimuthal TC locations are mirrored at axially symmetric instrumented planes #1 and #3 (Figure 4.7). The highest temperatures occur at $|\theta| = 0°$ and 30°, the two locations that are directly subject to the incident heat flux. The error bar in the temperature measurement is comparable to the size of the symbols.

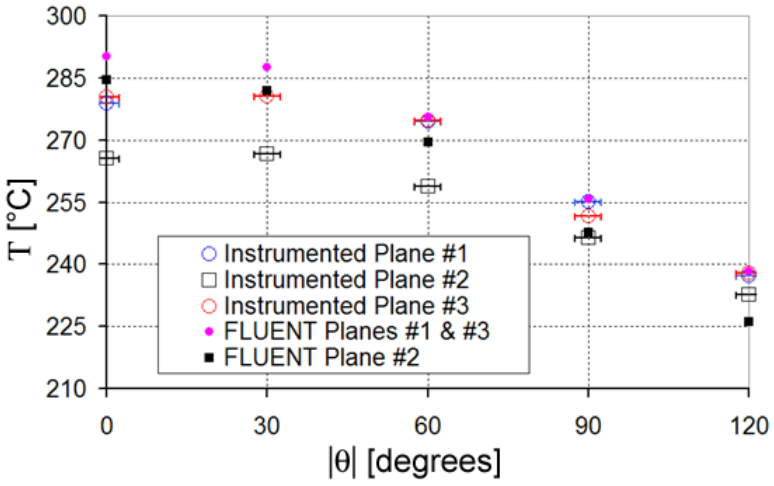

Figure 4.18: Experimental (open symbols) and numerical (filled symbols) $T(\theta)$ profiles for the three axially instrumented locations ($Re = 19,000$).

The numerical prediction of the temperature profiles shows reasonable agreement with the measured values. The code prediction is however conservative, as *FLUENT*® seems to *overestimate* the temperatures. The *Standard* $k-\epsilon$ turbulence model has been used in all calculations, also for consistency with the previous investigations.

Following the same reasoning adopted in Section 3.3.2, one can translate the temperature profiles into surface heat transfer coefficient profiles (Equation 3.5). The azimuthal HTC profiles for experiment #*TT*3 (Figure 4.19) show similar trend to what observed in the case of uniform heating, i.e., the heat transfer coefficient is maximum at the impinging jet stagnation point ($\theta = 0°$), then rapidly decreases away from the stagnation point ($|\theta| > 0°$). While the heat load produced by the copper concentrator is nearly one-dimensional, the azimuthal gradients in temperature profiles are due to the conduction in the brass T-block. The azimuthal gradients in surface heat transfer coefficient profiles are due to the impinging jet cooling effect.

Figure 4.20 shows the experimental *axial* temperature and HTC profiles for all the azimuthal locations. As predicted in the computer model (Figure 4.14) the center location of the module seems to be slightly cooler. However, the surface heat transfer

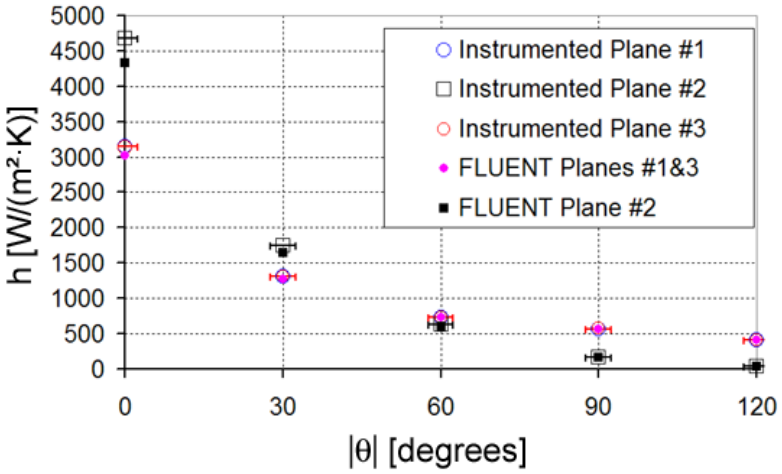

Figure 4.19: Experimental (hollow symbols) and numerical (solid symbols) $h(\theta)$ profiles for the three axially instrumented locations ($Re = 19,000$).

coefficient is maximum where the temperatures are minimum. This is due to the coolant distribution along the slit. The rectangular jet issues a larger amount of coolant in the middle section of the T, because of the location of the inlet port (Figure 4.16).

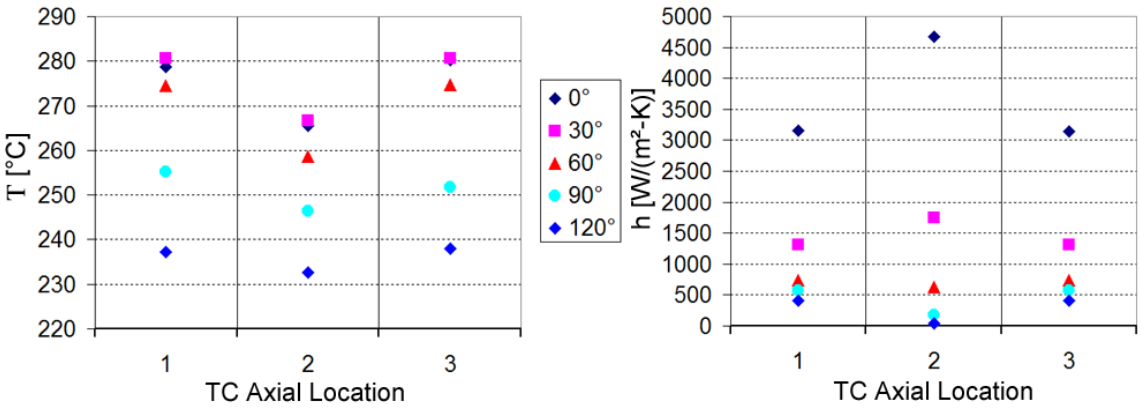

Figure 4.20: Experimental axial temperature (left) and HTC (right) profiles for $|\theta| = 0°$, $30°$, $60°$, $90°$ and $120°$ ($Re = 19,000$).

Table 4.3 compares experimentally measured and numerically predicted pressure drop in the test module for all the test cases. The pressure drop estimation is in good agreement with the experimental data except for test #1. The pressure drop in this case is very small because of the low Re and therefore subject to the largest

experimental errors. Nevertheless, *FLUENT*® in all cases slightly underestimates the pressure drop in the module for all the *Re* tested.

Table 4.3: Comparison of experimental ΔP_{exp} and numerically predicted ΔP_{CFD} pressure drop. All experiments have been run at a gauge pressure $P = 414\ kPa\ (60\ psi)$.

Exp. #	*Re* [-]	ΔP_{exp} [kPa (psi)]	ΔP_{CFD} [kPa (psi)]
*TT*1	4,800	6.9 (1.00)	3.2 (0.46)
*TT*2	11,800	21.5 (3.12)	18.0 (2.61)
*TT*3	19,000	46.5 (6.74)	45.1 (6.54)
*TT*4	19,000	52.9 (7.67)	47.0 (6.82)
*TT*5	30,400	141.7 (20.6)	136.7 (19.8)
*TT*6	30,400	139.5 (20.2)	136.7 (19.8)

4.3.3 Nusselt Number Calculations

The Nusselt number was calculated based on the slit hydraulic diameter $D_h = 0.92$ mm, and a constant thermal conductivity $k = 0.02521\ W/(m \cdot K)$ — the default value in *FLUENT*® for air (Equation 3.4). Since *Nu* is proportional to the heat transfer coefficient, its behavior is similar to that of the local HTC.

Figure 4.21 shows *Nu* as a function of *Re* at the impinging jet stagnation point for the three instrumented axial planes. The experimental data (symbols) include all cases reported in Table 4.1. For $Re = 19,000$ and $30,400$, two different values of the incident heat flux were tested — (0.55, 0.61) MW/m^2 and (0.75, 0.81) MW/m^2 respectively. For higher values of the heat flux, a higher Nusselt number seems to be measured, while maintaining the same *Re*. The value of the heat flux, however, should not affect the surface heat transfer coefficient, at least not directly. The variations in the measured *Nu* at a given *Re* are likely due to the *deformation* of the test module. Higher power inputs (i.e., higher incident heat fluxes) imply higher temperature gradients for a fixed *Re*, i.e., larger stresses and deformation that affect the *local gap width between the cooled surface and the slotted tube.*

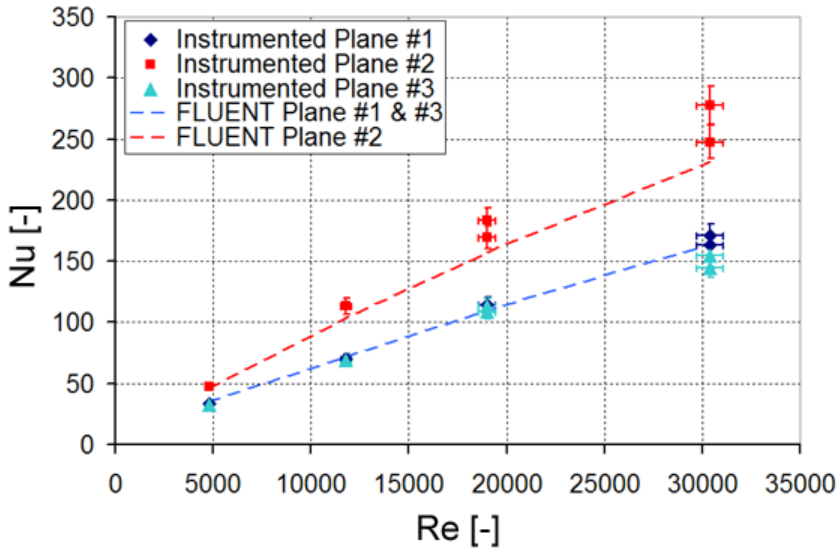

Figure 4.21: Experimental (symbols) and numerical (lines) Nu as a function of Re at the jet stagnation point $\theta = 0°$.

4.3.4 Comparison with the Uniformly Heated Test Section

In Section 4.3.1, the predicted HTC values for the single-sided heating case (Figure 4.15) have been compared with the values for the axisymmetrically heated case (Figure 3.15). The azimuthal HTC profiles for the two cases can be directly compared because of their similar slot width and annular gap dimensions.[2] Figure 4.22 shows the *azimuthal* surface heat transfer coefficients for both experimental test sections at matching $Re \approx 20,000$. For the single-sided heating case, experiment #*TT*3 is plotted at axial planes #1 and #2 (plane #3 is omitted because of the symmetry with plane #1). For the uniform azimuthal heating case, experiment #*TS*3 is plotted at axial plane #1. The data show that the *azimuthal* HTC profiles are essentially independent of the incident heat flux configuration, when matching the jet-to-wall spacing and Re.

It has also been discussed in Section 4.3.1 that, because of the opposite flow distribution between the two test sections, the *axial* HTC distribution is different.

[2] B = 0.6 mm, H = 1.1 mm for the uniform heating module vs. B = 0.45 mm, H = 1.25 mm for the single-sided heating apparatus.

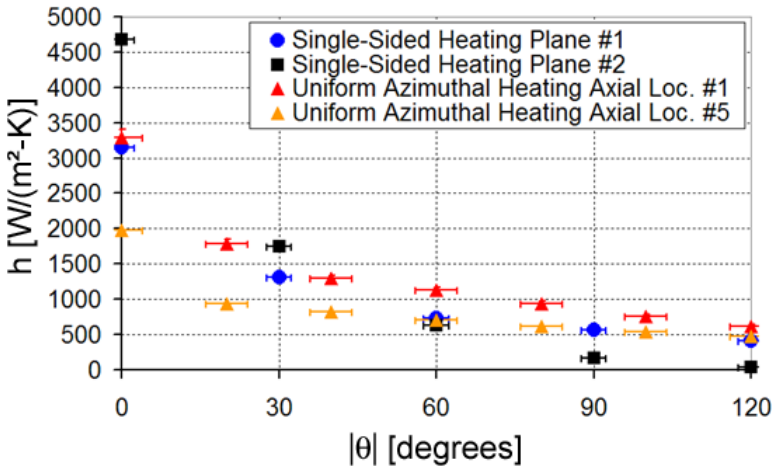

Figure 4.22: Experimental HTC profiles $h(\theta)$ for for both experimental test sections ($Re \approx 20,000$).

For the prototypical test module (i.e., T-tube with single-sided heating) the highest cooling effect is experienced at the center location; the behavior is inverted for the test module with axisymmetric heating (Figure 4.23). These data clearly show the effect of the flow configuration on the surface heat transfer coefficient distribution.

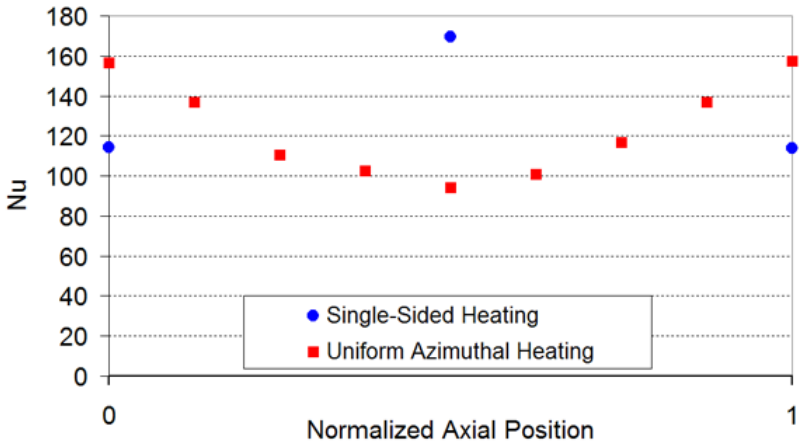

Figure 4.23: Experimental axial Nu profiles for for both T-tube experimental test sections at the jet stagnation point $\theta = 0°$ ($Re \approx 20,000$).

CHAPTER V

MULTI-JET APPARATUS (HEMJ)

In this chapter, the experimental and numerical studies conducted on a test section duplicating the helium-cooled multi-jet (*HEMJ*) finger divertor module are described. First, the experimental apparatus and procedures used in this investigation are detailed, followed by the numerical model. Finally, the results of the investigations are presented and discussed.

5.1 Experimental Apparatus and Procedures

5.1.1 Experimental Test Section

Figure 5.1 gives a schematic of the *HEMJ* test module. The test section can be divided into three parts:

1. The finger cartridge, which includes a concentric *thimble* and *jet cartridge*. This cartridge duplicates the proposed *HEMJ* "finger" (Section 2.2.2).

2. The tee, which provides the fittings for the coolant (air) and the instrumentation to monitor the flow.

3. The heater, which consists of a "bottle-shaped" copper block (*concentrator*), housing one cartridge heater. The concentrator provides the incident heat flux.

As shown in Figure 5.1, air enters the jet cartridge through the inlet pipe (light blue arrow), and is accelerated through the jets in the cartridge. After impinging on the inner surface of the thimble, the air flows as a turbulent channel flow along the gap between the jet cartridge and the inner surface of the thimble and is finally removed through the tee exit port (Figure 5.1, red [dark] arrow).

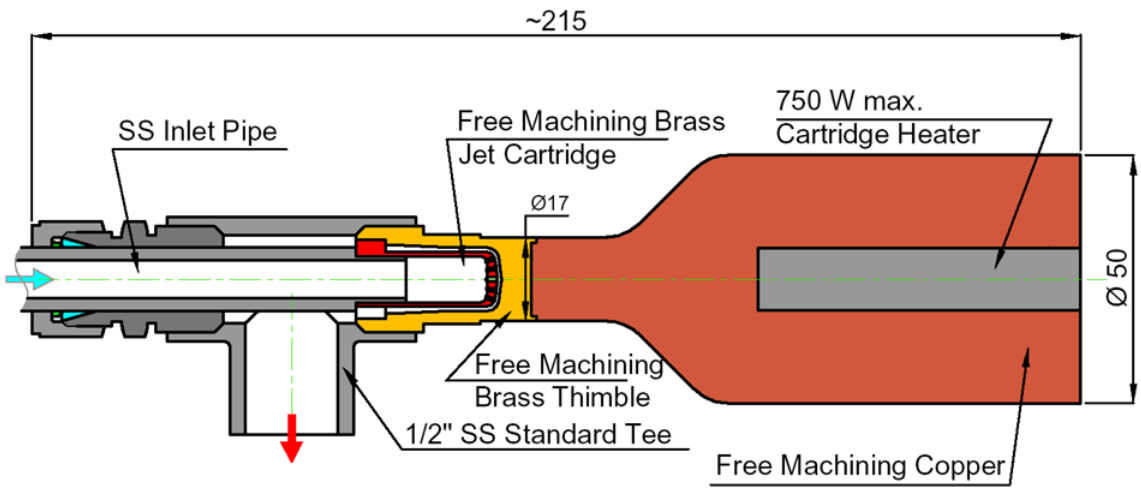

Figure 5.1: Schematic of the HEMJ test module.

The 36.3 mm long *thimble* with an inner-diameter of 12.94 mm, manufactured in C36000 brass (Figure 5.2), duplicates the tungsten alloy cap and tungsten armor tile of the proposed He-cooled HEMJ (Figure 2.12). The thimble houses a concentric *jet cartridge*, also manufactured from free machining C36000 brass of height 28.4 mm and outer diameter 11.14 mm (Figure 5.3). Both the thimble and the jet cartridge were fabricated by Hinman Shop at the Georgia Tech Research Institute. The thimble ID and the cartridge OD were selected to provide a jet-to-wall spacing $H = 0.9$ mm.

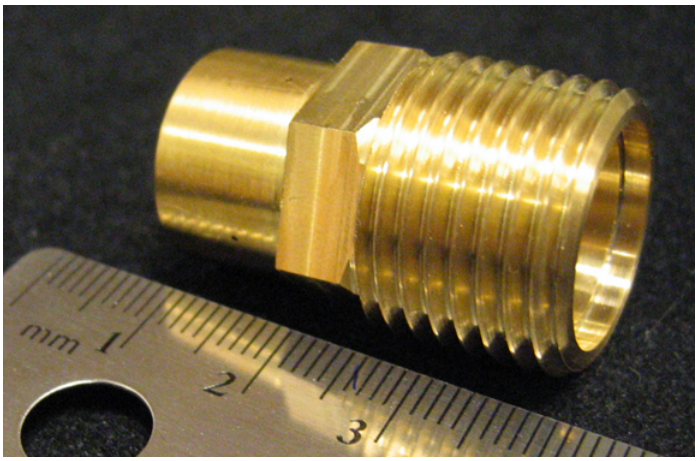

Figure 5.2: Picture of the brass thimble; the thread on the right end is 1/2" NPT.

The jet cartridge has twenty-four holes 0.6 mm in diameter laid out along four concentric "bolt" circles where each bolt circle consists of six holes evenly spaced 60° apart. Adjacent bolt circles have holes offset by 30° from each other. The center of the cartridge has a 1.0 mm diameter hole. Three sectors, each with an azimuthal extent of 30°, extend from the bottom of the jet cartridge, centering it in the thimble indention to ensure a consistent 0.9 mm gap between the top of the jet cartridge and the inner surface of the thimble. The jet cartridge is connected to the end of a 150 mm long tube made of 10.0 mm OD thin-walled SS 316 tubing by high temperature epoxy (*Devcon*® FasMetal 10).

Figure 5.3: Picture of the brass jet cartridge and SS inlet tube.

The 117 mm long cylindrical copper block (*concentrator*) produces a uniform axial heat flux across the thimble. The block was manufactured by the Hinman Shop at the Georgia Tech Research Institute from free machining C14500 copper (Figure 5.4). The heater block consists of a 50 mm diameter section housing a $FAST - HEAT$® Magnesium-Oxide cartridge heater in the center with a maximum output of 750 W, which exceeds the required input power needed to generate a nominal heat flux of 1.0 MW/m^2. The copper heater block contracts to a 17 mm diameter "neck" region which is brazed to the top of the thimble using silver solder.

Four E-type thermocouple probes (*OMEGA*® EMQSS-020G-6) are inserted in the brass thimble at varying depths spaced by 90° to measure the temperature distribution over the cooled surface (Figure 5.5). Table 5.1 gives the exact locations of the TC

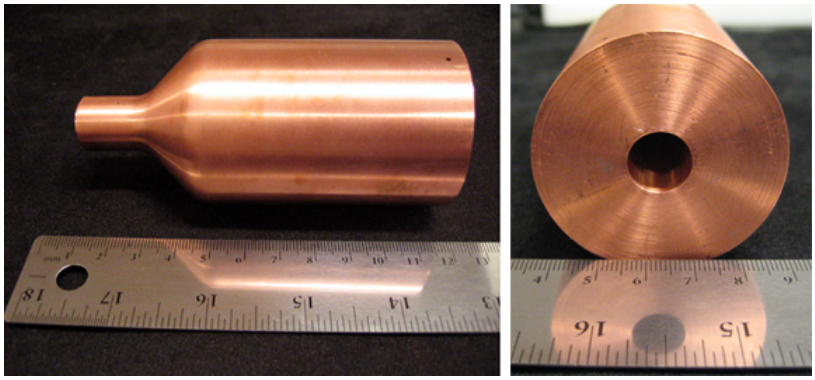

Figure 5.4: Picture of the copper heater block. The concentrator houses a cartridge heater (right).

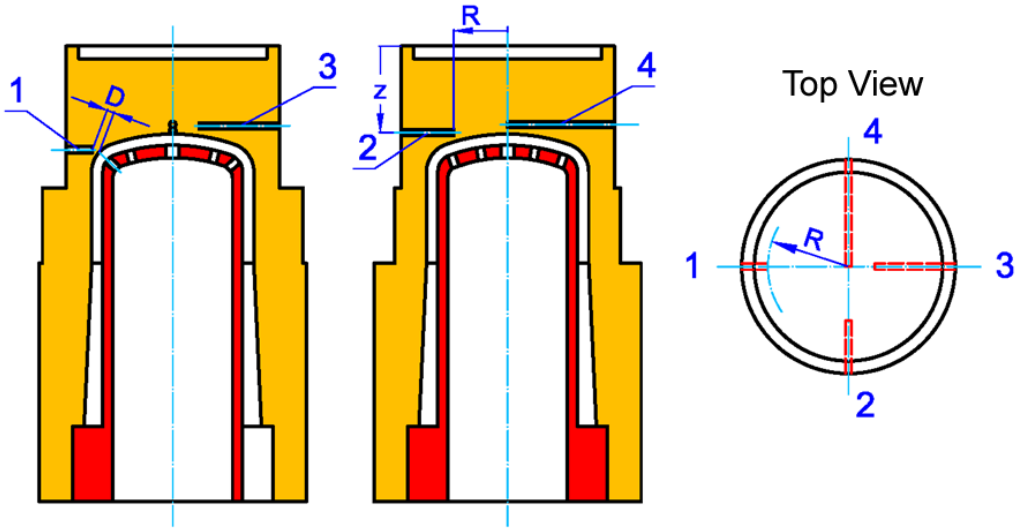

Figure 5.5: Schematic of the TC positioning in the thimble. These TCs are used to measure the temperature distribution on the cooled surface.

beads in the coordinate system defined on Figure 5.5. In all cases, the nominal distance of the bead center from the cooled surface is $D = 0.5$ mm.

Table 5.1: Coordinates of the thermocouple beads embedded in the brass thimble.

TC	R	z	D
#	[mm]	[mm]	[mm]
1	6.4	8.26	0.5
2	4.3	6.88	0.5
3	2.1	6.36	0.5
4	0.0	6.25	0.5

Three E-type thermocouple probes (*OMEGA*® EMQSS-020G-6) are embedded, spaced 90° apart, at axial locations of (3.0, 8.0, 13.0) mm from the brazing surface in the "neck" region of the concentrator (Figure 5.6). The reading from these TCs are used to calculate the measured axial heat flux. Two more E-type TCs (*OMEGA*® EMQSS-062U-6) are placed 5 mm from the top and at a depth of 16.0 mm in the copper block to monitor the peak temperature of the test section.

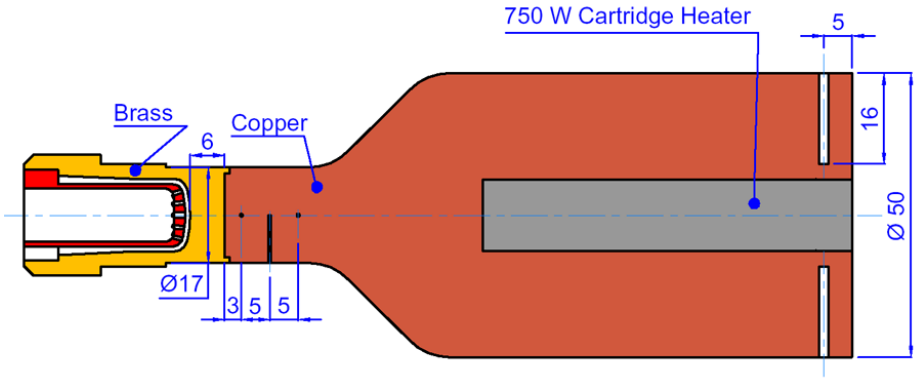

Figure 5.6: Schematic of the TC positioning in the copper block. Three TCs in the neck area are used to measure the incident heat flux; two additional TCs are used to monitor the maximum temperature in the copper.

After inserting the lead wires for each TC into its respective cavity, they were wrapped azimuthally around the neck section to reduce axial conduction and thermocouple probe movement. The TCs are secured by placing a thin layer of rock wool insulation around the test section and tightly winding a high strength nickel wire over the insulation (Figure 5.7).

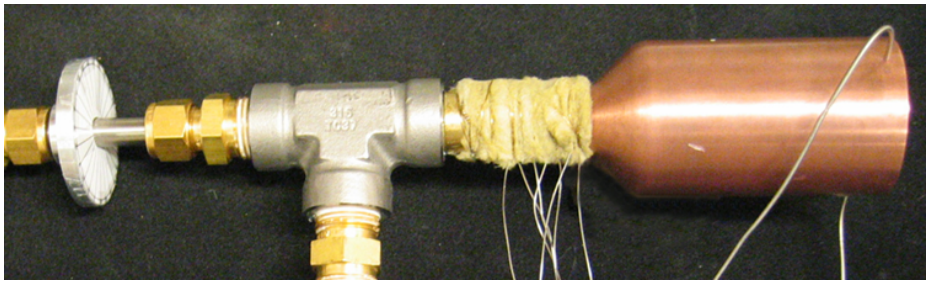

Figure 5.7: Picture of the test module. The copper heater block is silver-brazed to the top of the thimble which is screwed into a SS tee.

The assembled test section is shown in Figure 5.7. The brass thimble is screwed into a SS 1/2" NPT tee (*Parker* #8-8-8 FT). The jet cartridge, epoxied to the SS 316 tube, is inserted through the tee into the thimble and then secured and centered via a bored-through Swagelok® heat exchanger fitting. This fitting allows the inner SS 360 tube and thus the jet cartridge to rotate with respect to the thimble. An angular scale (Figure 5.8 [left]) and a steel "needle" are used to indicate the azimuthal position of the jet cartridge. θ is defined as the relative position of a jet on the outermost bolt circle measured from thermocouple #1 (Figure 5.8 [right]).

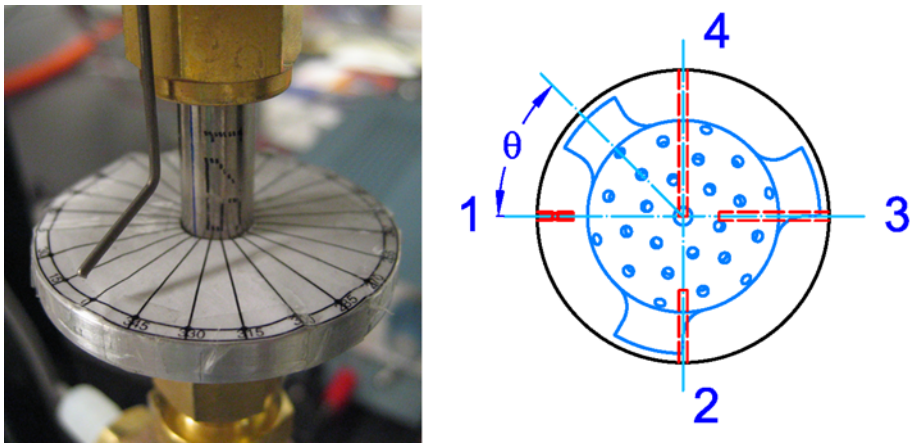

Figure 5.8: Photograph of the indexing system [left] and definition of the angular position θ [right].

The assembled HEMJ divertor test section is insulated with a 12.5 cm diameter cylinder of rock wool hollowed out at the center with a cavity that snugly fits the test section. The insulation extends 5 cm beyond the top of the copper heater block.

5.1.2 Experimental Flow Loop

Experimental studies were performed in an air flow loop (Figure 5.9). Air from a compressed-air line enters the loop at a gauge pressure of ~100 psi (724 kPa). The inlet pressure is measured with an analog test gauge (Ashcroft AMC-4291) which has a range of 0–200 psi with an accuracy 0.5 psi or 3.4 kPa. The inlet temperature is measured using an E-Type thermocouple (*OMEGA*® EMQSS-125G-6) in a 1/2" NPT

cross (*Lee USA*) which is attached to the 150 mm SS 360 tube via a bored-through Swagelok® fitting.

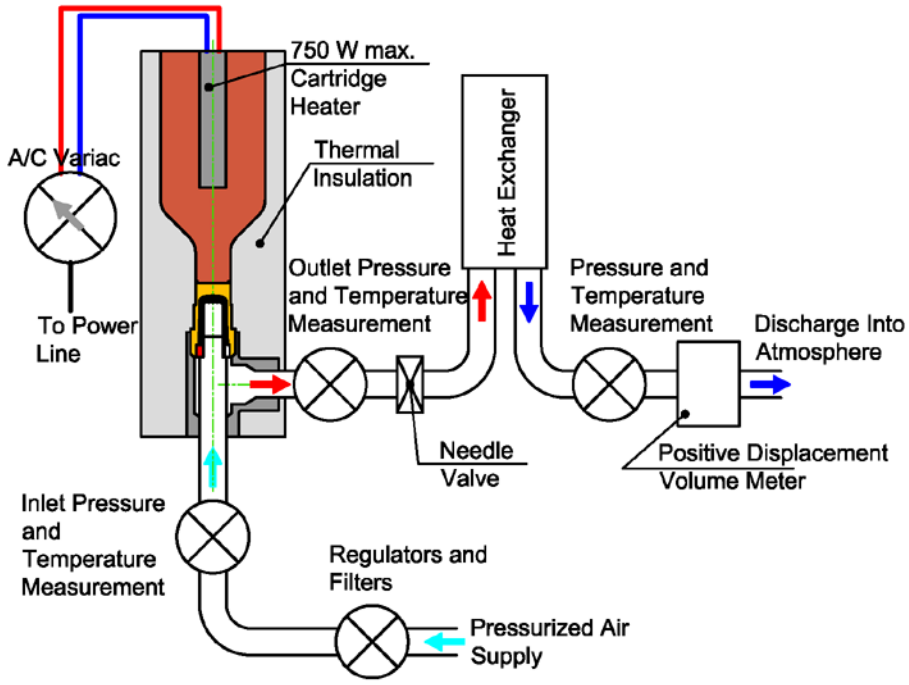

Figure 5.9: Flow loop diagram.

The exit pressure and temperature are measured with an *OMEGA*® pressure transducer (PX302-300AV) and *OMEGA*® Type-E thermocouple (EMQSS-125G-6), respectively. The temperature and pressure sensors, along with the outlet probes, are secured in a cross fitting attached to the SS tee of the test section. A needle valve (*Nupro Company*) downstream of the cross fitting controls the mass flow rate through the test section.

The mass flow rate is measured by a positive displacement gas volume meter (*Rockwell International* R-315). The air flows through a copper heat exchanger (*Parker Instrumentation* DYYC-55-4) before entering the flow meter to ensure that the temperature of the air exiting the test section does not exceed the maximum operating temperature of the flow meter. Air temperature and pressure are measured at the inlet of the flow meter with a thermocouple (*OMEGA*® Type-E) and a pressure

transducer (*OMEGA*® PX180-015GV); the air, after passing through the meter, is finally vented directly to the atmosphere.

The power input to the heater (i.e., the heat flux incident on the thimble) is controlled by adjusting the voltage to the heater with a variable autotransformer (*Staco Energy Products* 3PN1010V). The voltage and current are both measured with digital multimeters (*Hewlett Packard* 34401 A and *Fluke* 25, respectively).

5.1.3 Experimental Parameters and Procedures

The test conditions studied here bracket the values of the important dimensionless groups for the actual *HEMJ* divertor module. The most important dimensionless group is the Reynolds number based on the diameter of the central jet $D_{jet} = 1.0$ mm, the average speed $\overline{V}$ through the jets and the coolant properties at the test section inlet:

$$Re_{jet} = \frac{\dot{m} D_{jet}}{A_{jets} \mu_{in}} \tag{5.1}$$

The *Re* expected for the He-cooled HEMJ under nominal operating conditions is 21,400 (Table 5.2). The range of *Re* spanned by this investigation is $Re = 14,200$–$59,300$. In this investigation, experiments were performed at power inputs corresponding to nominal heat fluxes $\dot{q}''_{nom}$ =(0.5, 0.8, 1.0) MW/m^2 in the 17 mm diameter neck region of the copper heater block. Twenty experiments were run with the jet cartridge at a fixed azimuthal position while changing coolant mass flow rate (Section 5.1.3.1). Five experiments were run at constant mass flow rate and incident heat flux at different azimuthal positions of the jet cartridge (Section 5.1.3.2). The air studies described here are complemented by experiments performed using an exact duplicate of this HEMJ divertor test section (designed and constructed by GT) in the HEBLO helium flow loop at Forschungszentrum Karlsruhe (FZK).

Table 5.2: Comparison of nominal operating conditions in the DEMO reactor, the HEBLO test facility (FZK) and the air loop (GT).

Parameter		**Air loop (GT)**	**Helium (FZK)**	**Helium (DEMO)**
P_{oper}	[MPa]	0.720	8.0	10.0
μ_{in}	[kg/m·s]×10^{-5}	1.85	2.04	4.16
$\dot{m}$	[g/s]	2.0–8.0	1.2–6.3	6.8
$\dot{q}''_{nom}$	[MW/m^2]	0.5, 0.8, 1.0	1.0, 2.0	10.0
T_{in}	[°C]	20	35	600
Re	[-]	14,000–56,000	7,700–40,400	21,400
Pr	[-]	0.71	0.71	0.66

5.1.3.1 Constant Azimuthal Angle Experiments

During the constant azimuthal angle experiments, the power input to the heater (i.e., the heat flux incident on the thimble surface) and the azimuthal position of the jet cartridge remained constant at $\theta = 0°$ while the mass flow rate was varied. The experiments were performed as follows:

1. The flow loop is pressurized to a pressure between 710 kPa and 730 kPa.
2. The heater power is then set with the variable autotransformer.
3. The desired mass flow rate is set by adjusting the exit needle valve.
4. Once the temperatures in the test section reach steady state[1] for the given mass flow rate, the data are collected.
5. Adjust the needle valve to the next mass flow rate value to be tested and repeat step 4.

Table 5.3 details the constant azimuthal angle experiments performed in this thesis. Tests *#MJ6* through *#MJ15* were carried out to verify the repeatability of the

[1]The temperatures were assumed to have reached "steady-state" when the thermocouple probe readings sampled at 0.2 Hz remained constant within ±0.5 °C for 10–15 data scans.

experiment. The average time required to reach steady-state was approximately 1 h (starting with a "cold" test module). Once the apparatus was at steady-state, an additional 30 min were required after each adjustment to a different mass flow rate.

Table 5.3: Constant azimuthal angle experiments. All tests have been performed at $\theta = 0°$.

Test	$\dot{m}$	Re	$\dot{Q}$	$\dot{q}''_{nom}$	$\dot{q}''_{net}$	ΔP
#	[g/s]	[-]	[W]	[MW/m^2]	[MW/m^2]	[kPa]
*MJ*1	2.00	14,100	113.2		0.43	9.6
*MJ*2	3.05	21,600	113.1		0.45	20.7
*MJ*3	4.10	29,000	113.1	0.50	0.45	32.4
*MJ*4	6.30	44,500	114.0		0.46	90.7
*MJ*5	8.29	58,600	114.4		0.48	177
*MJ*6	2.08	14,700	182.3		0.70	11.0
*MJ*7	3.11	22,000	182.3		0.71	17.9
*MJ*8	3.99	28,200	182.2	0.80	0.72	35.9
*MJ*9	6.01	42,500	181.5		0.72	73.8
*MJ*10	8.39	59,300	181.2		0.73	177
*MJ*11	2.01	14,200	181.4		0.69	9.7
*MJ*12	3.16	22,300	182.2		0.71	22.1
*MJ*13	4.20	29,700	182.8	0.80	0.72	41.4
*MJ*14	6.10	43,100	182.9		0.72	77.2
*MJ*15	8.06	57,000	182.8		0.73	152
*MJ*16	2.07	14,600	228.4		0.88	11.7
*MJ*17	3.10	21,900	227.0		0.90	24.1
*MJ*18	4.05	28,600	226.6	1.00	0.89	35.2
*MJ*19	6.20	43,800	227.6		0.90	84.1
*MJ*20	8.18	57,800	227.9		0.92	166

5.1.3.2 Rotation Experiments

During the rotation experiments, the power input to the heater (i.e., the heat flux incident on the thimble surface) and the mass flow rate remained constant while the azimuthal position of the jet cartridge, θ, was varied by rotating the cartridge. These experiments gave azimuthal profiles of the temperature distribution on the cooled surface of the HEMJ divertor test section. The experiments were performed as follows:

1. Repeat steps 1–3 for the $\theta = 0°$ tests (Section 5.1.3.1).

2. Once the experimental conditions reached steady-state (with the same criteria described before), the data are collected.

3. Loosen the Swagelok® fitting at the inlet of the test section while maintaining an upward force on the SS tube. Rotate the SS tube and thus the jet cartridge to the desired azimuthal position θ as indicated by the steel needle. Tighten the Swagelok® fitting at the new azimuthal position.

4. Verify that the mass flow rate remains constant.

5. Repeat steps 2–4 as required.

Table 5.4 details the rotation experiments performed; in all cases, θ was varied by $15°$ increments over a total azimuthal extent of $60°$ or $120°$ based on the 6-fold symmetry of the HEMJ jets, resulting in a total of thirty-eight rotation experiments.

Table 5.4: List of the rotation experiments.

Test	$\dot{m}$	***Re***	θ **(range)**	$\dot{Q}$	$\dot{q}''_{nom}$	$\dot{q}''_{net}$	ΔP
#	[g/s]	[-]	[°]	[W]	[MW/m^2]	[MW/m^2]	[kPa]
*MJ*21	3.05	21,600	0–60	113	0.50	0.45	20.0
*MJ*22	3.03	21,400	0–60	182	0.80	0.70	17.5
*MJ*23	2.07	14,600	0–60, 180–240	228		0.89	11.9
*MJ*24	3.03	21,400	0–120	227	1.00	0.89	16.5
*MJ*25	4.05	28,600	0–120	227		0.89	32.9

5.2 Numerical Modeling

The numerical studies were carried out with the same CFD package used for the previous investigations (*FLUENT*® and *Gambit*® 2.2.30). Initially, several models of the test section were developed during the design of the test module to help selecting the experimental parameters. The final computer model duplicates in detail the

experimental test section as built; the numerical simulation results from this model were then compared to the experimental data (Section 5.3).

5.2.1 Model Geometry

The model used for the numerical studies detailed in this section was built using the 3D CAD software package Solidworks® 2006 to exactly match the dimensions and features of the experimental test section described previously. The model included the electric heater, copper concentrator, brass thimble, jet cartridge, tee, insulation, inlet tube, and outlet connector (Figure 5.10).

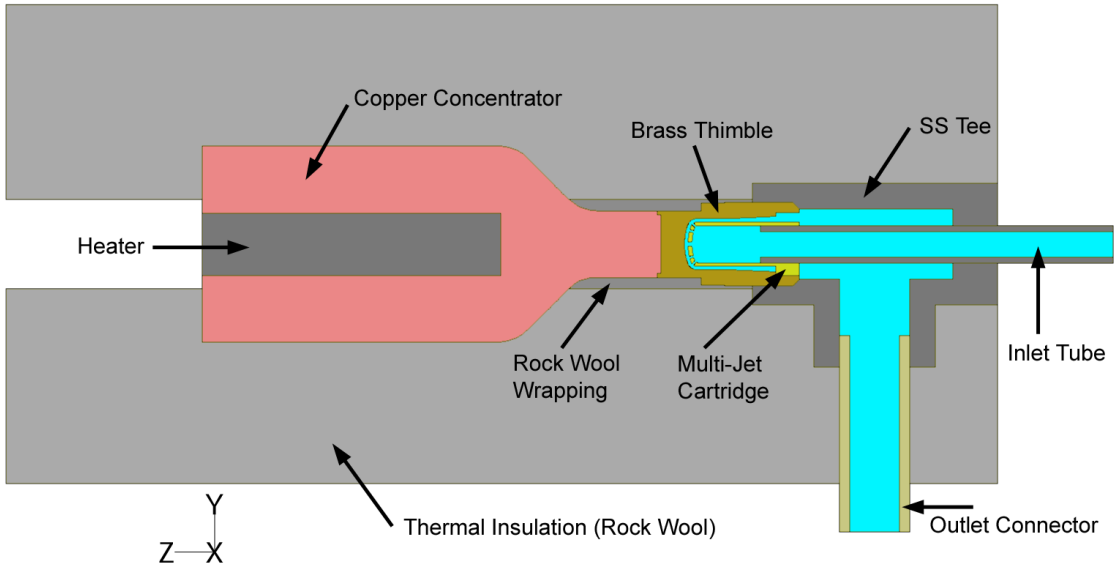

Figure 5.10: Half-model geometry used for the numerical calculations. The model includes all the components of the actual test module.

The copper concentrator, brass thimble, cartridge heater, inlet tube and insulation are axisymmetric, while the jet cartridge has a six-fold symmetry. All these features would suggest that only a section of 60° could be modeled. The coolant discharge port on one side of the test apparatus, however, necessitated the use of at least a half-model spanning 180° of the test section.

5.2.2 Grid Generation

The CAD model was imported into *Gambit*® 2.2.30 to generate the face mesh and volume grid for simulation in the CFD software package *FLUENT*® 6.2.16. The final half-model used 1,456,460 grid cells with 695,360 nodes. This grid was constructed by projecting face meshes along the volumes of the model. The grid is much finer in the regions of jet impingement (Figure 5.11). In areas of complex geometry, such as the jet impingement regions and the tee, a tetragonal/hybrid (unstructured) grid was used (Figure 5.12). The convergence criteria of the numerical solution are the same as those described in Section 3.2.4.

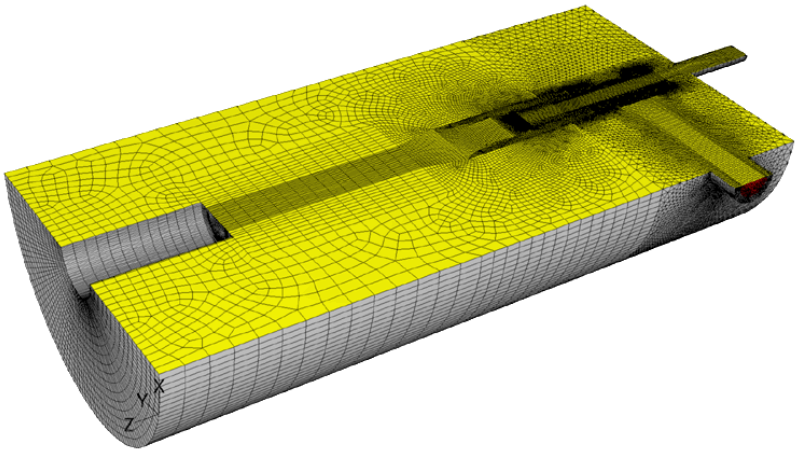

Figure 5.11: Grid of the half-model geometry used for the numerical calculations. The majority of the grid consists of *brick* (rather than tetragonal) elements.

5.2.3 Boundary Conditions

The boundary conditions used in the simulations, defined in *FLUENT*®, specify:

- $\dot{Q}_v'''$: The power input to the heater, i.e., uniform heat generation rate per unit volume [W/m^3]
- $\dot{m}_{in}$: Coolant mass flow rate at the inlet [kg/s]
- T_{in}: Coolant temperature at the inlet [°C]

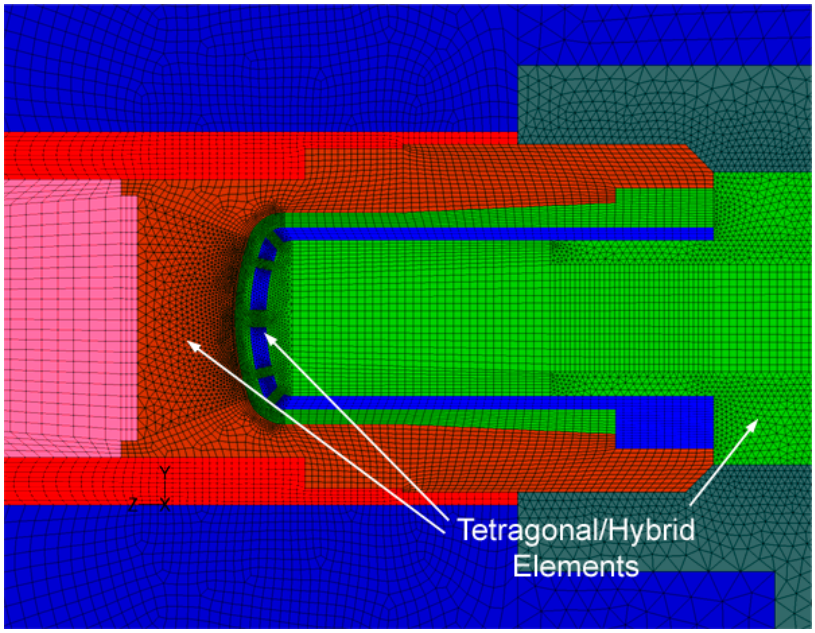

Figure 5.12: Detail of the grid in the jets impingement region. Due to the complexity of the geometry, only unstructured grid elements could be used in this area.

- P_{out}: Gauge exit pressure [Pa]
- P_{oper}: Operating pressure [Pa]
- h_{amb}: Heat transfer coefficient between the test module and the ambient, i.e., the outer insulation surface [W/(m^2·K)]. The value of HTC value varies among the different surface regions: $h_{amb} = 5\ W/(m^2 \cdot K)$ for region A, and $h_{amb} = 15\ W/(m^2 \cdot K)$ for region B (Figure 5.13)
- T_{top}: Temperature of the copper free surface at the top of the test module (label C, Figure 5.13)

The values for h_{amb} are based on the results obtained in the T-tube cases. All other parameters correspond to their respective measured values for each experiment. The surface temperature T_{top} at location C (Figure 5.13) was measured by manually inserting a thermocouple probe (*OMEGA*® Type-E) at that location.

The material properties used for this numerical model are the same as those for the single-sided T-tube investigation in Section 4.2.3, and the coolant (air) properties

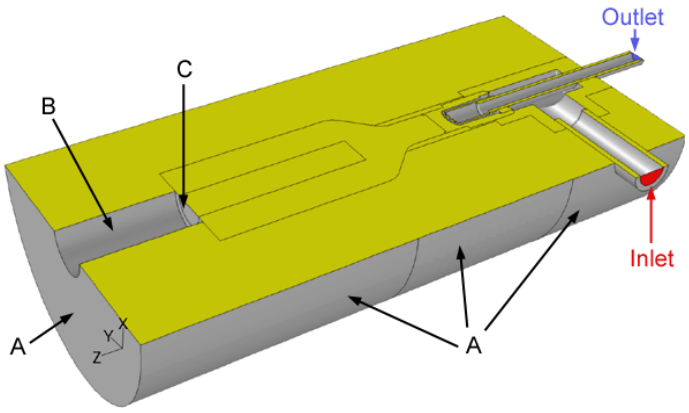

Figure 5.13: Geometry of the computer model with labels for the BCs.

are identical to those reported in Section 3.2.3.

For all the numerical *FLUENT*® simulations, the *Standard* $k-\epsilon$ closure equations with standard wall functions were used as the turbulence model. This is consistent with the investigation conducted on the T-tube test modules.

5.3 Results and Discussion

5.3.1 Nominal Test Case Results

This section details the numerical results for the air-cooled HEMJ test module under nominal operating conditions ($Re = 21,400$, Table 5.2). Figure 5.14 shows the temperature distribution of the HEMJ divertor test section model.

A closeup view of the neck region of the concentrator shows that a flat temperature distribution is achieved along $X-Y$ planes (Figure 5.14 [right]). This implies a nearly uniform incident heat flux in the *axial*, i.e., Z dimension.

The temperatures and convective heat transfer coefficient (HTC) on the "cupped" area above the impinging jets (i.e., the cooled inner surface of the brass thimble) are of primary interest for this investigation. The contours in Figure 5.15 [left] show that the temperature distribution on the cooled surface is fairly uniform, i.e., it is independent of the position of the jets. This is primarily due to the heat conduction in the the relatively high thermal conductivity brass.

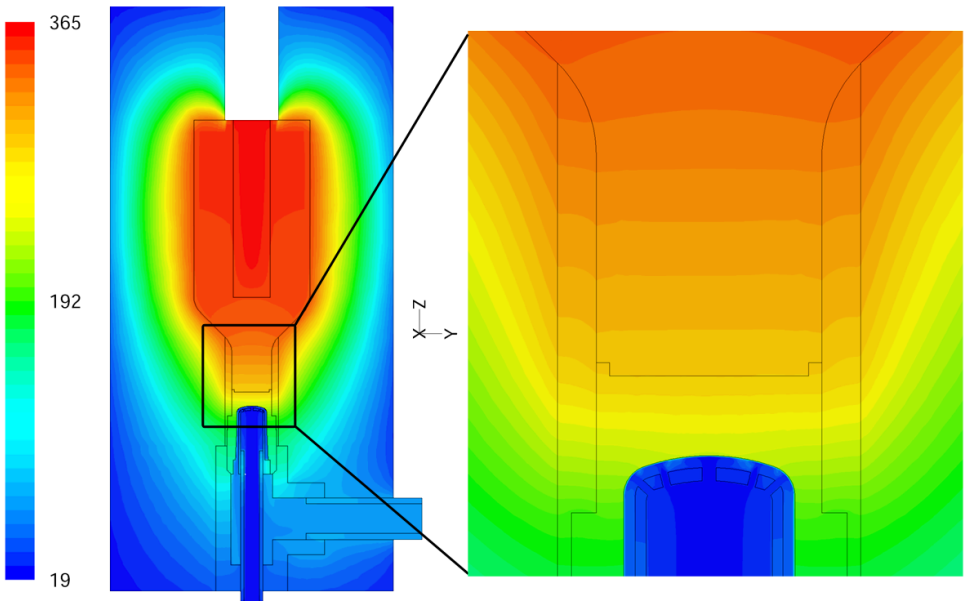

Figure 5.14: Temperature distribution (°C) across the test module [left] and in a closeup of the concentrator neck [right]. Note the nearly uniform incident heat flux on the brass thimble.

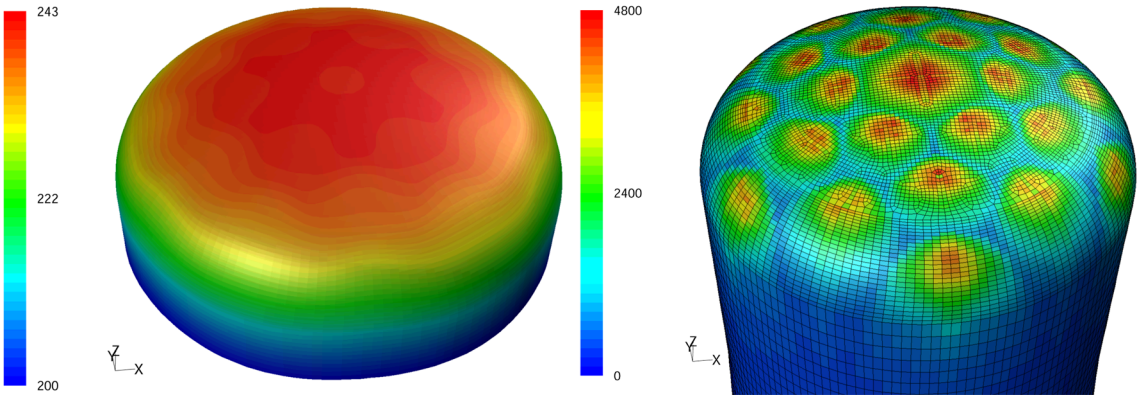

Figure 5.15: Wall temperature (°C) [left] and wall heat transfer coefficient ($W/m^2 \cdot K$) [right] distributions on the cooled surface of the brass thimble ($Re = 21,400$).

As expected, the convective heat transfer coefficient is greatest near each jet; note the especially large area of high HTC corresponding to the larger central jet (Figure 5.15 [right]). The HTC values are similar to those obtained in the T-tube investigations (Figures 3.15 and 4.15) at a similar jet-based *Re*.

Figure 5.16 shows pathlines, colored by the magnitude of the velocity, of the coolant flowing through the jets and impinging on the cooled surface of the thimble.

The flow distribution through the jets is fairly uniform. Adjacent jets interact and form a "fountain" after impinging on the cooled surface. The air then exits the region between the jets and the cooled surface, flowing through the gap between cartridge and thimble.

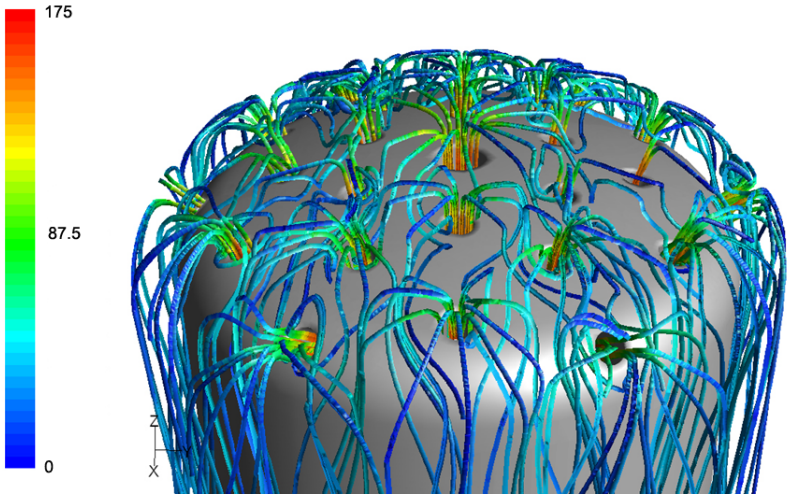

Figure 5.16: Coolant path lines colored by velocity magnitude [m/s] ($Re = 21,400$).

5.3.2 Comparison of Experimental and Numerical Results

This section compares and discusses the experimental and numerical results. The calculation of the local Nusselt number will follow.

The experimental temperature measurements from the TCs in the brass thimble (Figure 5.5, $\#1 - 4$) were compared to the numerical predictions of the temperature distribution. Since the TCs read temperature inside the thimble, a point was created in the *FLUENT*® model at the location corresponding to the center of the bottom of each thermocouple hole.

Figure 5.17 compares temperature results from experiment *#MJ7* and *FLUENT*® 6.2 simulations for $Re = 22,000$. The experimental and numerical results are in good agreement. Figure 5.18 shows that the numerical and experimental temperature results are in good agreement over the entire range of mass flow rates studied here. The Figure only shows readings from TCs #1 and #4, which are the lowest and

highest temperatures, respectively; the readings from TCs #2 and #3 were always between these extremes. The experimental data are slightly lower that the predicted temperatures; this may be due to the contact resistance between the TC beads and the bottom of the TC holes.

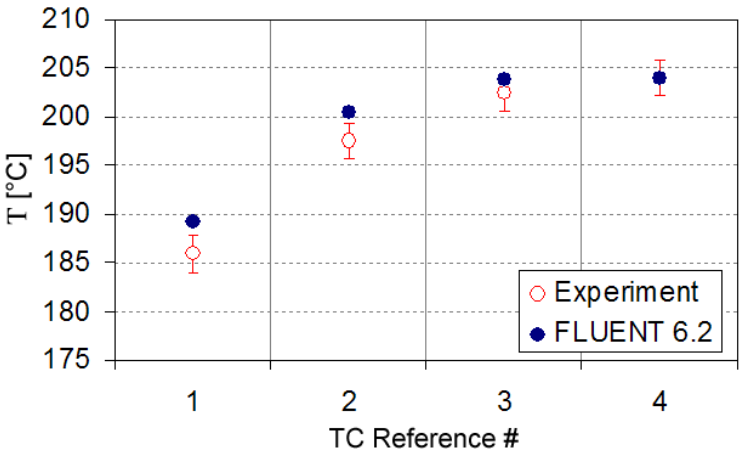

Figure 5.17: Plot of the embedded temperature results for experiment #*MJ7* ($Re = 22,000$).

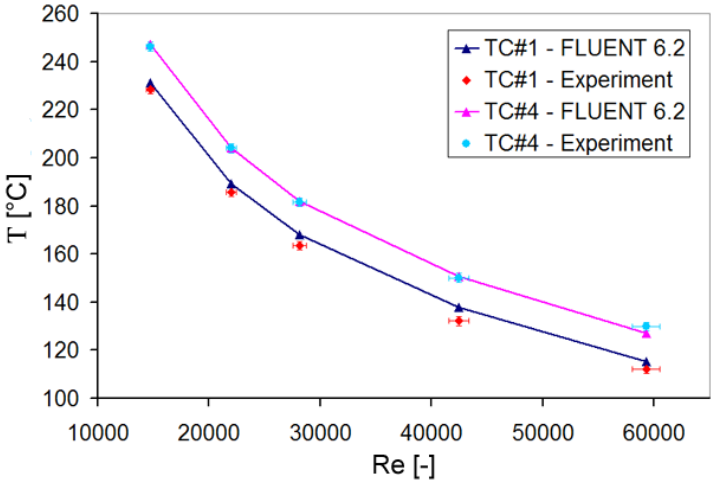

Figure 5.18: Plot of the embedded temperature results for TCs #1 and #4 across the entire Reynolds number range spanned during this experimental investigation.

The temperature on the inner (cooled) surface of the brass thimble is required to determine the surface heat transfer coefficient (HTC). After validating the *FLUENT*® model with the experimentally measured temperatures inside the brass thimble, the

surface temperatures in the numerical model were determined by projecting each of the four embedded thermocouple locations to the cooled surface. The temperature difference between embedded location and corresponding surface point (ΔT_{cond}) was then used to correct the experimental values for the conduction between the thermocouple embedded location and the jet impingement surface (Equation 5.2). The correction, however, was often within the experimental error.

$$T_{surf} = T_{emb} - \Delta T_{cond} \tag{5.2}$$

The convective HTC values calculated from the experimentally measured temperatures and predicted by the numerical simulations were in very good agreement, as shown in Figure 5.19 for $Re = 22,000$. The HTC is maximum near the surface under thermocouple #4 due to the impingement of the central jet upon TC #4. A smaller jet impinges on the surface above thermocouple #1 at $\theta = 0°$ (Figure 5.8). The local HTC at the locations corresponding to TCs #2 and #3 are lower than those at #1 and #4 because there is no direct impingement of a jet on these locations. Figure 5.20 shows the plot of the convective HTC, over the full range of mass flow rates spanned in this investigation.

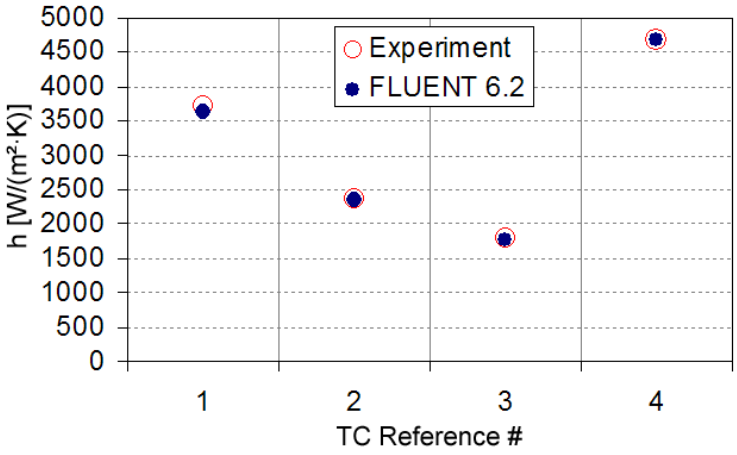

Figure 5.19: Plot of the surface heat transfer coefficient results for experiment #*MJ7* ($Re = 22,000$).

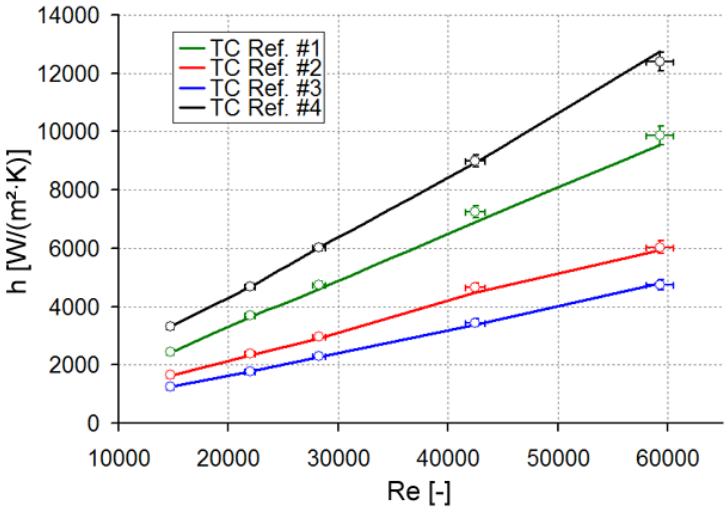

Figure 5.20: Plot of experimental (symbols) and numerical (lines) surface heat transfer coefficient results across the entire Reynolds number range spanned during this experimental investigation ($\theta = 0°$).

The experimentally measured surface temperatures showed a pattern similar to the numerical results (Figure 5.21). Thermocouple reference #1 has the lowest temperature at $\theta = 0°$, when it is next to a jet. At $\theta = 60°$, the thermocouple is at a location equivalent to the $\theta = 0°$ position. The experimental values at $\theta = 60°$ and $\theta = 0°$ are in close agreement with each other as expected. The highest temperature should occur when the thermocouple is farthest from a direct jet impingement location. For thermocouple reference #1, this corresponds to the $\theta = 15°$ and $\theta = 45°$ locations.

The surface temperatures predicted by *FLUENT*® are consistently higher (even if only by a few °C) than those experimentally measured. This is primarily due to the contact resistance between the TC beads and the bottom surface of the TC holes; it could also be due to the uncertainty in the boundary conditions assumed in the calculations (such as the temperature at the top of the copper block T_{top}, the mass flow rate $\dot{m}_{in}$ and the power input $\dot{Q}$). Nevertheless, the differences between the calculated and measured temperatures are small, so that the corresponding effect on the surface heat transfer coefficient is nearly negligible.

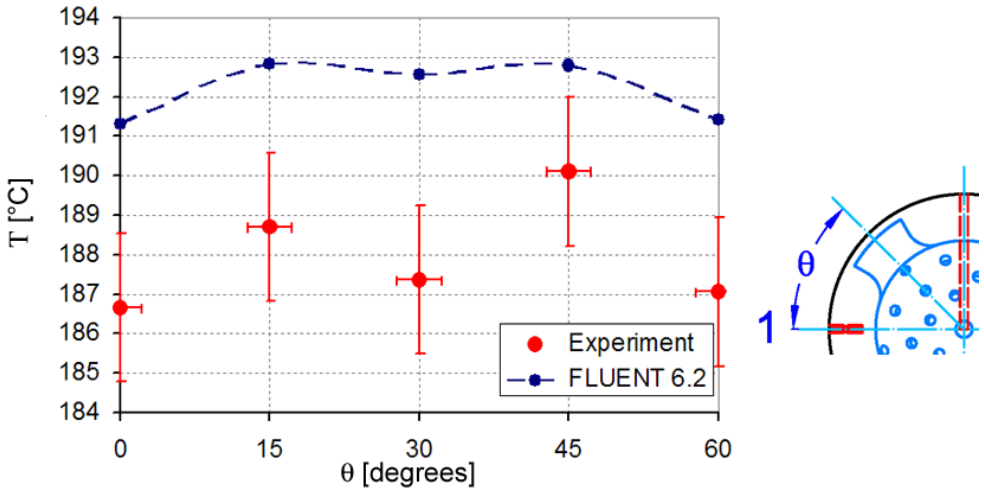

Figure 5.21: Azimuthal surface temperature profile for thermocouple position #1 for experiment #*MJ*22 ($Re = 21,400$).

While azimuthal temperature fluctuations on the cooled surface are fairly small, the gradients in the *local* heat flux are very steep, directly affecting the HTC profiles (Figures 5.15, 5.19 and 5.21). The azimuthal variations of the local heat transfer coefficient for experiment #*MJ*22 are plotted in Figure 5.22. The apparent better agreement on HTC vs. temperature profiles is mainly due to the difference in the scale of the plots and to the definition of the HTC (Equation 3.5).

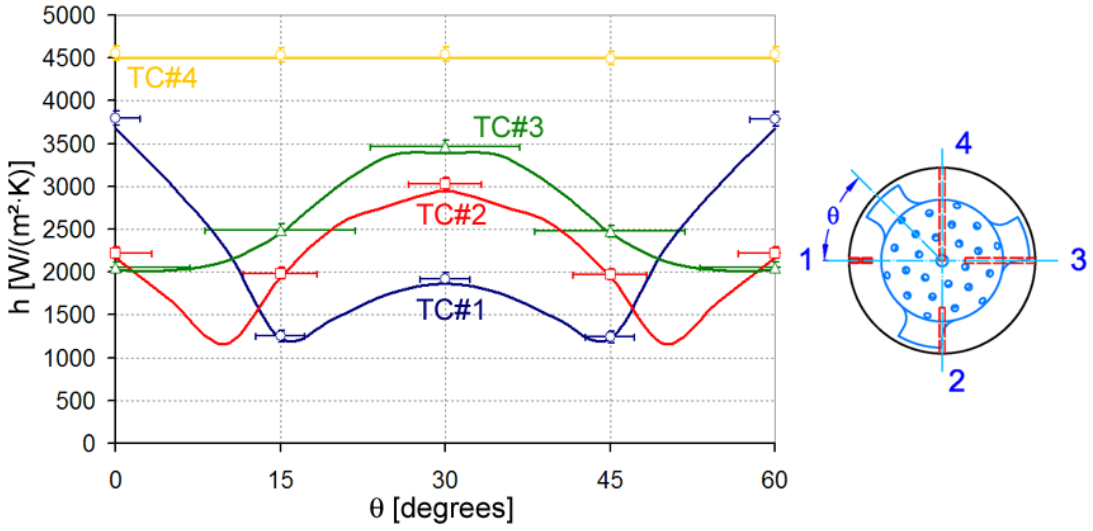

Figure 5.22: Experimental (symbols) and *FLUENT*® (lines) azimuthal surface HTC profiles for experiment #*MJ*22 ($Re = 21,400$).

The experimentally measured pressure drop was compared with numerical predictions to further validate the numerical simulations. Note that although the exit pressure is set to the experimentally measured value, the inlet pressure is free to vary during the simulation.

The experimentally measured pressure drop was within ~ 12 % of the *FLUENT*® prediction (Figure 5.23). For the experimental cases at the lower *Re*, the *FLUENT*® prediction differed by as much as ~ 26 % from the experimental values, due to the higher relative experimental error in the measurement of the pressure drop at low flow rates (Appendix A). However, the pressure drop from the numerical simulations consistently underestimated the experimentally measured values, due in part to the presence in the experiments of a 1.7 m long section of Tygon tubing and a valve between the site of the inlet pressure measurement and the HEMJ divertor test section. The numerical model does not include the tubing or the valve and therefore does not include the pressure drop due to these parts of the flow loop. Such additional pressure drop, however, can be estimated to be ~ 1 psi for the higher *Re*.

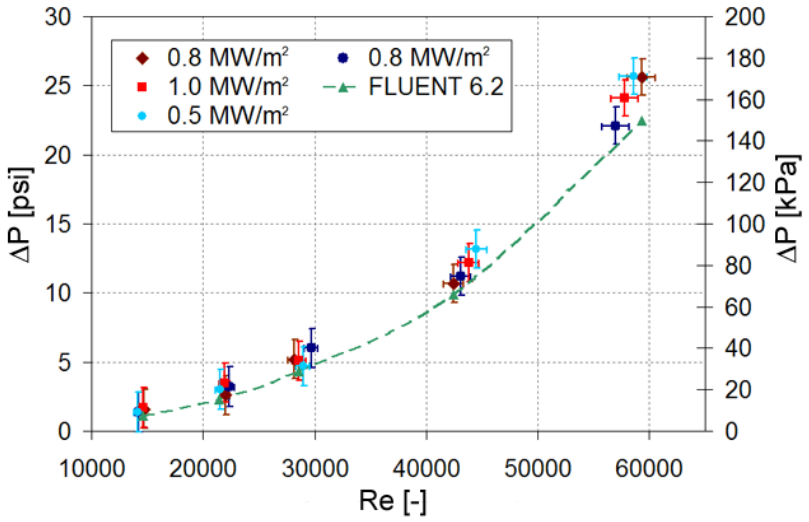

Figure 5.23: Plot of experimental (symbols) and numerical (line) $\Delta P(Re)$.

5.3.3 Nusselt Number Calculations

The Nusselt number was calculated based on the diameter of the central jet D_{jet} = 1.0 mm, and a constant thermal conductivity $k = 0.02521\ W/(m \cdot K)$ — the default value in *FLUENT*® for air (Equation 3.4). Since Nu is proportional to the heat transfer coefficient, its behavior is similar to that of the local HTC.

The values of Nu shown in Figure 5.24 can be compared with the results obtained for the T-tube investigation (Figure 4.21, 3.25 and 3.26). For $\theta = 0°$ the Nusselt number is maximum at TC locations #1 and #4 due to direct jet impingement at those locations. Furthermore, values of Nu for TC location #4 are the highest because the center jet diameter (1.0 mm) is larger than that of the other jets (0.6 mm). As in the single-sided T-tube case the Nu increases slightly with the incident heat flux, with the greatest effect at TC location #1.

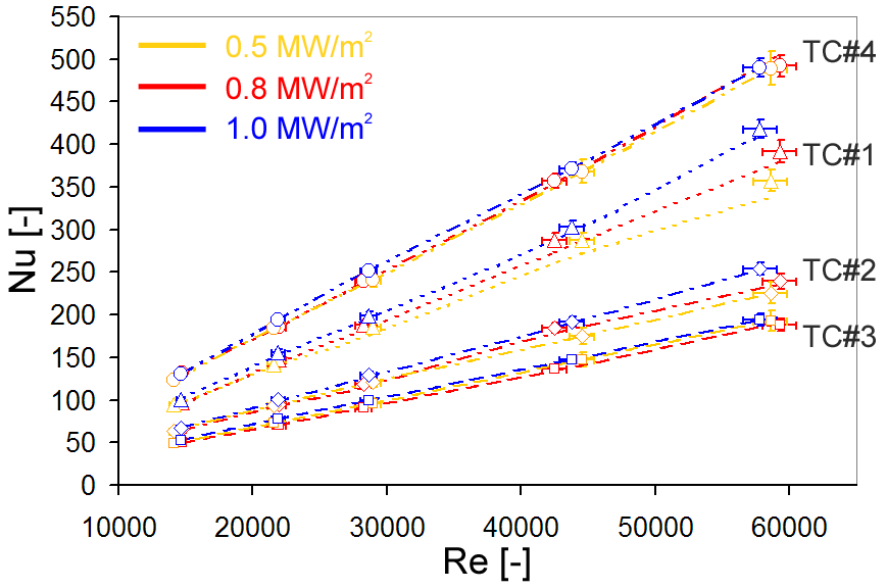

Figure 5.24: Plot Nusselt number as a function of Reynolds number obtained from experimental measurements of temperature (symbols) and numerical predictions (lines) at all four TC locations for $\theta = 0°$.

CHAPTER VI

CONCLUSIONS AND RECOMMENDATIONS

This Chapter presents the conclusions derived from this experimental and numerical investigation of various gas-cooled divertor geometries and their implications for MFE. The contributions of this work and recommendations for future work are also presented.

6.1 Conclusions

This thesis described an experimental and numerical investigation of the thermal performance of helium-cooled divertor modules proposed as the leading designs for the *ARIES* Compact Stellarator and *DEMO* studies ($T-tube$ and *HEMJ*, respectively). This research was initially motivated by the need to verify the results of preliminary design analyses that predicted heat transfer coefficients (HTC) in the order of 50 kW/(m^2·K) near the stagnation point of the T-tube design (Shin et al., 2005; Norajitra et al., 2005b). Heat transfer coefficients of this magnitude were judged to be "outside the experience base" for gas-cooled systems. Hence, experimental validation of the predicted thermal performance was deemed necessary.

Wall temperature and local HTC profiles were measured in *air-cooled* test modules that closely simulated the actual geometry of both types of He-cooled divertor modules and the thermal-hydraulic features of their jet impingement cooling technique. Experiments were performed over a wide range of parameters that match the most important dimensionless group, namely the Reynolds number, at the proposed operating conditions.

Numerical models duplicating the experimental test modules were created using the commercial CFD software package *FLUENT*®. Numerical simulations were used

to predict wall temperature and HTC distributions in the test modules for all conditions with the same methodology (i.e., *FLUENT*® code options) used by others to analyze the thermal performance of these helium-cooled divertors (Shin et al., 2005; Norajitra et al., 2005b). The experimental data validated the numerical predictions, suggesting that commercial CFD software can be used to evaluate the thermal performance of gas-cooled divertors and other plasma-facing components.

6.1.1 Experimental Results

This experimental investigation provides important results that extend and build upon previous studies of jet impingement cooling. The impingement of turbulent air jets on curved surfaces was studied for the following jet geometries and configurations:

Rectangular Jet (Slit): Rectangular jets with a slot length $L = 71$–150 mm and a large aspect ratio ($L/B \gg 1$) were studied at dimensionless jet-to-wall spacings $H/B = 1.83$ (Chapter 3) and $H/B = 2.72$ (Chapter 4). Tests were performed using air at Reynolds numbers $Re = 1,800$–$30,400$.

Single Row of Round Jets: Round jets of diameter $D = 1.0$ mm were studied at a dimensionless jet-to-wall spacing $H/D = 1.1$ and a dimensionless jet-to-jet spacing of $s/D = 3$ (Chapter 3) at Re=10,000–27,000.

Hexagonal Array of Round Jets: Round jets of diameter $D = 1.0$ mm and $D = 0.6$ mm were studied at a dimensionless jet-to-wall spacing that varied between H/D=0.9 (for the larger center hole) and H/D=1.5 (for the other smaller holes) for a triangular array with a dimensionless jet-to-jet spacing $s/D \sim 3.33$ at Re=14,100–59,300.

In agreement with previous studies, the results demonstrate that the heat transfer coefficient (HTC) is greatly enhanced (e.g., compared to a standard pipe flow) near the jet stagnation point for all these jet geometries, configurations, and jet-to-wall

spacings. The results also suggest that the maximum values of *Nu* (or HTC) are comparable at a given *Re*, regardless of the jet(s) geometry, size or configuration (Figures 3.25, 4.21 and 5.24). The spatial distribution of the local HTC, however, strongly depends on the jet(s) geometry and configuration, in particular:

- A single row of round jets offers a more uniform flow distribution than the rectangular jet, along the axial extent of the test module considered in this investigation. This results in a more uniform axial distribution of HTC (Figure 3.29).

- The heat transfer enhancement due to a single rectangular jet as well as a row of jets is *limited to the neighborhood of the jet stagnation point*, i.e., the impingement region (Figure 3.20 and 4.19).

- Hence, since jet impingement cools only near the stagnation point, multiple jets are needed to obtain a more uniform *spatial* heat transfer performance, thereby reducing the temperature gradients on the cooled surface (see results for the *HEMJ* thimble, Figure 5.14).

Three different flow configurations (i.e., coolant paths) were studied in the uniformly heated T-tube section of Chapter 3. The prototypical T-tube case investigated in Chapter 4 represents as a fourth flow configuration. Important information on the cooling performance and pressure drop in the test modules can be deduced from these results:

- Symmetric flow paths (like in the uniformly heated double inlet and prototypical T-tube modules) should be preferred since they offer an overall better performance: the local HTC is more uniform for this case along the axis of the T-tube due to smaller variations in the flow velocity, and the pressure drop across the module is smaller.

- Abrupt "detours" in the coolant path (e.g., 180° turns) deteriorate the flow distribution in the axial direction and minimize the impinging jet velocity, therefore increasing the axial HTC degradation. Furthermore, they increase the pressure drop.

- The relative position of inlet vs. outlet port(s) and the overall module length are important factors. The coolant follows the *shortest path* (i.e., the path with the least loss) between the inlet(s) and the outlet(s); any "dead end" results in a low velocity flow with lower cooling performance.

6.1.2 Numerical Results

The *FLUENT*® model predictions show reasonably good agreement with the experimental data in most cases, except for a few cases where accurate numerical models could not be built because of limitations in computational resources (Section 3.2.2). Experimental results and numerical predictions were directly compared for the:

Temperature: The surface temperature profiles calculated by *FLUENT*® showed an overall agreement with the temperatures measured in the test sections. In the T-tube cases, however, where the axial dimension of the test module if far larger than all other important geometric features (such as slit width B and annular gap H), the accurate prediction of the temperature profiles is strongly affected by the capability of the code to precisely resolve the axial flow distribution along the slit (or round jets).

Heat Transfer Coefficient (HTC): The experimental HTC was calculated using the numerically predicted local heat flux (Equation 3.5). The HTC is directly obtained from the temperature — it is not an independent quantity. The agreement between numerical and experimental values of HTC is identical to that between the numerical and experimental values of T. Although the difference

in the temperature prediction at the jet stagnation point ($\theta = 0°$) can be as small as few °C, the difference between the experimental and numerical HTC values is generally $\lesssim$ 15–20 % for the T-tube with uniform heating, $\lesssim$ 10 % for the single-sided T-tube and $\lesssim$ 3 % for the *HEMJ* geometry.

Pressure Drop: The pressure drop estimations is in best agreement with the experimental data for those computer models with the finest grid resolution. The difference between the experimental and numerical ΔP values is generally $\lesssim$ 10–25 % for the T-tube with uniform heating (row of holes and slit, respectively), $\lesssim$ 15 % for the single-sided T-tube and $\lesssim$ 12 % for the *HEMJ* geometry. It should be noted, however, that the largest discrepancy between ΔP_{exp} and ΔP_{CFD} occurs at a lower Re (i.e., mass flow rate) where the experimental pressure drop measurement has the largest relative error.

Although the computer models duplicate in detail the experimental test sections, they are a virtual representation of reality. It is unclear whether the differences between the experimentally measured and numerically calculated quantities are due to deficiencies in the CFD code/nodalization scheme or simply to "imperfections" in the test apparatuses (e.g., uniformity of slit width and annular gap along the axial extent of the test modules, temperature-induced deformations, contact resistance between surface and TC beads, etc.). The results demonstrate that model predictions and experimental results are in best agreement for the test sections manufactured with the greatest precision (single-sided T-tube and *HEMJ* tests).

The use of different k-ϵ turbulence models did not appear to significantly affect the numerical results (Figure 3.19). Detailed parametric studies on the effect of the turbulence models and wall functions were carried out by Shin et al. (2005). Nevertheless, it should be noted that treating the near-wall region with enhanced wall functions is suitable only for layered grids that are fine enough to resolve the

laminar sublayer, corresponding to a grid spacing of one wall unit y^+ (*FLUENT*®, 2004); the grid spacing in most of the numerical studies was much greater than a wall unit, typically $y^+ \gtrsim 20$–30. Hence, the use of standard wall functions was deemed to be more appropriate.

The general agreement between numerical predictions and experimental values indicates that commercial CFD codes such as *FLUENT*® can be used to evaluate proposed designs of high heat-flux gas-cooled components in MFE reactors, even for the complex geometries described here. The code predictions are of an accuracy comparable to those for typical engineering calculations (e.g., the prediction of the HTC is usually within 20 %). The modeling, however, requires adequate attention in the generation of the grid and possibly in the selection of the code options.

6.2 Implications for He-Cooled Divertors in MFE

The model predictions are in good agreement with the experimental data, providing confidence in the predicted performance of both the $T-tube$ and the *HEMJ* divertor designs. Specifically, the results confirm the validity of the high heat transfer coefficients predicted in the preliminary design calculations, and hence the ability of these divertors to accommodate incident heat flux values up to 10 MW/m^2. These models also validate the results of previous detailed parametric studies that were performed on the T-tube, namely that its design is "robust" with respect to anticipated changes in geometry and operating conditions resulting from manufacturing tolerances and/or flow mal-distribution among the modules (Shin et al., 2005).

The results collected during this investigation offer an experimental database on the thermal performance of gas-cooled divertors. In addition, this investigation could provide suggestions for the development of more efficient coolant flow geometries for gas-cooled divertors (Sections 6.2.1 and 6.2.2).

6.2.1 Suggested Modifications for the T-Tube Divertor Design

The results of this investigation can be extrapolated to suggest changes in the geometry of the proposed T-tube to enhance its thermal performance. These changes include:

Impinging Jets Geometry: As previously discussed, a series of round jets presents some advantage vs. a single rectangular jet (slit) in the thermal performance (Section 6.1.1). In addition, by using round jets rather than a slot, it could be possible to utilize a smaller mass flow rate of coolant with at least as good (if not even better) thermal performance (Section 3.3.5). This would also imply a smaller pressure drop across the T-tube module. Therefore, replacing the slot with a series of round jets might be a better way to go.

Impinging Jet(s) Configuration: The results clearly indicate that the enhancement of the cooling effect provided by the jet(s) impingement is limited to an area near the stagnation point (Section 6.1.1). Hence, two (or three) slots cut at symmetric locations with respect to the module azimuthal centerline (e.g., $\theta = \pm 20°$) forming a V (or a W) could provide a more uniform cooling performance in the azimuthal direction (Figure 6.1). If using round jets instead of the slot, the jets could be alternated along the axial direction forming a staggered pattern (Figure 6.2). Because of the *single-sided nature* of the incident heat flux, it is necessary to cover an azimuthal range $\sim 90°$; more than three slots would be unnecessary. If maintaining a dimensionless jet-to-wall spacing of H/B or $H/D \sim 2$, the optimal *azimuthal* spacing between two adjacent slots (or rows of round jets) is $\theta \approx 30°$, which corresponds to a jet-to-jet spacing $s/B = s/D = 8.0$ (the optimum value suggested by San and Lai (2001)) on an impingement surface of diameter $\phi = 15$ mm and a slot width $B = 0.5$ mm (or jets diameter $D = 0.5$ mm). Based on the same parameters, the optimal

axial spacing for the round jets is 4.0 mm. However, since in this application a uniform HTC distribution is sought (rather than an optimum value of Nu at the stagnation point), smaller jet-to-jet spacing values could be preferred.

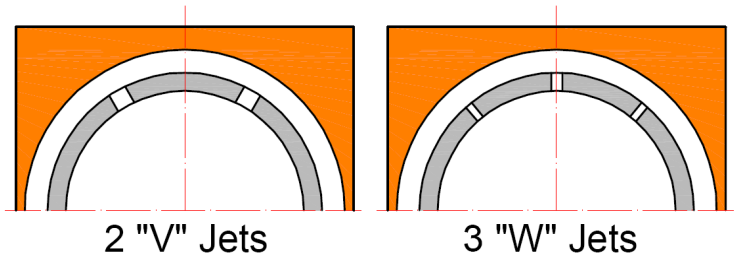

Figure 6.1: Suggested azimuthal slot (or round jets) distribution.

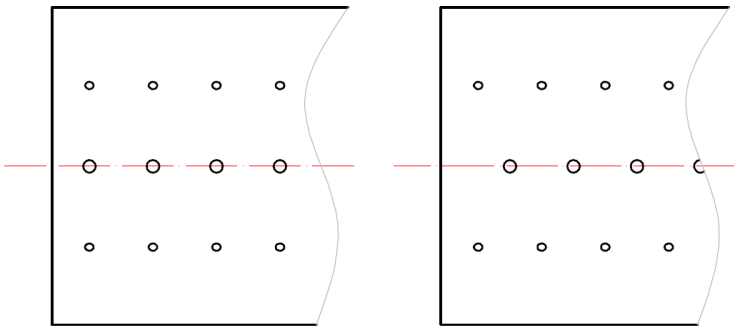

Figure 6.2: Suggested axial configuration of the round jets. Preferred staggered layout is shown on the right.

Overall Size: By using more than one slot it could be possible to increase the *diameter* of the inner tube and therefore enlarge the *width* of the cartridge, because of the improved *azimuthal* cooling performance. Furthermore, when replacing the slot with a row of holes it could be possible to increase the *length* of the cartridge because of the improved *axial* cooling performance. The overall improved thermal performance (i.e., the more uniform HTC spatial distribution) would limit the temperature gradients in the tungsten armor, thereby reducing the thermal stresses. Larger size modules could be used, reducing the number of components required and therefore the complexity and the cost of the divertor.

Coolant Ports Location: As noted in Section 6.1.1, the coolant flows along the shortest path between the inlet(s) and the outlet(s). By increasing the distance between the outlet and the inlet coolant ports it may be possible to achieve a better *axial* flow distribution. This may avoid overheating of the module ends, thereby allowing a higher incident heat flux without exceeding the thermal limits dictated by material properties.

6.2.2 Suggested Modifications for the HEMJ Divertor Design

The quasi-uniform temperature distribution on the cooled surface of the thimble (Figure 5.14) suggests that the size of the "finger" *HEMJ* module could be increased without affecting the thermal performance (and therefore without affecting the thermal stresses in the tungsten armor). As indicated earlier, the use of larger modules would require a smaller number of components, reducing complexity and cost of the divertor.

In addition, the jet-to-jet spacing could be changed; according the the results reported in the literature (Section 2.1.4), a peak in Nu at the jet stagnation point is achieved with a jet-to-jet spacing $s/D \approx 8$ (for a jet-to-wall spacing $H/D = 2$). Currently, the jet-to-jet spacing is $s/D = 3.33$ (and a jet-to-wall spacing $H/D = 1.5$). By increasing the jet-to-jet spacing (and therefore reducing the number of jets), it could be possible to reduce the coolant mass flow rate (and hence the pressure drop) with at least as good, if not improved, cooling performance.

6.3 Contributions

The results of this investigation contribute to the general understanding of the thermal-hydraulic performance of gas cooling through jet impingement. Additionally, computer models have been experimentally validated, providing confidence that commercially available CFD codes such as *FLUENT*® can be utilized to analyze flows in complex geometries.

Fusion energy, despite its technical challenges, has the potential to be a major energy source free of greenhouse gases. Developing divertors that can withstand the extreme heat fluxes and temperature gradients typical of tokamak plasmas is required to maintain the purity of the plasma for long-term operation of magnetic fusion energy (MFE) reactors. This research will therefore contribute to robust and reliable design of a critical component in MFE power plants.

The experimental results obtained with these test modules will establish a design database that will be useful for designers of MFE power plants. Specifically, these data will be used to validate numerical models for predicting the thermal-hydraulic behavior of helium-cooled divertors. These numerical models, implemented in commercially available software, will in turn be used to evaluate and improve the performance of gas-cooled high heat-flux plasma-facing components, thereby improving the long-term performance of MFE reactor designs.

6.4 Recommendations and Future Work

The *experimental* investigation could be improved/extended by:

- The construction of test modules duplicating other proposed divertor geometries (such as the so called "plate" design of Hermsmeyer and Malang (2002)).
- Tests performed using helium as the coolant. This would eliminate any argument about the influence of Pr on the calculation of Nu.
- Tests performed with higher heat fluxes, which may require modification of the test modules or the design of new ones.
- Using calibrated thermocouples. The calibration of each individual thermocouple, rather than reliance on the generally conservative error estimates provided by the manufacturer, would decrease the error in the calculation of the heat transfer coefficient.

- Direct measurement of the pressure drop across the test section with a *differential* pressure transducer rather than calculating ΔP through the difference between the inlet and exit pressure would improve the measurement accuracy.

- Obtaining the coolant mass flow rate measurement with more accurate instrumentation.

The *numerical* investigation could be improved/extended by:

- Supporting the purely thermal-hydraulic calculations with structural analyses, using finite elements software such as *ANSYS*®, *ALGOR*® and others.

- Comparing the results obtained using other commercially available CFD codes (e.g., *CFX*®, *STAR − CD*®, etc.).

- Performing calculations with improved (in quality and spatial resolution) grids.

APPENDIX A

ERROR ANALYSIS

This appendix summarizes the methods used to quantify the uncertainties in the experimental measurements. The total uncertainty was based on the uncertainty due to fluctuations in the measurements and the uncertainty in the instrumentation (usually quoted by the manufacturer). An error propagation formula (Equation A.1) was used to determine the uncertainty for derived quantities.

$$U_x(i, j \ldots, n) = \sqrt{U_i^2\left(\frac{\partial U_i}{\partial i}\right)^2 + U_j^2\left(\frac{\partial U_j}{\partial j}\right)^2 + \cdots + U_n^2\left(\frac{\partial U_n}{\partial n}\right)^2} \tag{A.1}$$

Here x is the derived quantity (e.g., heat flux, Nusselt number, etc.) and i, j, $\ldots n$ are the measured quantities (e.g., temperature, slot width, etc.). Unless stated otherwise, all of the statistical uncertainties were calculated assuming that the samples had a Gaussian distribution, corresponding to $k_c = 2.0$ for 95 % confidence intervals. The error propagation contribution to the total uncertainty did not include covariance terms (Equation A.2).

$$U_{total} = \sqrt{U_A^2 + U_B^2} \tag{A.2}$$

A.1 Mass Flow Rate Uncertainty

For the uncertainty in the mass flow rate measurement, the instrumental uncertainty and the statistical uncertainty due to experimental fluctuations were considered. The positive displacement gas flow meter used to either directly measure or calibrate the orifice, had a minimum resolution of 0.05 ft^3. This corresponds to a relative instrumental uncertainty of ± 1.25 % on a typical measurement of 4 ft^3 (neglecting uncertainties in the measurement of time and coolant density). The standard deviation in the mass flow rate due to experimental fluctuations was found to be 0.022 g/s based

on four independent flow rate measurements under identical conditions 3.09, 3.08, 3.04 and 3.08 g/s. Based on Student's t-distribution for three degrees of freedom, k_c should be 3.2 for 95 % of the measurements to fall within the total uncertainty. The 95 % confidence intervals for the mass flow rate measurements is therefore 0.0704 g/s. Thus, the relative error in the mass flow rate measurement (based on the mean of the four samples) due to experimental fluctuation is ±2.29 %. The combination of the instrumental and statistical uncertainties then gives a total relative uncertainty $U_{\dot{m}} = \pm 2.61$ %; this value was assumed to be the relative uncertainty over the entire range of mass flow rates considered here.

A.2 Temperature Uncertainty

The total uncertainty in the thermocouple reading was derived from the manufacturer-given uncertainty of ±1.5 °C and the statistical experimental fluctuations. The statistical fluctuations were determined from 75 temperature samples obtained over 6.25 min under steady-state conditions as defined in Section 3.1.5. The total uncertainty in the temperature measurements then ranged from 1.6 °C to 1.9 °C.

A.3 Heat Transfer Coefficient Uncertainty

The total uncertainty in the heat transfer coefficient (HTC) was found by using the error propagation formula (Equation A.3), and the uncertainties of the surface temperature, inlet temperature, and heat flux.

$$U_{HTC} = \sqrt{U_{q''}^2 \frac{1}{(T_w - T_{in})^2} + U_{T_w}^2 \frac{q''^2}{(T_w - T_{in})^4} + U_{T_{in}}^2 \frac{q''^2}{(T_w - T_{in})^4}} \qquad \text{(A.3)}$$

The temperature uncertainties were computed in the previous Section. The heat flux uncertainty is due to the manner it was obtained from *FLUENT*®. The value of the local heat flux was read by clicking (inquiring) at the desired location on the jet impingement surface; a range of heat flux values was returned for each face mesh element. The full scale in *FLUENT*® was divided into 40 intervals which results in

a ±1.25 % relative uncertainty of the heat flux. The total uncertainty of the flux, $U^2_{q''}$, was determined by multiplying the recorded heat flux value by the relative uncertainty. The total uncertainty in the HTC for the T-tube experiment with uniform heating (Chapter 3) ranges from ±1.5 % to ±7.4 % corresponding to $\theta = 180°$ and $\theta = 0°$, respectively. The total uncertainty in the HTC for the single-sided T-tube experiment (Chapter 4) varies between ±2.7 % and ±3.0 %. The total uncertainty in the HTC for the HEMJ experiment (Chapter 5) is ±1.8 % to ±5.5 % depending on experimental conditions and azimuthal location.

A.4 Nusselt Number Uncertainty

The uncertainty for the Nusselt number can then be calculated from the uncertainties in the local HTC and those in either the measurement of the jet diameter or the slit hydraulic diameter, depending on the geometry (Equation A.4).

$$U_{Nu} = \sqrt{U^2_{HTC}\left(\frac{D_h}{k}\right)^2 + U^2_{D_h}\left(\frac{h}{k}\right)^2} \tag{A.4}$$

The uncertainty in the measurement of the slit width is $U_B = \pm 0.1$ mm, while that of the round jets diameter is $U_B = \pm 0.05$ mm (based on standard machining tolerances). The relative uncertainty of the Nusselt number was $U_{Nu} \approx 5.3$ % for the round jets and 8.9 % to 11.3 % for the slits.

A.5 Incident Heat Flux Uncertainty

The uncertainty in the incident heat flux is based on the TC with the greatest spacing in the "neck" region of the copper concentrator, as shown in Equation A.5 (only for the single-sided T-tube and the HEMJ test modules).

$$q''_{measured} = k\frac{T_z - T_x}{\Delta_{zx}} \tag{A.5}$$

The total uncertainty was calculated by determining the error propagation formula for the heat flux (Equation A.6), and the uncertainties of temperature measurements

(U_T) and TC beads spacing ($U_{\Delta_{zx}}$).

$$U_{q''} = \sqrt{\left(\frac{k}{\Delta_{zx}}\right)^2 (U_{T_z}^2 + U_{T_x}^2) + U_{\Delta_{zx}}^2 \left(\frac{q''}{\Delta_{zx}}\right)} \tag{A.6}$$

The uncertainty in the spacing between neighboring beads is $U_{\Delta_{zx}} = \pm 0.1$ mm, based on an uncertainty of ±0.05 mm in the position of each TC bead. The uncertainty in the incident heat flux values are given in Table A.1 because the values vary greatly with the magnitude of the heat flux. The rather high uncertainties at the low heat flux values are due to the high relative uncertainty in the measurement of the small temperature drop in the copper "neck".

Table A.1: Relative uncertainty in the measurement of the incident heat flux.

Test Module	q'' [MW/m^2]	**Relative Error** [%]
T-tube	0.1	88
	0.28	31
	0.55	16
	0.81	11
HEMJ	0.45	18
	0.72	11
	0.90	9

A.6 Power Input Uncertainty

The uncertainty in the power input was determined by considering the statistical uncertainty due to experimental fluctuations and the manufacturer stated uncertainties in our measurements of voltage V and current I. The statistical uncertainty was found by first calculating a sample standard deviation for 75 samples of voltage (over 6.25 min) and ten samples of current (over the same period of time) recorded under steady state. The experimental fluctuations was found to be ±0.05 % for the voltage and ±0.68 % for the current. The total uncertainty due to experimental fluctuations was then ±0.69 % (Equation A.7).

$$U_{Power} = \sqrt{U_V^2 I^2 + U_I^2 V^2} \tag{A.7}$$

The manufacturers' stated accuracy for the Agilent Data Acquisition unit is 0.01 % and the Fluke 25 digital multimeter is 0.75 %. The calculated total instrumental uncertainty was ±0.75 %. Based on the instrumental and statistical uncertainties, the overall relative uncertainty in the power input measurement is estimated to be about ±1.2 %.

A.7 Pressure Drop Uncertainty

The uncertainty in the pressure drop was determined by considering statistical fluctuations in the inlet and outlet pressures during operation of the test section as well as uncertainties in the instrumentation. The total statistical uncertainty was determined by using the error propagation formula for the pressure drop (Equation A.8).

$$U_{\Delta P} = \sqrt{U_{P_{in}}^2 + U_{P_{out}}^2} \tag{A.8}$$

The *OMEGA*® pressure transducers have an accuracy, according to the manufacturer, of 0.75 % of the full scale; the Ashcroft pressure gauge could be read within 0.5 psi. The instrumentation uncertainties were computed for the experimental pressure readings. Then the total instrumentation uncertainty was calculated with the error propagation formula for the pressure drop (Equation A.8). Finally the total uncertainty in the pressure drop was calculated by taking the root-mean-squared value of the total instrumental and statistical uncertainties. The total uncertainty is $U_{\Delta P} \approx 1.4$ psi for the *HEMJ* test module (which used an analog pressure gauge) and $U_{\Delta P} \approx 0.6$ psi for the T-tube test modules (which used digital pressure gauges). This absolute uncertainty of course gives very large relative uncertainties in the pressure drop measurement for the low mass flow rate cases which have a very small pressure drop (Table A.2).

Table A.2: Relative uncertainty in the measurement of the pressure drop across the test section.

Test Module	ΔP [psi]	Relative Error [%]
T-tube	0.99	64.3
	3.09	20.6
	6.71	9.5
	16.76	3.8
HEMJ	1.7	84.2
	3.5	40.6
	5.1	27.6
	12.6	10.9
	24.1	5.5

A.8 Thermocouple Location Uncertainty

The thermocouples used in the uniformly heated test section (Chapter 3) had a bead size of $\sim$ 1 mm, corresponding to an angle of 7.2° (based on the outer tube OD ϕ = 15.9 mm). The angular scale used for the positioning of the inner tube with respect to the outer tube had a resolution of 2.5°. The alignment of the nine TCs at the "zero" position therefore also had an uncertainty of 2.5°, giving a total uncertainty in the azimuthal position $U_\theta = \pm 4.0^\circ$.

The thermocouples used in the single-sided heated test section (Chapter 4) had a bead diameter of $\sim$ 0.5 mm. This corresponds to an angle of 4.8° (based on the $\phi = 12.0$ mm cavity), giving an overall uncertainty $U_\theta = \pm 2.4^\circ$.

The thermocouples used in the HEMJ test section (Chapter 5) had a bead diameter of $\sim$ 0.5 mm. Because of the different radial positions of the four TCs, the measurements obtained by *TC*#1, *TC*#2, and *TC*#3 span 4.5°, 6.7°, and 13.6°, respectively. There is no uncertainty in azimuthal position associated with *TC*#4, which is located at the center of the thimble.

APPENDIX B

UNIFORMLY HEATED T-TUBE EXPERIMENTAL AND NUMERICAL DATA

This appendix tabulates the range of experimental and numerical parameters for all the tests performed on the T-tube apparatus with uniform azimuthal heating. Table B.1 lists and describes the symbols used in the following tables.

Table B.1: List and description of the experimental symbols.

Type	Units	Symbol	Description
Temperature	°C	T_{in}	Air Inlet temperature
		T_{outA}	Air outlet temperature at port "A" — double inlet arrangement (Figure 3.8)
		T_{outB}	Air outlet temperature at port "B" — double inlet arrangement (Figure 3.8)
		T_{out}	Outlet temperature — counter and parallel flow arrangement
		T_x	Temperature at instrumented axial location #x
Heat Flux	kW/m^2	HF_x	Numerical heat flux at axial location #x
		HF_{avg}	Average numerical heat flux at fixed θ
Pressure	psi	P_{in}	Inlet gauge pressure
		P_{out}	Outlet gauge pressure

Each table refers to the corresponding experiment number listed in Tables 3.2 and 3.4. Experiments #$TS4$ and #$TS6$ were directly vented into the atmosphere, so the outlet pressure is ambient; the outlet pressure P_{out} is therefore not given for these cases. In the case of the row of holes, the numerical results are tabulated only for experiments #$TH1$, #$TH2$ and #$TH3$ (see Section 3.2.2). As indicated in Section 3.3.4, the average numerical surface heat flux along a line at fixed θ was used, for this case, in the calculation of the HTCs.

Table B.2: Experimental results for test #$TS1$.

θ	T_{in}	T_{outA}	T_{outB}	T_1	T_2	T_3	T_4	T_5	T_6	T_7	T_8	T_9	P_{in}	P_{out}
[°]	[°C]												[psi]	
0	21.2	43.4	45.5	57.3	69.1	89.7	97.7	98.7	91.0	84.2	67.5	59.2	15.9	14.3
20	21.0	43.1	45.5	60.9	76.5	91.2	98.6	100.7	95.8	86.9	72.5	66.8	15.8	14.2
40	20.8	43.9	45.3	73.8	85.1	98.4	107.9	110.5	102.9	96.5	86.2	77.0	15.9	14.1
60	20.8	43.8	45.6	84.9	95.0	111.3	118.7	119.8	114.1	111.3	98.4	89.7	15.7	14.0
80	20.7	43.8	45.7	94.9	109.7	123.4	129.4	131.1	128.6	122.8	111.0	97.9	15.8	14.1
100	20.6	43.7	45.6	109.3	122.1	134.4	140.5	144.3	140.5	131.1	118.5	108.9	15.9	14.1
120	20.9	43.3	45.9	120.6	133.1	144.8	153.0	154.6	145.9	138.0	128.3	118.6	15.8	14.0
140	21.8	43.8	46.3	129.3	143.6	156.8	161.6	156.5	151.7	145.2	136.4	126.0	15.8	14.0
160	22.9	45.2	47.8	136.8	154.7	163.0	160.9	161.2	156.6	150.1	141.1	132.5	15.7	14.1
180	23.8	46.2	48.6	143.1	157.6	159.8	163.8	163.4	158.3	151.3	143.7	131.6	15.8	14.2
200	23.4	45.6	48.3	140.0	150.9	160.2	163.1	161.6	156.1	148.9	139.2	126.5	15.7	14.1
220	22.5	44.2	47.5	130.1	147.9	156.2	158.4	156.5	149.6	142.1	131.3	121.0	15.7	14.1
240	22.1	44.2	47.1	123.9	140.1	148.6	150.7	146.7	141.2	133.0	124.2	118.7	15.7	14.1
260	21.8	44.2	46.7	113.7	128.7	138.2	138.9	137.6	130.7	125.0	122.3	109.2	15.8	14.1
280	21.6	43.9	46.5	101.5	115.2	124.1	128.6	126.9	120.9	124.5	111.2	98.5	15.7	14.1
300	21.5	43.9	46.1	88.0	99.0	112.6	117.3	116.9	122.1	113.2	99.7	84.6	15.8	14.2
320	21.3	43.5	46.0	73.4	86.3	100.3	107.0	116.7	110.2	102.3	85.0	73.2	15.8	14.2
340	21.2	43.6	45.8	63.0	75.1	89.9	105.0	106.2	99.3	89.9	74.8	62.4	15.8	14.2
360	21.2	43.4	45.5	57.3	69.1	89.7	97.7	98.7	91.0	84.2	67.5	59.2	15.9	14.3

Table B.3: Experimental results for test #*TS*2.

θ	T_{in}	T_{outA}	T_{outB}	T_1	T_2	T_3	T_4	T_5	T_6	T_7	T_8	T_9	P_{in}	P_{out}
[°]	[°C]												[psi]	
0	21.6	37.7	41.0	55.1	62.1	75.1	79.4	82.0	77.2	74.2	61.6	55.1	30.2	25.3
20	21.5	37.8	40.7	58.8	67.1	82.9	87.9	90.1	82.6	79.7	66.7	59.5	30.2	25.3
40	21.3	38.4	40.2	69.7	80.5	99.7	105.7	106.7	97.0	93.8	78.2	69.1	30.1	25.4
60	21.0	38.7	39.2	84.8	97.5	117.6	123.4	123.5	112.3	107.5	91.9	81.0	30.1	25.4
80	21.1	38.8	39.2	100.8	114.0	132.9	137.1	137.1	128.0	123.0	109.2	96.3	30.1	25.4
100	21.2	38.7	39.3	114.6	129.3	145.7	150.2	150.7	144.7	138.1	130.1	116.5	30.1	25.4
120	21.0	38.4	39.3	130.7	144.6	158.5	162.6	163.3	159.4	152.2	145.6	133.3	30.1	25.3
140	21.4	38.9	39.6	150.5	162.1	172.3	176.0	177.5	174.3	166.7	159.4	148.0	30.2	25.4
160	21.7	39.5	39.7	164.8	174.4	182.5	185.4	186.1	183.1	176.0	168.9	159.2	30.1	25.5
180	21.9	39.8	39.9	168.2	178.3	185.7	187.6	188.1	187.3	181.7	174.9	165.7	30.1	25.4
200	21.7	39.1	40.1	157.6	169.5	179.0	181.2	180.8	180.9	177.1	169.6	159.1	30.2	25.2
220	21.4	38.7	39.8	144.8	158.3	171.1	173.7	173.0	172.2	167.7	158.1	146.0	30.3	25.0
240	21.1	38.8	39.4	132.8	147.9	162.3	165.3	166.4	164.6	158.8	147.6	134.1	30.2	25.2
260	21.0	38.8	39.1	117.2	133.1	149.8	153.3	154.5	149.3	142.3	131.5	116.1	30.2	25.3
280	21.1	38.7	39.1	102.4	117.9	136.5	139.6	140.7	135.6	129.8	117.0	100.6	30.1	25.2
300	21.1	38.4	39.5	85.4	97.8	118.2	122.4	124.3	120.3	117.8	101.3	86.3	30.2	25.2
320	21.0	38.0	39.5	70.1	81.7	102.5	105.8	107.1	102.6	101.8	84.4	71.9	30.2	25.2
340	21.4	38.6	39.8	62.0	72.1	89.7	93.1	94.4	89.8	87.6	71.4	61.4	30.1	25.2
360	21.7	39.2	39.8	58.5	67.1	81.1	86.5	87.0	81.1	76.4	62.8	55.1	30.1	25.3

Table B.4: Experimental results for test #$TS3$.

θ	T_{in}	T_{outA}	T_{outB}	T_1	T_2	T_3	T_4	T_5	T_6	T_7	T_8	T_9	P_{in}	P_{out}
[°]	[°C]												[psi]	
0	18.5	36.0	39.1	57.8	64.8	77.8	80.7	85.3	81.7	74.6	64.8	57.5	33.9	4.1
20	18.6	36.7	39.4	62.9	71.3	91.1	92.9	98.3	91.0	83.1	71.1	62.2	33.3	4.0
40	18.7	36.2	38.2	75.0	83.9	106.4	109.5	114.9	106.1	99.6	84.1	73.5	34.1	4.1
60	18.7	36.6	39.0	88.4	98.4	119.1	124.4	129.6	121.1	115.4	99.3	86.0	33.6	4.0
80	18.8	36.1	38.3	101.4	112.9	130.7	138.1	142.2	133.9	129.2	114.8	99.1	34.9	4.2
100	18.7	36.7	38.9	119.8	133.0	150.0	157.9	160.8	152.5	147.4	136.0	118.2	34.3	4.1
120	18.8	37.2	39.2	140.5	153.5	169.8	177.4	178.3	170.2	164.4	156.1	138.5	33.8	4.0
140	18.9	37.2	39.2	158.0	170.6	185.4	192.4	189.9	182.0	175.9	170.0	156.4	33.8	4.0
160	19.0	37.5	39.6	177.0	189.4	201.2	207.0	202.5	196.4	190.7	184.8	173.0	33.5	4.0
180	18.6	36.5	38.7	171.0	184.6	197.0	201.6	197.1	193.2	189.0	182.3	169.5	34.2	4.1
200	18.7	36.7	39.0	159.3	173.3	188.0	194.4	192.3	189.6	185.5	176.7	161.9	34.0	4.1
220	18.8	36.8	39.6	141.5	156.5	172.3	181.4	184.8	182.7	176.5	166.4	151.5	33.7	4.0
240	18.8	37.0	39.3	129.9	144.4	159.4	169.4	173.2	173.2	165.6	153.1	135.0	33.8	4.0
260	18.6	36.2	38.4	110.5	126.8	143.8	154.4	158.1	154.1	150.4	135.9	116.6	34.2	4.1
280	18.7	36.6	38.8	96.8	111.6	130.6	139.9	144.5	140.5	137.4	119.8	101.4	34.0	4.1
300	18.7	36.6	38.9	81.0	93.6	115.5	120.6	125.6	122.1	119.8	99.7	83.0	34.3	4.2
320	18.8	36.9	39.0	68.5	79.9	102.7	104.5	109.6	106.6	103.7	83.6	69.5	34.2	4.2
340	18.8	37.0	39.2	61.5	70.6	88.1	89.9	94.9	92.0	86.8	71.6	61.8	33.8	4.1
360	18.8	37.1	39.1	59.5	67.0	80.9	83.7	88.5	84.3	76.8	66.4	58.5	33.5	4.1

Table B.5: Experimental results for test #$TS4$.

θ	T_{in}	T_{out}	T_1	T_2	T_3	T_4	T_5	T_6	T_7	T_8	T_9	P_{in}
[°]	[°C]											[psi]
0	20.3	30.0	31.5	36.0	42.8	49.7	61.6	79.7	101.4	113.3	108.4	4.3
20	20.4	30.2	32.7	36.4	43.4	50.4	62.9	82.6	105.0	114.7	109.7	4.3
40	21.5	31.2	35.5	40.0	48.0	55.8	70.4	90.4	111.5	120.4	114.0	4.2
60	21.1	30.7	40.2	45.8	54.4	64.5	79.6	99.4	118.9	127.0	118.5	4.1
80	20.9	30.6	46.0	52.6	62.9	73.6	89.1	108.7	126.9	133.6	121.5	4.1
100	20.8	30.5	52.8	61.1	71.7	83.0	98.8	118.3	134.5	138.2	124.8	4.1
120	20.6	30.3	61.4	69.9	80.8	92.2	108.7	127.1	139.8	143.0	127.9	4.3
140	20.5	30.0	70.0	78.7	89.6	101.5	117.7	133.1	144.9	147.4	129.7	4.3
160	20.4	30.0	77.4	86.8	97.9	109.4	123.4	138.2	149.0	149.7	131.4	4.4
180	20.4	30.0	81.7	92.5	102.9	113.2	127.2	141.4	150.5	151.8	132.0	4.4
200	20.4	29.8	79.7	92.0	102.4	113.4	127.5	140.8	151.0	151.8	132.5	4.6
220	20.4	29.8	73.0	86.4	97.3	108.9	122.8	138.0	148.6	149.8	130.4	4.6
240	20.4	29.6	65.5	77.8	88.9	100.2	115.5	131.4	145.0	148.5	130.1	4.5
260	20.4	29.7	57.0	68.3	78.6	90.5	105.2	123.5	139.4	144.6	128.1	4.6
280	20.3	29.9	49.2	58.6	68.9	79.8	95.1	114.5	131.9	139.1	125.4	4.6
300	20.2	29.9	42.3	50.5	59.5	70.2	85.5	104.2	123.7	132.5	121.1	4.6
320	20.2	29.9	36.5	43.3	52.0	62.3	75.6	94.4	115.3	124.7	116.5	4.5
340	21.4	30.9	32.3	37.8	47.0	54.6	67.3	85.6	106.7	117.6	112.3	4.4
360	22.1	31.5	30.0	36.0	42.8	49.7	61.6	79.7	101.4	113.3	108.4	4.4

Table B.6: Experimental results for test #$TS5$.

θ	T_{in}	T_{out}	T_1	T_2	T_3	T_4	T_5	T_6	T_7	T_8	T_9	P_{in}	P_{out}
[°]	[°C]											[psi]	
0	20.4	26.8	27.7	29.5	32.7	35.5	41.6	51.3	65.4	72.4	80.0	34.3	4.3
20	20.7	27.1	28.8	30.9	35.1	38.5	45.4	54.9	69.1	78.6	87.7	34.9	4.4
40	20.9	27.3	31.3	33.9	39.4	43.8	52.2	63.1	78.1	89.3	98.7	35.0	4.4
60	21.0	27.6	34.8	38.4	44.5	51.0	61.2	73.9	89.6	102.4	110.6	35.1	4.4
80	21.0	27.9	39.5	44.3	51.8	60.3	72.1	86.3	102.4	115.6	122.2	35.1	4.4
100	21.0	27.8	44.2	50.9	59.9	70.2	83.8	99.5	115.6	128.3	132.3	35.1	4.4
120	20.9	27.8	50.7	59.6	70.3	82.0	96.7	112.3	127.1	138.7	140.3	35.0	4.4
140	20.6	27.7	57.9	68.7	80.3	92.3	106.8	121.8	135.1	145.2	145.1	35.0	4.4
160	20.6	27.6	68.0	78.9	90.1	101.8	115.4	129.3	141.4	150.2	149.3	35.1	4.4
180	20.5	27.4	70.0	81.4	92.4	103.6	116.8	131.2	142.9	151.0	150.3	35.0	4.4
200	20.4	27.4	62.0	74.3	86.1	97.7	111.7	127.9	140.5	148.8	149.5	35.0	4.4
220	20.4	27.3	53.3	64.4	75.5	86.6	100.9	118.8	132.8	141.6	144.5	34.9	4.4
240	20.3	27.2	46.7	55.5	65.5	75.4	89.1	108.1	123.5	132.5	137.3	35.0	4.4
260	20.3	27.2	41.3	48.0	56.5	65.6	78.6	97.8	115.0	124.8	131.0	35.0	4.4
280	20.4	27.2	37.3	42.3	49.4	57.0	68.6	86.7	104.6	114.5	122.2	35.0	4.4
300	20.2	27.1	33.2	37.2	43.2	48.7	58.1	73.8	91.2	100.0	109.3	34.9	4.4
320	20.3	27.1	30.3	33.3	38.5	42.3	49.9	63.2	79.9	87.5	97.6	34.8	4.4
340	20.1	27.0	28.1	30.3	34.1	36.9	42.8	53.3	67.7	74.0	84.2	34.7	4.4
360	20.1	27.0	27.5	29.3	32.5	35.3	40.7	49.3	61.8	68.8	79.0	34.7	4.4

Table B.7: Experimental results for test #*TS*6.

θ	T_{in}	T_{out}	T_1	T_2	T_3	T_4	T_5	T_6	T_7	T_8	T_9	P_{in}
[°]	[°C]											[psi]
0	22.6	45.9	125.1	132.1	130.2	125.6	110.0	91.4	76.0	64.0	53.6	1.2
20	23.3	47.0	127.1	134.0	128.7	124.9	110.4	92.8	79.4	66.2	56.8	1.2
40	23.7	48.0	140.6	143.4	138.1	134.5	120.7	103.5	87.5	75.7	65.2	1.3
60	22.6	47.1	153.0	156.4	150.8	146.3	135.1	114.2	100.0	88.0	76.2	1.3
80	21.5	46.3	165.0	170.8	164.0	159.3	146.0	128.6	114.0	101.3	87.6	1.3
100	21.2	46.1	175.0	183.8	177.0	167.3	158.5	143.0	128.0	114.0	100.0	1.2
120	21.0	45.7	181.7	195.7	183.9	176.7	169.3	155.5	140.7	126.8	111.3	1.2
140	20.9	45.5	187.6	201.0	192.4	184.8	176.9	165.1	152.0	137.2	122.4	1.2
160	20.7	45.1	188.9	207.3	199.2	189.9	182.6	172.2	159.0	146.4	131.1	1.1
180	20.6	45.0	190.7	211.1	202.5	193.2	186.0	175.2	163.8	150.8	135.0	1.1
200	20.5	44.8	191.0	211.1	203.0	193.0	185.2	176.0	162.7	149.4	134.6	1.1
220	20.3	44.6	188.9	208.6	199.2	188.8	183.1	171.6	156.5	146.6	129.6	1.1
240	20.2	44.5	185.4	202.1	191.3	184.0	176.8	163.2	150.3	136.0	119.9	1.1
260	20.2	44.4	179.1	191.7	183.2	176.0	167.7	156.0	137.4	124.4	106.9	1.1
280	20.1	44.4	170.0	180.5	172.5	165.8	157.1	142.0	124.4	110.2	93.5	1.2
300	20.1	44.5	160.0	167.1	160.5	155.0	147.0	128.4	109.4	96.1	80.6	1.2
320	20.9	45.0	147.7	153.0	151.8	145.9	134.1	113.1	95.4	82.7	68.0	1.3
340	22.4	46.1	134.8	140.7	138.4	136.1	120.2	100.3	83.8	70.8	58.4	1.3
360	23.1	47.1	126.0	132.1	130.2	125.6	110.0	91.4	76.0	64.0	53.6	1.3

Table B.8: Experimental results for test #*TS7*.

θ	T_{in}	T_{out}	T_1	T_2	T_3	T_4	T_5	T_6	T_7	T_8	T_9	P_{in}	P_{out}
[°]	[°C]											[psi]	
0	20.9	29.1	33.6	37.0	39.8	45.0	49.8	53.2	53.7	61.3	79.3	40.8	25.3
20	20.9	29.2	34.9	38.6	42.2	47.9	52.9	55.4	56.1	67.5	91.6	40.8	25.2
40	21.0	29.4	37.9	42.5	47.8	54.0	60.1	62.6	65.1	82.2	115.1	40.8	25.1
60	21.1	29.5	42.9	48.8	55.4	63.0	69.9	71.6	77.1	101.8	143.2	40.8	25.1
80	21.5	30.2	49.4	56.7	64.9	73.8	80.6	81.8	90.1	120.8	162.7	40.8	25.1
100	21.8	30.6	56.7	65.6	75.6	85.0	90.6	91.1	98.5	129.5	164.5	40.8	25.1
120	21.3	30.2	64.3	74.0	84.1	92.5	96.5	97.1	103.9	132.6	162.9	40.8	25.1
140	21.3	30.3	72.5	82.2	91.6	98.4	101.0	102.3	110.7	137.6	163.7	40.8	25.1
160	21.1	30.0	78.7	88.3	97.0	102.4	104.7	106.7	116.4	141.4	165.0	40.8	25.1
180	21.0	29.9	81.6	91.1	99.3	104.2	106.6	109.9	122.0	150.9	177.4	40.8	25.1
200	20.9	29.8	78.9	89.1	97.9	103.1	105.7	109.8	123.7	156.0	184.0	40.8	25.0
220	21.0	30.1	72.7	84.2	94.4	101.3	104.2	109.6	126.6	167.2	195.0	40.8	25.1
240	21.7	30.6	63.7	74.3	84.8	93.1	97.1	103.0	120.7	161.1	191.6	40.8	25.1
260	21.9	30.7	57.1	66.4	75.8	84.6	89.8	94.9	109.7	138.2	167.4	40.7	25.1
280	22.0	30.9	51.6	59.6	67.8	76.2	82.8	87.4	100.0	125.0	156.6	40.8	25.1
300	21.6	30.5	45.5	52.3	59.1	66.5	73.5	78.2	87.3	108.0	141.0	40.8	25.1
320	21.3	30.2	40.2	45.6	51.2	57.4	63.7	69.1	74.2	89.0	116.4	40.7	25.2
340	21.3	30.1	37.0	41.3	45.4	51.1	56.4	61.2	63.9	74.3	96.2	40.7	25.2
360	21.3	30.2	35.2	38.8	41.8	47.4	52.0	55.8	56.7	65.3	82.7	40.8	25.3

Table B.9: Experimental results for test #*TH*1.

θ	T_{in}	T_{outA}	T_{outB}	T_1	T_2	T_3	T_4	T_5	T_6	T_7	T_8	T_9	P_{in}	P_{out}
[°]	[°C]												[psi]	
0	23.0	45.6	42.1	46.6	45.3	45.5	46.3	47.2	48.2	48.1	47.1	46.4	60.1	58.7
20	23.1	45.7	42.2	53.2	51.2	51.7	53.2	53.6	52.6	51.3	53.6	51.8	60.0	58.7
40	23.1	46.2	42.6	67.2	64.6	65.2	67.0	66.7	64.5	62.7	66.3	65.1	60.1	58.8
60	23.2	46.9	43.0	81.9	78.8	79.3	80.9	79.9	76.9	75.0	79.9	79.1	60.1	58.8
80	23.4	47.2	43.3	96.9	94.1	94.5	95.3	93.6	90.1	88.8	94.7	94.0	60.1	58.8
100	23.5	47.5	43.8	111.2	109.2	109.4	109.6	107.3	103.9	103.4	109.5	109.0	60.1	58.8
120	23.6	47.8	44.1	123.4	122.2	122.5	122.6	120.4	116.7	115.7	120.5	120.3	60.0	58.7
140	23.7	48.5	44.3	135.8	135.2	135.5	135.8	134.2	131.1	129.1	131.7	132.0	60.0	58.7
160	23.7	48.2	44.1	133.5	132.9	133.3	133.6	132.1	129.1	126.9	129.5	129.6	60.0	58.7
180	23.8	47.8	44.3	137.1	137.0	136.9	136.5	134.1	132.3	134.3	135.4	135.9	60.0	58.7
200	23.8	47.9	44.2	135.9	135.8	135.7	135.1	132.5	130.8	133.4	134.2	134.5	60.0	58.6
220	23.9	48.2	44.2	131.8	131.6	131.6	130.7	127.9	127.1	130.7	130.9	131.2	60.0	58.6
240	24.0	48.5	44.2	124.4	124.2	124.5	123.9	122.5	121.8	122.8	122.8	122.8	60.0	58.6
260	24.0	48.7	44.1	113.3	112.6	112.9	112.2	111.0	110.7	111.8	111.6	112.2	60.0	58.6
280	24.1	48.6	44.2	100.9	99.5	99.8	99.3	99.0	99.5	100.0	98.6	99.9	60.0	58.6
300	24.1	47.9	44.4	85.0	83.5	83.7	83.6	83.4	84.3	85.9	83.7	85.0	59.9	58.6
320	24.1	47.5	44.7	69.7	68.6	68.7	68.9	69.0	70.6	72.7	69.5	70.2	59.9	58.6
340	24.1	47.7	44.8	55.5	54.7	55.0	55.3	55.9	57.9	59.1	56.2	55.9	59.9	58.6
360	24.2	47.7	44.9	49.3	48.3	48.8	49.6	50.5	51.4	51.0	49.9	49.1	59.9	58.6

Table B.10: Experimental results for test #*TH*2.

θ	T_{in}	T_{outA}	T_{outB}	T_1	T_2	T_3	T_4	T_5	T_6	T_7	T_8	T_9	P_{in}	P_{out}
[°]	[°C]												[psi]	
0	22.2	41.2	38.5	41.2	40.8	41.0	41.8	42.5	42.7	42.2	42.0	41.3	57.6	52.2
20	22.4	41.9	39.1	48.6	47.9	48.3	49.7	49.7	48.0	46.9	49.8	48.3	57.6	52.2
40	22.6	42.3	39.4	60.6	59.8	60.4	61.6	60.7	58.4	57.5	61.9	60.4	57.5	52.3
60	22.7	42.7	39.6	75.1	74.7	75.1	75.6	73.8	70.6	70.3	76.3	74.9	57.5	52.3
80	22.9	43.1	39.8	88.7	88.8	89.5	89.1	86.3	82.7	83.3	90.3	89.0	57.4	52.3
100	23.1	43.2	39.8	101.9	103.4	104.1	103.2	99.9	95.0	96.4	103.5	102.7	57.5	52.3
120	23.2	43.1	39.9	111.8	115.0	116.3	115.2	111.0	106.2	108.7	114.9	115.1	57.5	52.2
140	23.2	43.4	40.1	120.5	125.6	127.4	126.8	122.3	116.6	119.4	125.0	125.6	57.5	52.2
160	23.4	43.9	40.1	128.9	134.6	136.2	135.4	130.2	124.4	128.5	133.1	133.9	57.4	52.3
180	23.4	44.4	40.1	133.5	139.6	141.1	139.9	133.9	129.5	135.4	139.4	140.4	57.4	52.2
200	23.5	44.6	39.9	129.2	136.7	139.3	139.1	135.5	132.2	132.6	136.2	138.2	57.6	52.2
220	23.6	44.4	39.9	121.9	128.9	131.6	131.8	128.8	126.9	126.4	129.5	131.6	57.8	52.4
240	23.7	44.5	40.1	114.1	119.4	121.9	121.9	119.9	119.4	117.8	120.3	122.2	57.8	52.4
260	23.8	44.1	40.2	103.5	106.2	107.8	106.8	105.1	103.4	104.2	107.9	108.7	57.8	52.3
280	23.8	44.0	40.5	92.5	93.3	94.2	93.2	91.8	90.5	92.0	96.1	95.0	57.8	52.4
300	23.8	43.7	40.7	79.7	79.2	79.6	79.0	78.0	77.6	79.6	82.9	80.8	57.8	52.4
320	23.9	43.5	40.9	65.5	65.0	65.4	65.3	64.8	65.6	67.0	68.1	66.8	57.8	52.4
340	23.9	43.9	40.9	51.1	50.9	51.0	51.3	51.7	53.3	53.6	52.7	52.0	57.8	52.4
360	24.0	44.0	40.9	45.0	44.8	44.7	45.4	46.1	46.7	46.0	45.8	45.1	57.8	52.4

Table B.11: Experimental results for test #*TH*3.

θ	T_{in}	T_{outA}	T_{outB}	T_1	T_2	T_3	T_4	T_5	T_6	T_7	T_8	T_9	P_{in}	P_{out}
[°]	[°C]												[psi]	
0	21.5	40.8	36.5	41.6	41.3	42.7	41.9	42.6	43.5	43.0	42.2	41.2	52.3	41.2
20	21.8	42.0	37.9	48.3	47.7	49.8	49.4	49.5	48.0	46.6	49.0	47.6	53.2	42.1
40	22.0	42.5	38.5	63.0	61.8	64.5	64.6	63.6	60.5	59.0	64.5	62.3	53.1	42.2
60	22.3	43.4	39.1	79.3	78.7	80.9	81.0	79.2	74.8	73.3	81.4	78.4	53.1	42.3
80	22.6	43.9	39.4	93.3	94.5	96.8	95.7	93.4	88.0	87.0	95.6	93.4	53.0	42.3
100	22.8	44.1	39.8	105.4	108.6	111.9	110.3	107.2	100.9	100.4	108.3	107.2	52.9	42.2
120	22.9	44.8	39.7	117.5	125.1	129.8	128.9	124.8	116.9	118.4	126.2	125.2	53.1	42.3
140	23.0	44.4	40.2	120.1	132.0	137.8	137.3	133.0	126.0	129.2	135.1	133.6	53.1	42.3
160	23.1	45.2	40.0	128.9	143.8	150.6	151.2	147.6	139.8	140.2	145.1	144.1	53.0	42.3
180	23.2	45.1	40.1	130.5	146.7	153.9	154.6	151.2	145.4	145.2	148.6	147.5	53.0	42.3
200	23.3	45.3	40.2	128.5	143.9	151.1	151.9	148.7	146.5	145.8	148.0	147.8	53.0	42.2
220	23.3	45.2	40.2	122.0	135.5	142.3	143.2	140.4	138.1	138.4	141.2	142.1	53.1	42.0
240	23.4	45.2	40.3	115.9	125.3	129.9	130.3	127.3	125.3	127.1	130.0	131.5	53.2	42.1
260	23.5	44.6	40.6	106.0	111.6	113.0	112.7	110.1	108.8	110.8	114.2	115.8	53.1	42.0
280	23.6	44.7	40.8	97.6	101.0	100.7	99.8	97.2	96.3	98.5	103.0	102.1	52.9	41.9
300	23.6	44.8	41.0	85.3	86.7	86.9	85.2	83.4	83.6	85.1	88.9	87.1	52.7	41.7
320	23.7	44.9	41.1	68.7	69.4	71.0	69.0	68.4	69.5	70.3	71.9	70.2	52.4	41.4
340	23.8	45.3	41.1	53.2	53.6	55.9	53.6	54.0	56.4	56.4	55.7	54.6	52.3	41.3
360	23.8	45.5	41.3	46.2	46.4	47.9	47.1	47.7	48.1	47.3	46.7	46.3	52.1	41.2

Table B.12: Experimental results for test #*TH*4.

θ	T_{in}	T_{out}	T_1	T_2	T_3	T_4	T_5	T_6	T_7	T_8	T_9	P_{in}	P_{out}
[°]	[°C]											[psi]	
0	22.3	43.9	43.2	43.8	45.7	46.4	47.6	49.8	51.4	51.1	52.4	59.5	56.4
20	22.4	44.5	49.6	49.9	53.0	53.9	55.1	54.9	56.0	58.4	60.2	59.5	56.3
40	22.5	45.0	60.7	61.2	64.9	66.1	67.7	67.3	68.7	72.6	74.2	59.4	56.3
60	22.6	45.4	73.5	75.0	78.6	80.5	82.4	82.3	84.5	88.8	89.5	59.4	56.2
80	22.7	45.6	84.9	88.0	92.2	95.2	97.8	98.6	101.5	105.3	105.1	59.4	56.2
100	22.8	45.8	91.8	97.2	103.5	108.1	111.5	113.0	115.6	118.7	117.3	59.4	56.2
120	22.9	46.0	95.7	103.6	112.3	118.3	122.3	124.1	126.2	128.6	125.9	59.4	56.1
140	23.0	46.1	99.4	109.1	120.3	127.7	131.9	133.6	135.2	136.6	132.4	59.3	56.1
160	23.1	46.2	104.0	115.0	127.3	135.1	139.1	140.8	141.9	142.1	136.7	59.3	56.1
180	23.2	46.3	106.6	118.3	130.4	137.7	141.4	143.4	144.2	143.6	137.7	59.3	56.0
200	23.3	46.3	104.4	115.9	127.8	135.1	139.1	142.0	143.1	142.2	136.3	59.3	56.0
220	23.3	46.3	99.8	110.3	121.9	129.1	133.5	137.6	139.5	138.6	133.4	59.3	56.0
240	23.3	46.3	93.7	102.0	111.3	117.5	122.1	127.5	130.5	129.5	125.7	59.2	56.0
260	23.4	46.3	89.4	95.7	102.3	106.8	110.9	116.8	120.6	119.5	116.6	59.2	56.0
280	23.4	46.3	83.2	87.7	92.0	94.9	97.9	103.7	107.9	106.7	104.8	59.2	55.9
300	23.5	46.2	72.5	75.5	78.1	79.5	81.3	86.4	90.4	89.7	88.5	59.2	55.9
320	23.5	46.2	61.4	63.2	65.5	66.1	67.3	71.9	75.5	75.0	74.5	59.3	56.1
340	23.5	46.2	48.8	49.9	51.9	52.1	53.2	57.0	59.7	58.6	59.4	59.3	56.1
360	23.5	46.2	43.6	43.9	45.6	46.4	47.5	49.2	50.7	50.6	52.0	59.3	56.1

Table B.13: Experimental results for test #*TH*5.

θ	T_{in}	T_{out}	T_1	T_2	T_3	T_4	T_5	T_6	T_7	T_8	T_9	P_{in}	P_{out}
[°]	[°C]											[psi]	
0	23.1	41.4	38.1	38.0	39.6	40.1	41.2	42.4	43.8	44.0	45.3	58.3	45.3
20	23.0	41.7	44.4	44.0	46.8	47.3	48.5	48.2	49.2	52.3	53.7	58.4	45.4
40	23.0	42.0	55.7	55.3	58.8	59.6	60.8	61.0	63.0	68.2	68.9	58.5	45.4
60	23.0	41.9	65.5	66.5	69.9	71.3	73.6	74.8	78.3	84.1	84.6	58.4	45.3
80	23.2	41.8	70.9	73.3	77.0	80.4	84.7	88.3	93.1	98.6	99.4	58.4	45.3
100	23.2	41.9	74.2	77.2	81.8	87.2	94.6	100.9	107.0	112.0	113.2	58.5	45.2
120	23.2	41.8	77.8	80.6	85.1	91.7	101.8	111.7	118.9	124.2	125.1	58.4	45.2
140	23.2	41.8	81.0	83.5	87.7	94.1	105.2	117.3	125.8	131.7	132.3	58.4	45.2
160	23.1	41.8	85.8	88.1	91.8	97.8	109.2	123.5	133.7	139.6	138.9	58.4	45.2
180	23.1	41.8	88.1	90.1	93.3	98.9	110.5	125.7	136.3	141.2	139.9	58.4	45.2
200	23.2	41.8	86.5	88.8	92.1	97.7	108.9	124.0	134.6	138.8	137.3	58.4	45.2
220	23.2	41.8	85.0	87.5	91.0	96.8	108.2	122.9	133.2	137.1	135.9	58.4	45.2
240	23.2	42.1	79.4	83.2	87.9	95.1	106.6	119.1	127.2	128.7	128.4	58.4	45.2
260	23.2	42.0	75.4	79.3	84.0	89.9	99.0	110.1	117.7	118.2	117.6	58.4	45.2
280	23.3	42.0	72.4	76.3	80.4	84.0	89.6	98.9	106.0	105.4	104.2	58.4	45.2
300	23.3	42.0	67.2	70.2	73.2	75.1	78.0	85.2	91.6	91.2	89.6	58.4	45.2
320	23.2	42.0	55.7	57.4	60.0	60.6	61.7	67.2	72.2	71.8	70.9	58.4	45.2
340	23.3	42.0	44.5	45.3	47.5	47.6	48.6	52.4	55.5	54.6	55.0	58.3	45.3
360	23.3	42.0	39.9	40.0	41.8	42.3	43.5	45.3	47.0	46.8	47.8	58.3	45.3

Table B.14: Experimental results for test #*TH*6.

θ	T_{in}	T_{out}	T_1	T_2	T_3	T_4	T_5	T_6	T_7	T_8	T_9	P_{in}	P_{out}
[°]	[°C]											[psi]	
0	21.3	39.8	37.7	38.3	40.0	40.7	41.8	43.4	45.2	45.2	45.9	60.0	38.0
20	21.4	40.3	43.5	43.5	46.5	47.0	48.1	47.8	49.1	52.2	52.9	60.0	38.0
40	21.6	40.7	53.5	53.4	57.2	58.0	59.3	59.3	61.5	66.9	67.8	60.0	37.9
60	21.7	41.4	66.3	67.8	71.2	73.1	75.6	76.9	81.3	88.0	89.2	60.0	37.9
80	21.6	40.9	57.1	58.2	61.6	63.2	65.4	66.8	70.2	75.2	76.5	60.0	37.9
100	22.1	42.5	78.2	81.5	86.3	91.9	99.8	108.1	116.6	123.8	126.3	60.0	37.8
120	22.2	42.6	82.3	85.3	90.1	96.6	106.6	118.8	129.7	138.4	141.6	59.9	37.7
140	22.3	42.7	87.2	90.2	94.8	101.0	111.2	125.7	139.1	149.5	152.3	59.9	37.7
160	22.4	42.7	92.9	95.4	99.3	104.6	113.8	129.5	145.8	157.0	158.2	59.9	37.7
180	22.4	42.8	95.2	97.5	101.0	105.9	114.9	131.3	148.3	158.7	159.5	59.9	37.7
200	22.6	42.9	94.0	96.7	100.3	105.4	115.0	131.6	147.9	156.9	157.5	59.8	37.6
220	22.6	43.0	88.9	92.0	96.1	102.0	112.8	128.8	143.3	150.4	151.4	59.8	37.6
240	22.7	43.1	83.5	86.7	91.2	97.5	108.3	123.2	135.3	140.1	140.9	59.8	37.7
260	22.7	43.1	79.4	82.8	87.5	93.2	102.5	115.6	125.9	128.1	128.0	59.8	37.6
280	22.7	43.0	75.4	78.9	83.0	86.6	92.2	102.5	111.5	111.9	111.2	59.8	37.6
300	22.8	42.7	67.1	69.7	72.4	74.2	76.6	84.3	91.3	91.6	92.2	59.7	37.6
320	22.9	42.6	56.8	58.2	60.7	61.4	62.5	68.1	73.6	73.5	72.6	59.7	37.6
340	22.9	42.7	45.1	45.9	48.0	48.0	48.9	52.9	56.4	55.5	56.0	59.7	37.6
360	22.9	42.9	40.0	39.9	41.7	42.3	43.4	44.8	46.5	46.8	48.3	59.7	37.7

Table B.15: Experimental results for test #*TH*7.

θ	T_{in}	T_{out}	T_1	T_2	T_3	T_4	T_5	T_6	T_7	T_8	T_9	P_{in}	P_{out}
[°]	[°C]											[psi]	
0	22.4	43.3	53.4	47.8	48.3	46.2	45.4	44.7	44.2	43.4	43.3	59.8	57.1
20	22.6	43.9	66.4	57.7	57.8	56.5	54.8	51.0	49.7	51.2	50.7	59.8	57.1
40	22.7	44.8	90.9	78.1	77.1	75.8	72.9	67.6	66.0	68.5	67.9	59.8	57.2
60	22.8	45.6	113.4	98.7	97.0	95.3	91.6	85.4	83.3	85.9	85.2	59.7	57.2
80	22.9	46.0	136.2	119.8	117.6	114.8	110.8	104.2	101.3	103.4	102.6	59.7	57.2
100	23.0	46.1	155.7	137.9	134.1	130.6	126.7	120.0	116.3	117.5	116.0	59.7	57.2
120	23.1	46.2	169.4	153.0	148.2	144.4	140.4	134.0	129.9	129.9	126.9	59.7	57.2
140	23.1	46.1	184.1	168.4	161.7	157.5	153.2	147.1	143.0	142.3	138.3	59.6	57.2
160	23.2	46.2	193.5	179.6	171.1	166.2	161.6	155.9	151.8	150.5	146.4	59.6	57.1
180	23.2	46.2	196.4	184.4	175.0	169.5	164.6	159.7	156.1	154.2	150.0	59.6	57.1
200	23.3	46.2	191.9	179.8	170.9	165.3	160.4	156.8	153.7	150.9	146.7	59.6	56.9
220	23.3	46.2	183.0	169.5	161.7	156.5	151.9	149.1	146.5	143.1	139.0	59.6	56.8
240	23.4	46.3	168.9	155.3	149.5	144.9	140.8	138.7	136.5	133.2	129.9	59.7	56.9
260	23.4	46.3	149.7	137.9	133.9	129.6	126.0	124.6	123.3	120.4	118.1	59.8	57.0
280	23.5	46.2	129.2	119.7	117.3	113.4	110.0	109.4	109.2	106.9	105.5	59.8	56.9
300	23.5	46.3	109.4	102.3	100.6	96.8	93.7	93.8	94.6	92.4	91.4	59.8	56.9
320	23.5	46.3	85.9	81.2	80.4	76.7	74.3	74.8	76.0	73.3	72.6	59.7	56.9
340	23.6	46.3	65.5	61.8	62.2	58.7	57.2	58.1	58.7	56.0	55.7	59.7	57.0
360	23.6	46.3	56.4	52.2	52.8	50.5	49.6	48.6	48.2	47.4	47.2	59.7	57.0

Table B.16: Experimental results for test #*TH*8.

θ	T_{in}	T_{out}	T_1	T_2	T_3	T_4	T_5	T_6	T_7	T_8	T_9	P_{in}	P_{out}
[°]	[°C]											[psi]	
0	21.9	39.6	46.5	42.9	43.6	41.9	41.3	40.6	39.8	38.8	38.4	57.8	46.2
20	22.0	39.9	57.4	50.8	51.8	50.9	49.2	45.7	44.1	45.1	43.8	57.8	46.1
40	22.2	40.4	78.9	68.3	68.8	68.3	65.3	60.0	57.9	58.9	56.6	57.7	46.2
60	22.3	40.7	99.7	86.2	86.8	84.9	81.2	74.9	72.0	72.5	69.2	57.7	46.2
80	22.4	41.3	128.4	109.3	110.0	106.0	101.9	94.5	89.7	87.9	83.3	57.6	46.3
100	22.5	41.4	154.4	130.8	129.1	123.8	119.8	111.1	103.6	97.5	90.7	57.6	46.3
120	22.6	41.5	177.9	151.1	145.9	141.2	136.2	126.7	116.3	104.8	95.4	57.6	46.4
140	22.7	41.6	194.0	168.5	160.4	155.6	149.6	139.4	126.6	111.1	99.9	57.6	46.3
160	22.7	41.5	209.0	185.4	174.6	168.7	162.2	151.7	137.8	120.3	106.8	57.6	46.3
180	22.7	41.5	215.0	192.9	180.1	173.0	166.2	157.1	144.0	126.0	111.3	57.6	46.2
200	22.7	41.5	209.1	184.8	172.9	166.2	159.8	152.4	140.1	121.0	107.7	57.6	46.0
220	22.8	41.6	199.5	169.3	159.8	153.8	147.9	141.8	130.4	112.6	101.2	57.8	45.9
240	22.9	41.8	185.6	151.3	145.1	139.8	134.8	130.0	120.7	106.0	96.1	57.9	46.1
260	22.9	41.8	161.9	132.2	129.1	124.0	120.0	116.5	110.1	99.3	91.2	57.9	46.1
280	23.0	41.5	128.5	107.4	106.9	102.0	99.3	97.5	94.2	87.3	81.8	57.9	45.9
300	23.0	41.6	102.7	90.9	90.9	86.6	84.3	83.7	82.6	77.1	73.0	57.9	46.0
320	23.0	41.7	79.4	72.9	73.5	69.5	67.7	68.1	68.1	63.3	60.7	57.9	45.9
340	23.0	41.7	57.3	54.2	55.3	51.7	50.6	51.7	51.7	48.4	47.4	57.8	46.1
360	23.0	41.7	48.0	45.4	46.2	44.3	43.6	43.0	42.3	41.1	40.6	57.8	46.1

Table B.17: Experimental results for test #*TH*9.

θ	T_{in}	T_{out}	T_1	T_2	T_3	T_4	T_5	T_6	T_7	T_8	T_9	P_{in}	P_{out}
[°]	[°C]											[psi]	
0	22.8	42.1	49.6	46.5	46.9	45.2	44.4	43.6	42.7	41.5	40.9	60.0	39.2
20	22.8	42.4	62.1	55.3	56.4	55.4	53.5	49.5	47.6	48.6	47.3	60.0	39.3
40	22.7	42.6	87.4	75.3	76.0	75.5	71.9	66.3	63.6	65.0	62.3	60.0	39.3
60	22.7	42.7	114.7	98.1	98.4	96.3	91.8	84.8	81.2	82.2	78.8	60.0	39.4
80	22.7	42.8	146.0	119.7	120.6	116.5	111.3	103.1	97.4	95.2	90.8	59.9	39.5
100	22.8	42.9	174.7	142.3	140.9	134.5	129.2	119.0	109.9	103.0	96.7	59.9	39.5
120	22.8	42.8	199.4	167.3	161.3	154.6	147.7	134.6	120.6	108.7	101.0	59.9	39.5
140	22.8	42.9	226.9	191.3	180.0	173.4	165.0	149.4	130.3	114.9	106.6	59.9	39.6
160	22.8	42.8	245.3	209.5	194.8	187.4	178.4	161.6	139.5	121.9	112.8	59.9	39.5
180	22.8	42.8	255.2	218.5	201.7	193.3	184.1	168.8	146.9	127.9	118.2	60.0	39.4
200	22.8	42.9	259.8	211.9	194.2	186.2	177.1	163.7	143.2	124.2	115.4	60.0	39.3
220	22.9	43.0	237.3	190.1	178.2	171.5	163.6	152.3	134.2	116.9	108.6	60.2	39.1
240	23.0	43.0	212.6	168.9	161.9	156.2	149.2	140.5	126.3	111.4	103.2	60.3	39.0
260	23.0	43.1	177.1	143.7	142.1	136.7	131.6	126.2	116.7	105.5	97.9	60.1	39.1
280	23.0	43.0	147.3	121.8	123.4	117.4	114.4	111.6	106.3	98.4	92.2	60.2	39.1
300	23.0	41.7	104.6	92.5	92.4	88.1	85.8	85.1	84.1	78.5	74.4	57.9	45.9
320	23.0	41.7	80.0	73.4	74.0	70.0	68.1	68.6	68.5	63.8	61.3	57.9	45.9
340	23.0	41.7	57.4	54.3	55.4	51.8	50.7	51.8	51.8	48.4	47.4	57.8	46.1
360	23.0	41.7	48.0	45.4	46.2	44.3	43.6	43.0	42.3	41.1	40.6	57.8	46.1

Table B.18: Numerical results for test #*TS*1.

θ	T_1	T_2	T_3	T_4	T_5	HF_1	HF_2	HF_3	HF_4	HF_5
[°]	[°C]					[kW/m^2]				
0	62.7	69.3	79.2	85.1	89.7	37.9	42.2	47.6	48.9	47.9
20	68.7	76.5	87.5	93.7	98.1	23.7	23.7	24.9	22.4	21.3
40	79.3	88.8	101.5	107.3	111.3	20.3	20.3	21.7	19.6	19.2
60	91.4	102.5	116.7	122.1	125.7	18.6	18.2	13.0	17.7	17.5
80	103.8	116.1	130.3	136.6	139.9	17.4	17.2	14.6	16.6	16.7
100	115.7	129.0	142.2	150.2	153.5	16.9	16.8	16.2	16.0	16.3
120	126.8	140.7	153.1	162.5	166.0	16.1	15.1	15.8	15.2	15.7
140	136.8	150.2	162.3	172.9	176.9	14.1	14.9	14.8	14.0	14.3
160	144.2	157.2	169.2	180.5	185.3	12.2	13.0	12.9	11.9	11.6
180	147.5	160.2	172.2	183.6	188.8	7.7	9.1	9.4	9.0	7.8

Table B.19: Numerical results for test #*TS*2.

θ	T_1	T_2	T_3	T_4	T_5	HF_1	HF_2	HF_3	HF_4	HF_5
[°]	[°C]					[kW/m^2]				
0	55.1	60.8	67.6	70.3	73.2	72.2	71.4	71.7	68.6	66.4
20	62.2	67.8	75.3	77.9	80.8	43.9	47.0	52.3	50.1	49.4
40	72.6	79.8	90.5	92.9	95.7	45.2	45.8	51.0	44.8	43.8
60	85.5	94.9	109.3	110.6	112.8	43.8	43.3	33.2	41.9	41.6
80	100.1	111.2	126.2	128.6	130.0	41.9	41.4	35.7	40.6	41.2
100	114.6	127.2	140.8	145.9	146.7	41.4	41.8	40.0	39.6	41.2
120	129.2	142.9	154.9	162.2	163.0	41.4	37.5	39.2	38.6	40.8
140	143.0	155.7	167.3	176.4	178.0	37.6	38.0	37.9	37.0	39.2
160	153.8	165.6	177.0	187.3	190.4	35.2	35.5	35.3	33.8	35.3
180	159.0	170.2	181.4	192.1	196.3	25.9	28.0	29.2	28.2	25.0

Table B.20: Numerical results for test #*TS*3.

θ	T_1	T_2	T_3	T_4	T_5	HF_1	HF_2	HF_3	HF_4	HF_5
[°]	[°C]					[kW/m^2]				
0	60.9	68.8	76.4	80.5	83.3	128.3	132.3	137.2	133.6	131.6
20	66.6	75.7	84.4	89.1	92.2	78.9	78.1	82.5	74.7	75.0
40	79.3	89.9	100.9	104.1	105.8	72.8	75.9	84.7	79.3	78.7
60	93.5	105.5	118.7	119.2	121.1	78.6	80.0	68.8	78.8	77.9
80	111.0	123.9	136.3	137.7	141.6	77.9	78.1	68.3	76.6	76.7
100	131.8	145.2	155.1	160.8	165.2	76.1	78.3	76.0	74.9	76.7
120	153.8	167.2	177.5	187.0	190.6	75.7	70.4	73.4	73.0	76.5
140	174.3	188.1	199.9	212.4	215.3	69.8	71.2	71.2	70.5	75.0
160	192.6	205.8	218.2	232.8	236.3	67.0	67.9	67.6	65.8	69.9
180	201.1	213.6	226.0	241.6	246.8	55.6	57.7	58.7	56.2	54.3

Table B.21: Numerical results for test #*TS*4.

θ	T_1	T_2	T_3	T_4	T_5	T_6	T_7	T_8	T_9
[°]	[°C]								
0	29.6	32.2	36.2	40.0	46.9	56.9	70.0	79.4	88.6
20	31.2	34.0	38.7	43.1	51.0	61.9	75.5	85.6	94.6
40	34.6	38.6	44.4	49.8	58.8	70.7	84.5	95.2	103.6
60	38.9	43.7	50.4	56.7	66.6	79.2	92.8	103.9	111.7
80	44.1	49.6	56.7	64.1	74.7	87.8	100.9	112.1	119.2
100	49.2	55.6	63.1	71.4	82.5	95.6	108.1	119.1	125.6
120	54.8	61.8	69.7	78.6	89.8	102.3	114.2	124.8	130.6
140	61.6	68.9	77.0	86.0	96.7	108.4	119.6	129.7	134.8
160	67.9	75.0	82.9	91.5	101.5	112.2	122.9	132.4	137.1
180	71.3	78.1	85.6	94.0	103.6	114.0	124.4	133.8	138.2
θ	HF_1	HF_2	HF_3	HF_4	HF_5	HF_6	HF_7	HF_8	HF_9
[°]	[kW/m^2]								
0	13.6	16.7	20.8	23.6	28.0	32.5	36.0	37.4	35.6
20	9.6	10.2	11.4	10.7	10.5	10.4	9.8	9.2	8.0
40	8.9	8.9	9.0	8.6	8.0	7.5	6.7	6.4	5.7
60	8.0	7.8	6.7	7.6	7.2	6.8	6.3	5.7	5.1
80	7.8	7.9	7.5	7.6	7.1	6.3	6.0	5.5	4.9
100	8.4	8.1	7.9	7.4	6.8	5.9	5.7	5.3	4.7
120	8.3	7.8	7.4	6.8	6.0	5.5	5.3	5.0	4.5
140	7.0	6.4	5.8	5.2	4.7	4.6	4.7	4.6	4.2
160	3.2	2.8	2.7	2.8	3.2	3.8	4.2	4.3	4.0
180	1.9	0.7	0.4	1.3	2.4	3.3	3.9	4.1	3.9

Table B.22: Numerical results for test #*TS*5.

θ	T_1	T_2	T_3	T_4	T_5	T_6	T_7	T_8	T_9
[°]	[°C]								
0	27.8	30.6	34.0	36.5	40.2	44.8	50.5	53.5	57.8
20	31.0	33.7	37.1	39.4	43.0	47.7	54.5	57.9	62.9
40	35.4	38.5	42.2	44.8	49.3	55.3	63.5	68.2	73.8
60	38.4	42.2	46.9	50.3	56.0	63.2	71.8	78.0	84.1
80	41.8	47.3	52.6	57.3	64.1	72.3	81.0	88.3	94.5
100	45.5	52.6	58.5	64.3	71.8	80.7	89.3	97.2	103.5
120	49.9	57.8	64.6	71.2	79.1	88.0	96.5	104.6	110.7
140	56.8	65.2	72.7	79.6	87.4	95.8	104.1	112.0	117.9
160	63.7	71.9	79.4	86.1	93.4	101.1	108.8	116.3	121.9
180	69.0	76.8	83.9	90.3	97.2	104.6	112.0	119.4	124.9
θ	HF_1	HF_2	HF_3	HF_4	HF_5	HF_6	HF_7	HF_8	HF_9
[°]	[kW/m^2]								
0	24.0	16.7	20.1	22.6	26.3	29.7	34.0	36.4	39.3
20	18.9	19.1	20.1	19.3	20.3	21.8	22.6	22.1	21.4
40	17.3	17.9	18.7	19.1	19.9	18.9	16.9	17.9	17.4
60	20.1	20.5	19.6	19.6	18.0	17.4	16.1	16.6	16.2
80	17.8	16.5	15.7	16.7	16.3	16.6	16.5	15.7	15.3
100	17.0	16.3	16.0	16.7	16.8	16.3	16.3	15.5	14.9
120	17.2	17.1	17.8	17.6	17.1	16.2	15.9	15.2	14.6
140	18.5	17.8	17.4	16.5	15.6	15.3	14.9	14.6	14.1
160	14.9	13.8	13.1	12.9	12.9	13.1	13.3	13.4	13.1
180	1.1	3.3	4.9	6.0	7.3	8.5	9.4	10.3	10.6

Table B.23: Numerical results for test #*TS*6.

θ	T_1	T_2	T_3	T_4	T_5	T_6	T_7	T_8	T_9
[°]	[°C]								
0	123.9	111.1	103.5	96.2	84.1	73.4	67.5	58.2	53.3
20	136.6	121.5	113.0	105.5	92.7	81.0	73.7	63.6	58.0
40	158.8	139.2	128.9	120.5	107.2	94.3	84.6	74.3	66.4
60	180.8	157.3	144.6	134.6	121.5	107.3	95.6	84.8	75.3
80	201.7	176.2	161.0	149.4	136.1	121.2	108.0	96.2	85.3
100	219.0	193.6	176.3	163.0	149.1	134.3	120.3	107.6	95.8
120	232.2	208.4	189.6	174.7	160.3	145.6	131.6	118.5	106.3
140	242.1	221.0	201.1	184.9	170.0	155.6	142.0	129.3	117.3
160	247.5	228.6	208.1	191.0	175.9	161.8	148.6	136.6	125.2
180	249.9	232.0	211.4	194.0	178.7	164.7	151.7	139.9	128.9

continued on next page

continued from previous page									
θ	HF_1	HF_2	HF_3	HF_4	HF_5	HF_6	HF_7	HF_8	HF_9
[°]	[kW/m^2]								
0	65.3	56.2	54.0	51.8	48.7	44.1	35.8	34.4	28.6
20	20.6	18.3	17.5	16.6	16.8	16.7	13.8	17.0	16.7
40	14.0	14.5	13.9	12.3	13.5	13.6	13.4	13.5	13.8
60	9.9	13.0	12.6	12.2	12.0	12.9	13.5	13.1	13.2
80	7.3	11.7	11.6	11.4	11.0	12.0	13.0	12.9	13.7
100	5.9	10.3	10.6	10.6	10.6	10.9	12.0	12.7	13.3
120	5.5	9.0	9.4	9.6	9.8	9.9	10.6	11.5	12.3
140	5.5	7.5	8.1	8.5	8.8	8.8	9.0	9.4	10.0
160	5.5	6.1	6.8	7.4	7.6	7.5	7.3	6.9	6.7
180	5.3	4.8	5.3	6.2	6.5	6.3	5.8	5.0	3.9

Table B.24: Numerical results for test *#TS7*.

θ	T_1	T_2	T_3	T_4	T_5	T_6	T_7	T_8	T_9
[°]	[°C]								
0	37.1	40.4	45.5	46.6	49.5	52.0	52.4	53.8	61.0
20	39.1	42.3	47.7	49.2	52.4	55.3	55.5	57.8	68.0
40	43.7	48.4	53.4	56.2	59.9	63.1	62.9	67.4	86.6
60	48.7	53.9	58.8	62.6	66.8	69.6	69.3	77.6	111.7
80	55.3	60.9	65.8	70.5	75.1	76.7	77.0	91.2	137.9
100	61.8	67.8	72.9	78.3	82.5	83.7	84.7	105.3	151.5
120	68.0	74.4	80.1	85.4	89.0	90.4	92.0	116.7	154.3
140	76.6	83.3	88.8	93.6	97.1	98.9	100.9	125.0	152.6
160	83.5	89.8	94.7	99.1	102.6	104.9	106.8	127.2	147.1
180	88.5	94.4	99.1	103.4	106.9	109.5	111.4	129.1	146.4
θ	HF_1	HF_2	HF_3	HF_4	HF_5	HF_6	HF_7	HF_8	HF_9
[°]	[kW/m^2]								
0	36.2	38.6	36.5	39.7	40.0	40.3	41.0	44.7	57.1
20	23.8	24.4	23.0	24.6	26.0	26.7	27.1	29.7	38.5
40	22.8	23.3	24.0	23.8	23.8	22.3	24.4	27.8	35.3
60	23.5	23.0	23.5	23.3	22.8	23.1	24.4	27.7	18.0
80	23.9	23.4	23.7	23.3	22.5	23.7	24.8	25.3	4.0
100	24.2	24.1	23.9	23.0	23.4	24.0	24.6	20.9	8.4
120	24.8	24.0	23.3	23.3	23.5	23.8	23.6	17.4	13.7
140	23.5	22.7	22.6	22.6	22.4	22.2	22.0	16.1	18.7
160	20.0	19.7	19.7	19.5	19.1	18.6	19.5	19.2	23.8
180	8.0	9.8	10.7	11.3	11.7	11.7	13.2	22.3	26.9

Table B.25: Numerical results for test #*TH*1.

θ	T_1	T_2	T_3	T_4	T_5	HF_{avg}
[°]	[°C]					[kW/m^2]
0	47.8	49.3	51.7	54.9	57.9	53.4
20	54.3	56.6	59.9	64.4	68.7	32.3
40	63.5	67.0	71.6	79.1	86.1	22.1
60	83.8	86.0	89.2	93.1	101.3	25.5
80	90.7	93.0	96.4	102.3	111.1	27.4
100	97.2	99.6	103.1	109.9	120.9	28.2
120	103.9	106.3	110.1	117.3	132.7	27.9
140	110.9	113.3	117.2	124.8	145.5	26.7
160	117.5	119.9	123.9	131.7	156.2	23.4
180	120.9	123.5	127.4	135.3	160.3	1.57

Table B.26: Numerical results for test #*TH*2.

θ	T_1	T_2	T_3	T_4	T_5	HF_{avg}
[°]	[°C]					[kW/m^2]
0	44.7	45.9	46.7	47.3	47.1	79.6
20	55.9	58.2	59.1	59.5	60.3	48.7
40	71.9	76.9	77.4	76.7	76.0	34.1
60	85.9	91.4	90.9	89.5	86.9	37.2
80	100.9	101.4	101.1	97.5	96.1	37.8
100	107.5	111.1	110.7	108.6	105.8	36.0
120	117.2	120.4	122.1	119.8	116.8	33.6
140	126.2	129.9	132.1	130.4	129.7	31.1
160	133.7	136.9	138.2	138.8	141.5	29.9
180	136.7	139.6	141.0	143.1	146.7	25.6

Table B.27: Numerical results for test #*TH*3.

θ	T_1	T_2	T_3	T_4	T_5	HF_{avg}
[°]	[°C]					[kW/m^2]
0	37.9	38.9	39.9	41.3	42.0	74.5
20	48.2	49.5	50.6	52.8	55.0	47.7
40	63.2	66.8	68.7	71.9	73.9	32.6
60	76.0	80.2	82.0	83.7	87.4	35.6
80	88.9	91.4	93.1	93.8	100.9	38.0
100	93.4	99.6	102.3	103.1	115.1	37.8
120	101.8	108.6	111.7	111.5	129.0	36.9
140	110.0	116.8	119.3	119.6	141.4	35.0
160	116.3	122.7	124.8	126.7	149.7	33.1
180	119.5	125.7	128.0	130.7	151.9	23.6

APPENDIX C

SINGLE-SIDED T-TUBE EXPERIMENTAL AND NUMERICAL DATA

This appendix tabulates the range of experimental and numerical parameters for all the tests performed on the T-tube apparatus with single-sided heating. Table C.1 lists and describes the symbols used in the following tables.

Table C.1: List and description of the experimental symbols.

Type	Units	Symbol	Description
Temperature	°C	T_{in}	Air inlet temperature
		T_{outA}	Air temperature at outlet port "A" (Figure 4.6)
		T_{outB}	Air temperature at outlet port "B" (Figure 4.6)
		T_{MAX}	Maximum copper temperature
		T_{nAx}	Copper neck temperatures at instrumented plane "A" (Figure 4.8)
		T_{nBx}	Copper neck temperatures at instrumented plane "B" (Figure 4.8)
		T_{PlX}	Temperatures at instrumented plane #X
Heat Flux	kW/m^2	HF_{PlX}	Numerical heat flux at instrumented plane #X
Pressure	psi	P_{in}	Inlet gauge pressure
		P_{outA}	Gauge pressure at outlet port "A" (Figure 4.6)
		P_{outB}	Gauge pressure at outlet port "B" (Figure 4.6)

Each table refers to the corresponding experiment number listed in Table 4.1. Locations "A" and "B" are symmetric with respect to the inlet port at the center of the test module; the difference between experimental values recorded at locations "A" vs. "B" is due to imperfections in the experimental apparatus (e.g., thermal contact between the copper block and the brass). The same applies to axial planes #1 and #3.

Table C.2: Experimental results for test #$TT1$.

Temperature Profiles												
$\|\theta\|$ [°]	T_{Pl1} [°C]			T_{Pl2} [°C]			T_{Pl3} [°C]					
0	176.5			162.7			177.6					
30	177.3			163.0			177.5					
60	174.5			161.9			176.1					
90	168.7			159.8			169					
120	162.8			157.2			164.9					
Experimental Conditions												
T_{MAX}	T_{in}	T_{outA}	T_{outB}	T_{nA1}	T_{nA2}	T_{nA3}	T_{nB1}	T_{nB2}	T_{nB3}	P_{in}	P_{outA}	P_{outB}
217.2	23.3	89.3	81.8	203.4	204.6	206.0	203.3	204.4	206.0	59.93	58.94	58.91
[°C]										[psi]		

Table C.3: Experimental results for test #$TT2$.

Temperature Profiles												
$\|\theta\|$ [°]	T_{Pl1} [°C]			T_{Pl2} [°C]			T_{Pl3} [°C]					
0	224.5			199.7			226.1					
30	226.0			200.3			226.0					
60	221.4			196.1			222.4					
90	207.7			191.7			206.5					
120	195.7			185.2			197.5					
Experimental Conditions												
T_{MAX}	T_{in}	T_{outA}	T_{outB}	T_{nA1}	T_{nA2}	T_{nA3}	T_{nB1}	T_{nB2}	T_{nB3}	P_{in}	P_{outA}	P_{outB}
311.5	22.6	87.3	75.7	275.0	278.2	282.3	274.7	277.8	282.2	58.94	55.85	55.81
[°C]										[psi]		

Table C.4: Experimental results for test #$TT3$.

Temperature Profiles												
$\|\theta\|$ [°]	T_{Pl1} [°C]			T_{Pl2} [°C]			T_{Pl3} [°C]					
0	278.8			265.6			280.3					
30	280.6			266.6			280.6					
60	274.5			258.7			274.7					
90	255.2			246.4			251.7					
120	237.2			232.7			238.0					
Experimental Conditions												
T_{MAX}	T_{in}	T_{outA}	T_{outB}	T_{nA1}	T_{nA2}	T_{nA3}	T_{nB1}	T_{nB2}	T_{nB3}	P_{in}	P_{outA}	P_{outB}
408.1	22.3	101.0	99.8	339.7	345.9	353.6	339.8	346.2	354.4	59.79	53.08	53.01
[°C]										[psi]		

Table C.5: Experimental results for test #$TT4$.

Temperature Profiles												
$\|\theta\|$ [°]	T_{Pl1} [°C]			T_{Pl2} [°C]			T_{Pl3} [°C]					
0	319.0			283.4			334.4					
30	321.3			282.8			327.7					
60	314.7			277.9			317.2					
90	289.5			266.0			288.8					
120	269.7			256.0			272.1					
Experimental Conditions												
T_{MAX}	T_{in}	T_{outA}	T_{outB}	T_{nA1}	T_{nA2}	T_{nA3}	T_{nB1}	T_{nB2}	T_{nB3}	P_{in}	P_{outA}	P_{outB}
475.0	22.3	101.4	86.4	398.3	405.1	413.8	397.0	403.9	413.3	59.65	52.05	51.89
[°C]										[psi]		

Table C.6: Experimental results for test #$TT5$.

Temperature Profiles												
$\|\theta\|$ [°]	T_{Pl1} [°C]			T_{Pl2} [°C]			T_{Pl3} [°C]					
0	305.2			246.6			342.0					
30	307.8			243.5			326.5					
60	304.4			254.5			308.1					
90	267.2			227.8			272.7					
120	248.0			228.1			249.0					
Experimental Conditions												
T_{MAX}	T_{in}	T_{outA}	T_{outB}	T_{nA1}	T_{nA2}	T_{nA3}	T_{nB1}	T_{nB2}	T_{nB3}	P_{in}	P_{outA}	P_{outB}
517.6	22.1	85.6	71.2	420.8	429.0	439.7	418.0	426.0	438.1	59.84	39.53	39.05
[°C]										[psi]		

Table C.7: Experimental results for test #$TT6$.

Temperature Profiles												
$\|\theta\|$ [°]	T_{Pl1} [°C]			T_{Pl2} [°C]			T_{Pl3} [°C]					
0	293.1			273.2			321.8					
30	296.4			275.8			309.3					
60	289.9			264.9			292.7					
90	261.8			248.3			261.7					
120	239.0			231.6			240.0					
Experimental Conditions												
T_{MAX}	T_{in}	T_{outA}	T_{outB}	T_{nA1}	T_{nA2}	T_{nA3}	T_{nB1}	T_{nB2}	T_{nB3}	P_{in}	P_{outA}	P_{outB}
489.8	21.8	91.9	87.4	389.1	397.9	409.3	386.3	395.8	408.3	58.42	38.99	37.36
[°C]										[psi]		

Table C.8: Num. results for test #*TT*1.

θ	T_{Pl1}	T_{Pl2}	HF_{Pl1}	HF_{Pl2}
[°]	[°C]		[kW/m^2]	
0	169.9	168.7	140.5	183.3
30	168.6	167.3	58.1	75.0
60	165.0	163.0	33.3	29.5
90	159.5	156.2	27.2	1.4
120	154.7	149.6	28.0	2.9

Table C.9: Num. results for test #*TT*2.

θ	T_{Pl1}	T_{Pl2}	HF_{Pl1}	HF_{Pl2}
[°]	[°C]		[kW/m^2]	
0	218.9	215.8	389.3	553.1
30	216.8	213.7	175.6	223.0
60	209.1	205.6	94.5	74.3
90	196.4	191.4	64.3	11.4
120	185.2	177.5	60.2	8.8

Table C.10: Numerical results for test #*TT*3.

θ	T_{Pl1}	T_{Pl2}	HF_{Pl1}	HF_{Pl2}
[°]	[°C]		[kW/m^2]	
0	290.2	284.5	809.0	1137.1
30	287.6	281.8	337.7	426.6
60	275.6	269.4	186.4	148.8
90	255.8	247.6	133.0	38.4
120	238.4	226.1	88.1	7.5

Table C.11: Numerical results for test #*TT*4.

θ	T_{Pl1}	T_{Pl2}	HF_{Pl1}	HF_{Pl2}
[°]	[°C]		[kW/m^2]	
0	320.1	313.8	935.1	1319.3
30	316.6	310.3	386.6	489.1
60	302.1	295.7	213.4	169.5
90	278.3	270.2	153.3	44.9
120	257.6	245.6	102.0	1.6

Table C.12: Numerical results for tests #*TT*5 and #*TT*6.

θ	T_{Pl1}	T_{Pl2}	HF_{Pl1}	HF_{Pl2}
[°]	[°C]		[kW/m^2]	
0	305.0	297.7	1278.0	1717.1
30	301.0	293.7	563.7	674.1
60	283.3	276.1	313.4	263.6
90	254.3	246.2	208.2	72.9
120	229.4	217.7	191.6	14.9

APPENDIX D

MULTI-JET EXPERIMENTAL AND NUMERICAL DATA

This appendix tabulates the range of experimental and numerical parameters for all the tests performed on the HEMJ apparatus. Table D.1 lists and describes the symbols used in the following tables. Each data table refers to the corresponding experiment number listed in Tables 5.3 and 5.4. For the experiments spanning an azimuthal range larger than 60° (e.g., *MJ*#23), only numerical results for angles between $0° < \theta < 60°$ will be reported, because of the six-fold symmetry of the jet cartridge.

Table D.1: List and description of the experimental symbols.

Type	**Units**	**Symbol**	**Description**
Temperature	°C	T_{in}	Air inlet temperature
		T_{out}	Air temperature at outlet port
		T_{MAX}	Maximum copper temperature
		T_{nx}	Copper neck temperatures
		T_x	Thimble temperature at location #x
		T_{xS}	Surface temperature at location #x
Heat Flux	kW/m^2	HF_x	Numerical heat flux at location #x
Pressure	psi	P_{in}	Inlet gauge pressure
		P_{out}	Outlet gauge pressure

Table D.2: Experimental data for the constant azimuthal angle ($\theta = 0°$) tests.

Test	T_1	T_2	T_3	T_4	T_{n1}	T_{n2}	T_{n3}	T_{MAX}	T_{in}	T_{out}	P_{in}	P_{out}
$\#MJ$	[°C]										[psi]	
1	149.1	156.5	159.6	160.7	183.8	190.3	196.0	220.9	18.4	60.5	104.5	103.3
2	122.2	129.8	132.9	134.0	158.7	165.4	171.3	197.0	18.2	47.9	104.0	101.0
3	104.3	111.7	114.8	115.9	141.1	147.7	153.6	178.9	18.1	40.5	103.0	98.3
4	85.1	92.4	95.5	96.6	123.4	130.3	136.4	162.4	18.0	32.8	101.0	87.9
5	77.7	85.1	88.2	89.2	117.9	125.1	131.5	158.7	17.9	29.7	99.0	73.4
6	228.4	239.9	244.8	246.2	282.3	292.5	301.9	342.4	20.0	84.5	107.0	105.4
7	185.9	197.5	202.5	204.0	242.1	252.6	262.1	303.0	20.5	66.2	106.0	103.4
8	163.5	175.0	180.1	181.6	220.9	231.5	241.1	282.2	21.0	57.7	106.0	100.8
9	132.2	143.6	148.6	150.1	191.3	202.0	211.6	252.9	20.1	45.3	103.5	92.8
10	112.3	123.5	128.4	129.8	172.6	183.4	193.1	234.6	21.2	39.2	101.5	75.9
11	231.6	242.9	247.8	249.3	284.8	295.0	304.3	344.4	20.6	86.1	107.0	105.6
12	187.1	198.7	203.7	205.2	243.6	254.2	263.7	305.0	21.0	67.5	106.0	102.8
13	160.6	172.3	177.3	178.9	218.6	229.4	239.0	280.6	20.3	56.1	106.0	100.0
14	131.9	143.3	148.1	149.6	190.4	201.1	210.7	251.7	21.0	46.0	104.0	92.8
15	113.7	124.9	129.8	131.1	173.5	184.4	194.0	235.5	20.4	39.1	104.0	81.9
16	277.4	291.0	296.6	298.5	342.0	354.9	366.8	417.5	21.1	101.3	107.0	105.3
17	219.2	233.1	238.9	241.0	286.5	299.8	311.9	363.3	20.1	76.9	106.0	102.5
18	190.5	204.1	209.9	211.9	257.9	271.1	283.0	333.5	20.6	65.4	105.0	99.9
19	153.7	167.1	172.8	174.7	223.4	236.7	248.8	299.9	20.7	50.5	104.0	91.8
20	134.8	148.2	153.9	155.7	206.6	220.3	232.6	284.6	20.4	43.2	102.0	77.9

Table D.3: Experimental data for test #*MJ*21.

θ	T_1	T_2	T_3	T_4	T_{n1}	T_{n2}	T_{n3}	T_{MAX}	T_{in}	T_{out}	P_{in}	P_{out}
[°]	[°C]										[psi]	
0	122.2	129.8	132.9	134.0	158.7	165.4	171.3	196.8	18.2	47.9	104.0	100.9
15	122.5	130.0	133.2	134.3	159.0	165.6	171.6	197.0	18.3	48.0	104.0	101.0
30	122.4	130.1	133.2	134.4	159.1	165.8	171.7	197.2	18.4	48.2	104.0	101.0
45	122.4	130.1	133.3	134.5	159.2	165.9	171.9	197.5	18.4	48.3	104.0	101.0
60	122.6	130.3	133.4	134.6	159.3	166.0	172.0	197.6	18.3	48.8	104.0	101.1

Table D.4: Experimental data for test #*MJ*22.

θ	T_1	T_2	T_3	T_4	T_{n1}	T_{n2}	T_{n3}	T_{MAX}	T_{in}	T_{out}	P_{in}	P_{out}
[°]	[°C]										[psi]	
0	187.6	198.7	203.6	205.2	242.7	253.1	262.5	303.0	20.7	67.1	108.5	105.9
15	188.7	199.6	204.3	206.0	243.6	254.0	263.4	304.0	21.0	68.0	108.5	106.4
30	187.7	198.8	203.5	205.3	243.2	253.7	263.2	304.1	21.3	69.0	108.5	106.0
45	190.1	200.9	205.7	207.3	244.8	255.2	264.6	305.1	21.2	70.0	108.5	105.5
60	187.9	199.0	203.9	205.6	243.7	254.3	263.8	305.0	21.0	70.5	108.5	106.0

Table D.5: Experimental data for test #*MJ*23.

θ	T_1	T_2	T_3	T_4	T_{n1}	T_{n2}	T_{n3}	T_{MAX}	T_{in}	T_{out}	P_{in}	P_{out}
[°]	[°C]										[psi]	
0	277.4	291.0	296.6	298.5	342.0	354.9	366.8	417.5	21.1	101.3	107.0	105.3
15	275.0	288.9	294.8	296.8	341.0	354.1	366.2	417.6	21.1	102.9	107.0	105.2
30	272.5	287.5	293.4	295.3	339.3	352.4	365.4	416.0	20.9	102.9	107.0	105.4
45	275.1	289.1	294.8	296.7	340.1	353.1	365.0	415.7	20.8	103.7	107.0	105.1
60	274.5	288.2	294.1	296.0	339.6	352.6	364.5	415.5	20.6	101.3	107.0	105.1
180	274.4	288.2	294.0	295.9	339.4	352.4	364.4	415.3	21.1	101.3	107.0	105.1
195	274.5	288.0	293.8	295.8	339.3	352.3	364.2	415.1	20.8	100.5	107.0	105.3
210	274.0	287.8	293.5	295.5	339.0	352.0	364.0	415.0	20.6	100.2	107.0	105.4
225	274.2	287.8	293.6	295.6	339.0	352.0	364.0	414.9	20.6	100.2	107.0	105.4
240	275.3	288.4	294.1	296.1	339.4	352.4	364.3	414.9	20.4	99.9	107.0	105.4

Table D.6: Experimental data for test #*MJ*24.

θ	T_1	T_2	T_3	T_4	T_{n1}	T_{n2}	T_{n3}	T_{MAX}	T_{in}	T_{out}	P_{in}	P_{out}
[°]	[°C]										[psi]	
0	223.0	236.9	242.7	244.8	289.9	303.3	315.3	366.6	20.3	79.0	106.0	103.4
15	223.2	236.9	242.7	244.8	289.9	303.2	315.1	366.3	20.4	79.0	106.0	100.1
30	222.7	236.7	242.4	244.6	289.6	302.9	314.8	366.0	20.3	79.1	106.0	100.3
45	222.4	236.4	242.3	244.4	289.4	302.7	314.7	365.8	20.3	79.0	106.0	103.6
60	222.8	236.4	242.3	244.4	289.4	302.7	314.6	365.7	20.4	80.1	106.0	103.7
75	222.1	235.7	241.7	243.8	288.8	302.1	314.1	365.2	20.2	78.7	106.0	103.9
90	221.8	235.8	241.6	243.6	288.7	301.9	313.9	365.0	20.4	78.4	106.0	103.9
105	222.0	235.8	241.6	243.7	288.6	301.9	313.8	364.9	20.5	78.3	106.0	103.6
120	222.8	236.2	241.9	244.0	288.8	302.0	313.9	364.9	20.4	78.4	106.0	103.2

Table D.7: Experimental data for test #*MJ*25.

θ	T_1	T_2	T_3	T_4	T_{n1}	T_{n2}	T_{n3}	T_{MAX}	T_{in}	T_{out}	P_{in}	P_{out}
[°]	[°C]										[psi]	
0	190.5	204.1	209.9	211.9	257.9	271.1	283.0	333.5	20.6	65.4	105.0	99.9
15	190.7	204.3	210.2	212.2	258.4	271.5	283.4	334.0	20.6	65.4	105.0	100.1
30	191.0	204.9	210.5	212.5	258.7	271.8	283.8	334.4	20.6	65.4	105.0	100.3
45	190.9	204.8	210.6	212.5	258.8	272.0	283.9	334.7	20.6	65.3	105.0	100.3
60	191.3	204.7	210.7	212.6	259.0	272.2	284.1	335.0	20.5	66.0	105.0	100.4
75	191.8	205.0	211.0	213.0	259.3	272.5	284.5	335.3	20.3	65.1	105.0	100.5
90	191.4	205.1	210.9	212.9	259.3	272.5	284.5	335.4	20.3	64.9	105.0	100.6
105	192.2	205.7	211.5	213.5	259.8	273.0	284.9	335.7	20.3	64.8	105.0	100.1
120	192.8	205.8	211.6	213.6	259.9	273.1	285.0	335.8	20.3	64.8	105.0	100.1

Table D.8: Numerical results for the constant azimuthal angle ($\theta = 0°$) tests.

Test	T_1	T_2	T_3	T_4	T_{1S}	T_{2S}	T_{3S}	T_{4S}	HF_1	HF_2	HF_3	HF_4
#MJ	[°C]								[kW/m^2]			
1	150.37	157.54	159.89	160.12	150.16	156.12	158.45	156.47	310	220	175	430
2	124.34	131.39	133.61	133.72	123.88	129.72	131.94	129.93	370	260	210	520
3	108.15	114.78	116.80	116.78	107.58	113.06	114.98	112.90	400	280	230	570
4	89.35	95.71	97.52	97.32	88.52	93.73	95.38	93.08	480	320	280	690
5	81.61	87.98	89.67	89.23	80.62	85.78	87.25	84.44	530	370	330	820
6, 11	231.27	242.92	246.68	247.13	230.65	240.42	244.15	243.41	510	360	280	740
7, 12	189.22	200.38	203.79	204.04	188.25	197.64	200.96	199.76	610	415	320	840
8, 13	167.91	178.59	181.73	181.82	166.70	175.66	178.65	177.13	670	450	360	940
9, 14	137.71	148.10	150.97	150.83	136.04	144.71	147.37	145.25	800	560	430	1120
10, 15	115.22	124.89	127.37	126.96	113.24	121.26	123.45	120.74	880	595	490	1270
16	275.30	290.96	295.83	297.17	275.45	288.54	293.56	292.98	650	450	360	900
17	225.22	238.55	242.64	242.83	224.10	235.32	239.29	237.93	780	530	420	1060
18	193.81	207.21	210.99	211.98	193.24	204.35	208.21	206.79	850	590	470	1180
19	155.96	168.08	171.44	171.30	153.94	164.08	167.15	164.71	1000	690	550	1380
20	136.85	148.74	151.87	151.48	134.44	144.37	147.13	144.03	1180	790	630	1580

Table D.9: Numerical results for test #*MJ*21.

θ	T_1	T_2	T_3	T_4	T_{1S}	T_{2S}	T_{3S}	T_{4S}	HF_1	HF_2	HF_3	HF_4
[°]	[°C]								[kW/m^2]			
0	124.34	131.39	133.61	133.72	123.88	129.72	131.94	129.93	340	250	160	470
15	124.65	131.37	133.58	133.72	124.71	129.72	131.64	129.93	110	235	275	470
30	124.70	131.29	133.56	133.72	124.59	129.32	131.37	129.93	175	365	390	470
45	124.62	131.39	133.58	133.72	124.67	129.82	131.65	129.93	110	235	275	470
60	124.32	131.37	133.61	133.72	123.88	129.70	131.95	129.93	340	250	160	470

Table D.10: Numerical results for test #*MJ*22.

θ	T_1	T_2	T_3	T_4	T_{1S}	T_{2S}	T_{3S}	T_{4S}	HF_1	HF_2	HF_3	HF_4
[°]	[°C]								[kW/m^2]			
0	192.27	203.47	206.91	207.17	191.32	200.74	204.08	202.92	630	390	370	820
15	192.83	203.49	206.86	207.17	192.82	200.82	203.65	202.92	210	350	450	820
30	192.89	203.41	206.81	207.17	192.55	200.13	203.22	202.92	320	530	620	820
45	192.81	203.55	206.84	207.17	192.80	200.96	203.53	202.92	210	350	450	820
60	192.26	203.56	206.88	207.17	191.41	200.80	204.02	202.92	630	390	370	820

Table D.11: Numerical results for test #*MJ*23.

θ	T_1	T_2	T_3	T_4	T_{1S}	T_{2S}	T_{3S}	T_{4S}	HF_1	HF_2	HF_3	HF_4
[°]	[°C]								[kW/m^2]			
0	277.10	291.21	295.77	296.33	276.37	288.21	292.73	291.86	610	440	350	820
15	277.67	291.26	295.73	296.33	277.86	288.30	292.30	291.86	200	410	460	820
30	277.74	291.18	295.68	296.33	277.62	287.66	291.86	291.86	320	520	610	820
45	277.65	291.34	295.71	296.33	277.84	288.43	292.18	291.86	200	410	460	820
60	277.10	291.32	295.75	296.33	276.47	288.29	292.67	291.86	610	440	350	820

Table D.12: Numerical results for test #*MJ*24.

θ	T_1	T_2	T_3	T_4	T_{1S}	T_{2S}	T_{3S}	T_{4S}	HF_1	HF_2	HF_3	HF_4
[°]	[°C]								[kW/m^2]			
0	225.22	238.55	242.64	242.83	224.10	235.32	239.29	237.93	810	520	470	1020
15	225.88	238.57	242.58	242.83	225.89	235.41	238.77	237.93	255	440	600	1020
30	225.96	238.48	242.52	242.83	225.57	234.59	238.26	237.93	410	680	790	1020
45	225.86	238.65	242.56	242.83	225.86	235.58	238.63	237.93	255	440	600	1020
60	225.21	238.66	242.61	242.83	224.20	235.39	239.21	237.93	810	520	470	1020

Table D.13: Numerical results for test #*MJ*25.

θ	T_1	T_2	T_3	T_4	T_{1S}	T_{2S}	T_{3S}	T_{4S}	HF_1	HF_2	HF_3	HF_4
[°]	[°C]								[kW/m^2]			
0	193.81	207.21	210.99	211.98	193.24	204.35	208.21	206.79	810	520	470	1100
15	194.84	207.01	210.97	211.98	195.02	204.59	207.91	206.79	255	440	600	1100
30	195.05	207.00	211.00	211.98	194.76	203.89	207.57	206.79	410	680	790	1100
45	194.90	207.16	211.21	211.98	195.09	204.41	207.81	206.79	255	440	600	1100
60	194.13	207.37	211.12	211.98	193.30	204.30	208.25	206.79	810	520	470	1100

REFERENCES

Baxi, C. B. and Wong, C. "Review of helium cooling for fusion reactor applications". *Fusion Engineering and Design*, **51-52**:319–324, 2000.

Behbahani, A. I. and Goldstein, R. J. "Local heat transfer to staggered arrays of impinging circular air jets". *J. Eng. Power*, **105**:354–360, 1983.

Boccaccini L.V., et al. "He-cooled divertor concepts". In *US-Japan Workshop on Fusion Power Plants and Related Advanced Technologies*, Tokyo, Japan, 11-13 Jan. 2005.

"CFD Online", April 2008. URL `http://www.cfd-online.com/`. (Last checked: May 2008).

Crosatti, L., Sadowski, D. L., Weathers, J. B., Abdel-Khalik, S. I., Yoda, M., and the ARIES Team. "Experimental and numerical investigation of the thermal performance of gas-cooled t-tube divertor modules". *Fusion Science and Technology*, 2007.

Dano, B. P. E., Liburdy, J. A. and Kanokjaruvijit, K. "Flow characteristics and heat transfer performances of a semi-confined impinging array of jets". *International Journal Of Heat And Mass Transfer*, **48**:691–701, 2005.

EC Energy Research. "European Community Energy Research website", May 2008. URL `http://ec.europa.eu/research/energy/index_en.htm`. (Last checked: May 2008).

EFDA-JET. "Official JET website, The world's largest nuclear fusion research facility", March 2008. URL `http://www.jet.efda.org/`. (Last checked: May 2008).

El-Gabry, L. A. and Kaminski, D. A "Numerical investigation of jet impingement with cross flow — Comparison of Yang-Shih and standard kϵ turbulence models,". *Numer. Heat Transfer: Part A: Appl.*, **47**:441–469, 2005.

Eren, H., Yesilata, B. and Celik, N. "Nonlinear flow and heat transfer dynamics of impinging jets onto slightly-curved surfaces". *Applied Thermal Engineering*, **27**:2600–2608, 2007.

Fitzgerald, J. A. and Garimella, S. V "A study of the flow field of a confined and submerged impinging jet". *Int. J. Heat Mass Transfer*, **41**:8–91025–1034, 1998.

FLUENT®. "FLUENT 6.2 Documentation", 2004. URL `http://www.fluent.com/`. (Last checked: July 30, 2007).

Gardon, R. and Akfirat, J. C. "Heat transfer characteristics of impinging two-dimensional air jets". *J. Heat Transfer*, **88**:101–108, 1966.

Garimella, S. V and Rice, R. A. "Confined and submerged liquid jet impingement heat transfer". *J. Heat Transfer*, **117**:871–877, 1995.

Guerra, D. R. S., Su, J., Atila, P. and Silva Freire, A.P. "The near wall behavior of an impinging jet". *International Journal Of Heat And Mass Transfer*, **48**:4019–4027, 2005.

Harlow, F. H. and Nakayama, P. I. "Transport of turbulence energy decay rate". *Los Alamos Sci. Lab.*, **LA-3854** 1968.

Hermsmeyer, S. and Kleefeldt, K. "Review and comparative assessment of helium-cooled divertor concepts". In *FZKA 6597*, 2001.

Hermsmeyer, S. and Malang, S. "Gas-cooled high performance divertor for a power plant". *Fusion Eng. Des.*, **197**:61–62, 2002.

Huber, A. M. and Viskanta, R. "Effect of jetjet spacing on convective heat transfer to confined, impinging arrays of axisymmetric air jets". *International Journal Of Heat And Mass Transfer*, **37**:2859–2869, 1994.

Ihli, T., et al. "An advanced he-cooled divertor concept". *Fusion Eng. Des.*, 2006.

Ihli, T. "He-cooled divertor development in the eu: The helium jet cooled divertor hemj". In *ARIES Meeting, General Atomics, San Diego, CA*, 24-25 Feb. 2005.

Ihli, T., Raffray, A. R., and The ARIES Team "Aries cs report: Helium cooled divertor design study". In *UCSD-CER-06-04*, 2005. URL `http://aries.ucsd.edu/CER/reports.shtml`.).

Incropera, F. and DeWitt, D. *Fundamentals of Heat and Mass Transfer*. John Wiley & Sons, Hoboken, NJ, 5th edition, 2002.

ITER. "Official ITER website", April 2008. URL `http://www.iter.org/`. (Last checked: May 2008).

Karditsas, P. and Taylor, N. "Thermal fluid finite element calculations for the european ppcs divertor concepts". Washington D.C., 17-21 Nov. 2002. 15th TOFE.

Kercher, D. M. and Tabakoff, W. "Heat transfer by a square array of round air jets impinging perpendicular to a flat surface including the effect of spent air". *J. Eng. Power*, **92**:73–82, 1970.

Key, M.H. "Fast track to fusion energy". *Nature*, **412**:775-776, 2001.

Kleefeldt, K. and Gordeev, S. "Performance limits of a helium-cooled divertor (unconventional design)". In *FZKA 6401*, 2000.

Kruessmann, R., et al. "Conceptual design of a he-cooled divertor with integrated flow and heat transfer promoters". *PPCS Subtask TW3-TRP-001-D2, Part II Detailed Version*, **FZKA 6975**, 2004.

Lin, Z. H., Chou, Y. J. and Hung, Y. H. "Heat transfer behaviors of a confined slot jet impingement". *International Journal Of Heat And Mass Transfer*, **40**:1095–1107, 1997.

Maisonnier, D., et al. "A conceptual study of commercial fusion power plants". *EFDA*, **EFDA-RP-RE-5.0**, April 2005.

Malang, S. and Hermsmeyer, S. "Fzk-concept of helium-cooled divertor plates for power plants". In *PPCS Design Review Meeting He-cooled Divertor*, Garching, Nov. 2001.

Martin, H. "Heat and Mass Transfer between Impinging Gas Jets and Solid Surfaces". In *Advances in Heat Transfer*, **13**, Academic Press, New York, 1977.

Mau, T. K., et al. "Divertor configuration and heat load assessment for aries-cs". In *ARIES Project Meeting, Princeton, NJ*, Oct. 4-5 2006. URL `http://aries.ucsd.edu/ARIES/MEETINGS/0610/Mau_divertor.pdf`.).

Metzger, D. E., Florschuetz, L. W., Takeuchi, D. I., Behee, R. D. and Berry, R. A. "Heat transfer characteristics for inlined and staggered arrays of circular jets with crossflow of spent air,". *J. Heat Transfer*, **101**:526–531, 1979.

Najmabadi, F. "Recent progress in the aries compact stellarator study". *Fusion Engineering and Design*, **81, Issues 23-24**:2679–2693, 2006.

Norajitra, P., et al. "Divertor conceptual designs for a fusion power plant". Number S3-0006-339, Heidelberg, Germany, Sept. 30 - Oct. 5 2007. ISFNT-8.

Norajitra, P., et al. "State of the art: Development of a helium-cooled divertor for demo". In *Proceedings of SOFE meeting, San Diego*, Oct. 14-17 2003a.

Norajitra, P., et al. "Conceptual design of the dual-coolant blanket within the framework of the eu power plant conceptual study". In *(TW2-TRP-PPCS12), Final Report, Forschungszentrum Karlsruhe, Wissenschaftliche Berichte, FZKA 6780*, 2003b.

Norajitra, P., et al. "European development of he-cooled divertors for fusion power plants". *Nuclear Fusion*, **45**: 1271-1276, 2005a.

Norajitra, P., et al. "Status of he-cooled divertor development". *FZKA 7100*, **TW4-TRP-001-D2**, 2005b.

Nuclear Fusion Power. "Assessing fusion power", May 2007. URL `http://www.world-nuclear.org/info/inf66.html`. (Last checked: Jun 2008).

Ongena, J. and Van Oost, G.. "Energy for Future Centuries", 1999. URL `http://www.fusie-energie.nl/artikelen/ongena.pdf`. (Last checked: June 2008).

Pope, Stephen B. *Turbulent Flows*. Cambridge University Press, UK, 1st edition, 2000.

Raffray, A. R., et al. "Design and performance of the aries-cs divertor". *Fusion Eng. Des.*, 2006.

Salamah, S. A. and Kaminski, D. A. "Modeling of turbulent heat transfer from an array of submerged jets impinging on a solid surface". *Numer. Heat Transfer: Part A: Appl.*, **48**: 315–337, 2005.

San, J. Y., Huang, C. H., and Shu, M. H. "Impingement cooling of a confined circular air jet". *International Journal Of Heat And Mass Transfer*, **40**: 1355–1364, 1997.

San, J. Y. and Shiao, W. Z. "Optimum jet-to-jet spacing of heat transfer for staggered arrays of impinging air jets". *International Journal Of Heat And Mass Transfer*, **44** : 3997–4007, 2001.

San, J. Y. and Shiao, W. Z. "Effects of jet plate size and plate spacing on the stagnation Nusselt number for a confined circular air jet impinging on a flat plate". *International Journal Of Heat And Mass Transfer*, **49** (19-20):3477–3486, 2006.

San, J. Y., Tsou, Y. M., and Chen, Z. C. "Impingement heat transfer of staggered arrays of air jets confined in a channel". *International Journal Of Heat And Mass Transfer*, **50** (19-20):3718–3727, September 2007.

Saripalli, K. R. "Visualization of multijet impingement flow". *AIAA J.*, **21**:483–484, 1983.

Shin, S., et al. "Thermal analysis of helium-cooled t-tube divertor". ARIES Project presentation, Madison, WI, June 14-15 2005. URL `http://aries.ucsd.edu/ARIES/MEETINGS/0506/Abdel-Khalik.pdf`.).

Stacey, W. M., J. *Fusion: An introduction to the physics and technology of mag- netic confinement fusion*. John Wiley & Sons, 1984.

"ThinkQuest, Education Foundation". URL `http://www.thinkquest.org/library/`. (Last checked: May 2008).

Weathers, J. B. "Thermal performance of helium-cooled divertors for magnetic fusion application". Master's thesis, School of Mechanical Engineering, Georgia Institute of Technology, 2007.

Wikipedia "Wikipedia, the free enciclopedia", December 2007. URL `http://en.wikipedia.org/wiki/Fusion_power`. (Last checked: June 2008).

Yakhot, V. and Orszag, S.A. "Renormalization group analisys of turbulence". I. Basic theory. *J. Sci. Comput*, **Vol. 1**(3–51).

Zhou, D. and Lee, S.-J. "Forced convective heat transfer with impinging rectangular jets". *International Journal of Heat and Mass Transfer*, **50**(9-10):1916–1926, May 2007.

VITA

Lorenzo Crosatti was born in Caprino Veronese, Italy, on January 22, 1980, the son of Crosatti Giovanni and Sometti Annalisa. After completing his work at *I.T.I.S. Galileo Ferraris* — a renowned high-school in Verona, Italy — in 1999, he entered the *Universitá degli Studi di Brescia*, Italy. Before the end of the program, in 2004, he joined the Graduate School at the *Georgia Institute of Technology*: he spent two semesters at Georgia Tech Lorraine in Metz, France and one semester in the Atlanta Campus. After completion of the Italian degree in Mechanical Engineering in Brescia in March 2005 (summa cum laude), he was also conferred the Master of Science in Mechanical Engineering at Georgia Tech in Atlanta. In August 2005, he continued his studies at Georgia Tech, where he started the Ph.D. program in the same field.

This thesis was typed by Lorenzo Crosatti.